

**NUMERICAL INVESTIGATION OF MULTIPLE-IMPINGING SLOT  
JETS IN THE GAS-JET WIPING OF LIQUID ZINC COATINGS**

# Numerical Investigation of Multiple-Impinging Slot Jets in the Gas-Jet Wiping of Liquid Zinc Coatings

By

PARSA TAMADONFAR, B.A.Sc.

A Thesis

Submitted to the School of Graduate Studies

In Partial Fulfillment of the Requirements

For the Degree

Master of Applied Science

McMaster University

© Copyright by Parsa Tamadonfar, September 2010

Master of Applied Science (2010)  
(Mechanical Engineering)

McMaster University  
Hamilton, Ontario

TITLE: Numerical Investigation of Multiple-Impinging Slot Jets in  
the Gas-Jet Wiping of Liquid Zinc Coatings

AUTHOR: Parsa Tamadonfar, B.A.Sc. (Sharif University of Technology)

SUPERVISORS: Dr. Joseph R. McDermid, Dr. Andrew N. Hrymak

NUMBER OF PAGES: xx, 107

## Abstract

A turbulent impinging slot jet is a device which is used in various industrial applications such as glass tempering, heating of complex surfaces, cooling of turbine blades, cooling of electronic devices and in the continuous hot-dip galvanizing line, which is the focus of this study. An impinging slot jet is used to control the zinc film thickness on the sheet substrate to reach uniform product coating thickness by applying a pressure gradient and shear stress distribution on the moving substrate, after immersion in a bath of molten zinc. The impinging jet wipes the excess molten zinc from the steel strip through the combined effects of a pressure gradient and shear stress distribution on the steel strip.

In this study, the fluid flow of three multiple-impinging slot jet configurations discharging air at high velocity on a moving substrate were investigated numerically. Computational fluid dynamics was used to determine the wall pressure results and wall shear stress distributions due to the multiple impinging slot jets, and these results were used as boundary conditions in an analytical model to estimate the final liquid zinc thickness on the substrate. The standard  $k - \varepsilon$  turbulence model with non-equilibrium wall treatments was used to capture the turbulence parameters in the flow field.

The knowledge of using multiple-impinging slot jets in the hot-dip galvanizing line process as a wiping actuator is quite limited. There is not any systematic work available in using these devices as a wiping actuator. In this study, three models of multiple slot jets were developed numerically with the goal of estimating the coating

weight on the moving sheet substrate. The conventional model of a single-impinging slot jet was used as a base case for comparing the wall pressure results, wall shear stress distributions and consequently the coating weight data on a moving substrate with different multiple-impinging slot jet configurations. Adjusting the various process parameters such as main slot jet Reynolds number ( $Re_m$ ), auxiliary slot jet Reynolds number ( $Re_a$ ), plate-to-nozzle ratio ( $z/d$ ) and sheet substrate velocity ( $V_{substrate}$ ) allows the producers to control the coating weight on a moving sheet substrate.

For this study, the numerical simulations were solved using FLUENT commercial code. A comprehensive set of numerical modeling over a wide range of process variables was performed for all configurations in order to present a broad summary of the coating weight trends in the wiping process. A full analysis of the wall pressure distributions and wall shear stress results, as well as coating weight estimation generated under different impinging slot jets have been presented in this study.

## **Acknowledgments**

It would be my honor to express my gratitude to Dr. Joseph R. McDermid and Dr. Andrew N. Hrymak for their precious guidance and patience through my studies at McMaster University. Also, I gratefully appreciate my lovely parents Mehrdad and Fariba and my sister Mahsa for their love and support.

Additionally, my thesis could not have been completed without funding support from Dr. Frank E. Goodwin, Executive Vice President of Technology and Market Development at the International Lead-Zinc Research Organization.

I deeply thank the generosity of my friends at McMaster University, particularly Hadi Noori, Andrew Sliasis, Suzie Brown, Wajih Hamouda, David Arthurs and Kevin McLaren for their helpful discussions during my thesis preparation.

Last but not least, I would like to thank Elnaz for her love and encouragement, which helped me a lot to progress my work.

*Try not to become a man of success, but rather try to become a man of value.*

Albert Einstein

## Table on Contents

<i>Abstract</i> .....	iii
<i>Acknowledgments</i> .....	v
<i>Table on Contents</i> .....	vii
<i>List of Figures</i> .....	ix
<i>List of Tables</i> .....	xiv
<i>Nomenclature</i> .....	xv
<b>Chapter 1: Introduction</b> .....	1
1.1 Thesis Statement.....	1
1.2 Motivation and Objectives.....	1
1.3 Thesis Layout.....	3
<b>Chapter 2: Literature Review</b> .....	5
2.1 Continuous Hot-Dip Galvanizing Line Process.....	5
2.2 Air Knife Coating .....	6
2.3 Coating Thickness Model Estimation.....	14
<b>Chapter 3: Simulation Models</b> .....	18
3.1 Navier-Stokes Equations.....	18
3.2 Turbulence Modeling.....	19
3.2.1 Reynolds-Averaged Navier-Stokes (RANS) Equations .....	22
3.2.2 The Turbulent-Viscosity Model .....	23
3.2.3 Standard $k - \epsilon$ Turbulence Model .....	24
3.2.4 Wall Functions.....	25
3.3 Discretization Method.....	26
3.4 Mesh.....	26
<b>Chapter 4: Numerical Analysis</b> .....	29
4.1 Single-Impinging Slot Jet .....	29
4.1.1 Geometry, Boundary and Initial Conditions.....	30
4.1.2 Plate-to-Nozzle Ratio Effect.....	32
4.1.3 Main Slot Jet Reynolds Numbers Effect .....	38
4.2 Two Parallel Impinging Slot Jets.....	42
4.2.1 Geometry, Boundary and Initial Conditions.....	43

4.2.2	Plate-to-Nozzle Ratio Effect.....	44
4.2.3	Main Slot Jet Reynolds Numbers Effect .....	51
4.2.4	Wall Thickness-to-Nozzle Ratio Effect.....	53
4.3	Main Jet with Inclined Auxiliary Impinging Slot Jet.....	54
4.3.1	Geometry, Boundary and Initial Conditions.....	55
4.3.2	Plate-to-Nozzle Ratio Effect.....	56
4.3.3	Main Slot Jet Reynolds Number Effect.....	62
4.3.4	Auxiliary Slot Jet Reynolds Number Effect .....	65
4.3.5	Wall Thickness-to-Nozzle Ratio Effect.....	68
4.4	Main Jet with Two Adjacent Inclined Auxiliary Impinging Slot Jets .....	70
4.4.1	Geometry, Boundary and Initial Conditions.....	70
4.4.2	Plate-to-Nozzle Ratios Effect .....	71
4.4.3	Main Slot Jet Reynolds Number Effect.....	78
4.4.4	Auxiliary Slot Jets Reynolds Number Effect .....	80
4.4.5	The Ratio Between the Distance of the Main Slot Jet and Auxiliary Slot Jet to Nozzle Gap Effect .....	83
4.5	Comparison Between the Coating Weights for All Configurations .....	84
	<b>Chapter 5: Conclusions and Proposals for Future Work .....</b>	<b>87</b>
5.1	Conclusions.....	87
5.2	Proposals for Future Work.....	88
	<b>References .....</b>	<b>90</b>
	<b>Appendix A: Coating Thickness Sensitivity to Different Turbulence Models .....</b>	<b>95</b>
i.	Numerical Simulations .....	95
ii.	Wall Pressure Correlations .....	96
iii.	Wall Shear Stress Correlations.....	98
iv.	Coating Thickness Results.....	100
v.	Additional Results .....	102

## List of Figures

Figure 1-1: Schematic of a single-impinging slot jet case [Elsaadawy <i>et al.</i> , 2007].....	2
Figure 2-1: Schematic of a pot region in continuous hot-dip galvanizing line [Marder, 2000].....	5
Figure 2-2: Time evolution of the film thickness throughout the wiping process [Lacanette <i>et al.</i> , 2005].....	9
Figure 2-3: Visualization of the liquid film: (a) the impingement region; (b) upstream of the impingement region; (c) downstream of the impingement region [Lacanette <i>et al.</i> , 2005].....	10
Figure 2-4: (a) Splashing in hot-dip galvanizing line; and (b) splashing on the substrate with water [Gosset and Buchlin, 2007].....	11
Figure 2-5: (a) Two opposing impinging slot jets without baffle; and (b) Two opposing impinging slot jets with baffle [Arthurs, 2007].....	11
Figure 2-6: Deflection of the flow due to the Coanda effect [Ahn and Chung, 2006].....	12
Figure 3-1: (a) The quadrilaterals mesh close to the centerline of the main jet for a single-impinging slot jet; and (b) The quadrilaterals mesh close to the centerline of the main jet and triangles near the auxiliary slot jets for multiple-impinging slot jets.....	27
Figure 4-1: Schematic for a single-impinging slot jet.....	30
Figure 4-2: Non-dimensional mean velocity profile at the nozzle exit.....	31
Figure 4-3: Non-dimensional wall pressure distributions for different $z/d$ ratios with $Re_m = 11000$ .....	33
Figure 4-4: Non-dimensional wall shear stress distributions for different $z/d$ ratios with $Re_m = 11000$ .....	34
Figure 4-5: Non-dimensional maximum (a) wall pressure; and (b) wall shear stress for different $z/d$ ratios with $Re_m = 11000$ for a single-impinging slot jet.....	35
Figure 4-6: Pressure contour and streamlines for $z/d = 4$ and $Re_m = 11000$ .....	36
Figure 4-7: Coating weight for different $z/d$ ratios, with $V_{strip} = 0.50$ m/s and $Re_m = 11000$ .....	37

Figure 4-8: Coating weight for different $V_{Strip}$ and $z/d$ ratios with $Re_m = 11000$ .....	37
Figure 4-9: Non-dimensional wall pressure distributions for different $Re_m$ with $z/d = 4$ .....	39
Figure 4-10: Non-dimensional wall shear stress distributions for different $Re_m$ with $z/d = 4$ .....	40
Figure 4-11: Coating weight variation with $Re_m$ , with $V_{Strip} = 0.50 \text{ m/s}$ and $z/d = 4$ ..	41
Figure 4-12: Coating weight for varying $Re_m$ and $V_{Strip}$ with $z/d = 4$ ....	42
Figure 4-13: Schematic for two parallel impinging slot jets.....	43
Figure 4-14: Non-dimensional wall pressure distributions for different $z/d$ ratios with $Re_m = 11000$ and $a/d = 12$ .....	45
Figure 4-15: Non-dimensional wall shear stress distributions for different $z/d$ ratios with $Re_m = 11000$ and $a/d = 12$ .....	46
Figure 4-16: Comparison of non-dimensional maximum (a) wall pressure; and (b) shear stresses for different $z/d$ ratios for both configuration of a single-impinging slot jet and two parallel impinging slot jets.....	47
Figure 4-17: Pressure contour and streamlines with $z/d = 4$ , $Re_m = 11000$ and $a/d = 12$ .....	48
Figure 4-18: Comparison of coating weight for a single-impinging slot jet and two parallel impinging slot jets for different $z/d$ ratios, with $V_{Strip} = 0.50 \text{ m/s}$ and $Re_m = 11000$ ....	50
Figure 4-19: Coating weight for different $V_{Strip}$ and $z/d$ ratios with $Re_m = 11000$ ....	50
Figure 4-20: Comparison of non-dimensional maximum wall pressure for different $Re_m$ for $z/d = 4$ ....	51
Figure 4-21: Comparison of non-dimensional maximum wall shear stress for different $Re_m$ for $z/d = 4$ for a single-impinging slot jet and two parallel impinging slot jets.....	52
Figure 4-22: Coating weight for different $Re_m$ and $V_{Strip}$ with $z/d = 4$ .....	53
Figure 4-23: Coating weight for different $a/d$ and $V_{Strip}$ with $z/d = 4$ and $Re_m = 11000$ ....	54
Figure 4-24: Schematic for a main with an inclined auxiliary impinging slot jets.....	55

Figure 4-25: Non-dimensional wall pressure distributions for different $z/d$ ratios with $Re_m = Re_a = 11000$ .....	57
Figure 4-26: Non-dimensional wall shear stress distributions for different $z/d$ ratios with $Re_m = Re_a = 11000$ .....	59
Figure 4-27: Comparison of non-dimensional maximum (a) wall pressure; and (b) wall shear stress for different $z/d$ ratios for both configurations of a single-impinging slot jet and a main jet with inclined auxiliary impinging slot jet.....	60
Figure 4-28: Pressure contour and streamlines for $z/d = 4$ and $Re_m = Re_a = 11000$ ....	60
Figure 4-29: Comparison of coating weight for a single-impinging slot jet and a main with inclined auxiliary impinging slot jet for different $z/d$ ratios, with $V_{strip} = 0.50$ m/s, $Re_m = 11000$ and $Re_a = 11000$ ....	61
Figure 4-30: Coating weight for different $V_{strip}$ and $z/d$ ratios with $Re_m = Re_a = 11000$ ...62	
Figure 4-31: Non-dimensional wall pressure distributions for different $Re_m$ , with $Re_a = 11000$ and $z/d = 4$ .....	63
Figure 4-32: Non-dimensional wall shear stress distributions for different $Re_m$ , with $Re_a = 11000$ and $z/d = 4$ .....	64
Figure 4-33: Coating weight for different $V_{strip}$ and $Re_m$ , with $Re_a = 11000$ and $z/d = 4$ .....	65
Figure 4-34: Non-dimensional wall pressure distributions for different $Re_a$ , with $Re_m = 11000$ and $z/d = 4$ .....	66
Figure 4-35: Non-dimensional wall shear stress distributions for different $Re_a$ , with $Re_m = 11000$ and $z/d = 4$ .....	67
Figure 4-36: Coating weight for different $V_{strip}$ and $Re_a$ , with $Re_m = 11000$ and $z/d = 4$ .....	68
Figure 4-37: Non-dimensional (a) wall pressure (b) wall shear stress distributions for different $a/d$ ratios, with $Re_m = Re_a = 11000$ and $z/d = 4$ .....	69
Figure 4-38: Coating weight for different $a/d$ ratios and $V_{strip}$ .....	69
Figure 4-39: Schematic for a main with two adjacent inclined auxiliary impinging slot jets.....	71

Figure 4-40: Non-dimensional wall pressure distributions for different  $z/d$ , with  $s/d = 13.15$  and  $Re_m = Re_a = 11000$ .... 73

Figure 4-41: Non-dimensional shear stress distributions for different  $z/d$ , with  $s/d = 13.15$  and  $Re_m = Re_a = 11000$ .. 74

Figure 4-42: Comparison of non-dimensional maximum (a) wall pressure; and (b) shear stress for different  $z/d$  ratios.... 75

Figure 4-43: Pressure contour and streamlines with  $z/d = 4$ ,  $s/d = 13.15$  and  $Re_m = Re_a = 11000$ .... 76

Figure 4-44: Comparison of coating weight for a single-impinging slot jet and a main with two adjacent inclined auxiliary impinging slot jets for different  $z/d$  ratios, with  $V_{Strip} = 0.50$  m/s,  $Re_m = 11000$  and  $Re_a = 11000$ ..... 77

Figure 4-45: Coating weight for different  $V_{Strip}$  and  $z/d$  ratios with  $Re_m = Re_a = 11000$ ... 77

Figure 4-46: Non-dimensional wall pressure distributions for different  $Re_m$ , with  $Re_a = 11000$  and  $z/d = 4$ ..... 79

Figure 4-47: Non-dimensional wall shear stress distributions for different  $Re_m$ , with  $Re_a = 11000$  and  $z/d = 4$ ..... 79

Figure 4-48: Coating weight for different  $Re_m$  and  $V_{Strip}$  with  $z/d = 4$  and  $Re_a = 11000$ .... 80

Figure 4-49: Non-dimensional (a) wall pressure; and (b) wall shear stress distributions for different  $a/d$  ratios, with  $Re_m = Re_a = 11000$  and  $z/d = 4$ ..... 81

Figure 4-50: Coating weight for different  $V_{Strip}$  and  $Re_a$ , with  $Re_m = 11000$  and  $z/d = 4$ ..... 82

Figure 4-51: Coating weight for different  $V_{Strip}$  and  $Re_a$ , with  $Re_m = 11000$  and  $z/d = 10$ ..... 82

Figure 4-52: Coating weight for different  $s/d$  ratios, with  $V_{Strip} = 0.50$  m/s and  $Re_m = Re_a = 11000$  and  $z/d = 4$ ..... 83

Figure 4-53: Pressure under the centerline of the main slot jet with respect to time for  $s/d = 3.28$  ratios, with  $Re_m = Re_a = 11000$  and  $z/d = 4$ ..... 84

Figure 4-54: Coating weight for different turbulent impinging slot jet configurations with $V_{Strip} = 0.50 \text{ m/s}$ and $Re_m = Re_a = 11000$ and $z/d = 4$ .....	85
Figure A-1: Comparison of the coating thickness of Lacanette <i>et al.</i> [2006] experimental data with different turbulence models numerical data.....	101
Figure A-2: Non-dimensional wall pressure distributions for different $z/d$ ratios with $Re_m = 4500$ for case 1.....	102
Figure A-3: Non-dimensional wall pressure distributions for different $z/d$ ratios with $Re_m = 4500$ for case 2.....	103
Figure A-4: Non-dimensional wall pressure distributions for different $z/d$ ratios with $Re_m = 4500$ for case 3.....	103
Figure A-5: Non-dimensional wall pressure distributions for different $z/d$ ratios with $Re_m = 4500$ for case 4.....	104
Figure A-6: Non-dimensional wall pressure distributions for different $z/d$ ratios with $Re_m = 4500$ for case 5.....	104
Figure A-7: Non-dimensional wall shear stress distributions for different $z/d$ ratios with $Re_m = 4500$ for case 1.....	105
Figure A-8: Non-dimensional wall shear stress distributions for different $z/d$ ratios with $Re_m = 4500$ for case 2.....	105
Figure A-9: Non-dimensional wall shear stress distributions for different $z/d$ ratios with $Re_m = 4500$ for case 3.....	106
Figure A-10: Non-dimensional wall shear stress distributions for different $z/d$ ratios with $Re_m = 4500$ for case 4.....	106
Figure A-11: Non-dimensional wall shear stress distributions for different $z/d$ ratios with $Re_m = 4500$ for case 5.....	107

## List of Tables

Table 3-1: Standard $k - \varepsilon$ turbulence model constants.....	25
---	----

## Nomenclature

$a$	Wall distance between two jets [mm]
$b_p$	Half width of the pressure distribution [mm]
$b_\tau$	Location of the maximum shear stress [mm]
$C_{1\varepsilon}, C_{2\varepsilon}$ and $C_\mu$	Standard $k - \varepsilon$ turbulence model constants
$d$	Air-knife gap width [mm]
$g$	Gravitational constant [ $\text{m}/\text{s}^2$ ]
$G$	Non-dimensional effective gravitational acceleration
$G_k$	Production of turbulence kinetic energy [ $\text{N}/(\text{m}^3\text{s})$ ]
$h$	Local film thickness [m]
$h_f$	Final film thickness [m]
$H$	Non-dimensional film thickness
$k$	Turbulent kinetic energy [ $\text{N}\cdot\text{m}/\text{kg}$ ]
$l$	Length of the computational domain [mm]

$P$	Pressure along the sheet substrate [Pa]
$P_{max}$	Maximum pressure on the sheet substrate [Pa]
$q$	Volumetric flow rate per unit of film width [ $m^2/s^{-1}$ ]
$Q$	Non-dimensional withdrawal flux
$Re_a$	Auxiliary slot jet Reynolds number
$Re_m$	Main slot jet Reynolds number
$s$	Distance of the main slot jet to the auxiliary slot jet [mm]
$S$	Non-dimensional shear stress
$t$	Time [s]
$u$	Fluid velocity [m/s]
$u'$	Fluctuating velocity [m/s]
$\bar{u}$	Mean fluid velocity [m/s]
$u_\tau$	Friction velocity [m/s]
$V_{strip}$	Sheet substrate velocity [m/s]

$x$	Cartesian coordinate [m]
$y$	Cartesian coordinate [m]
$y^+$	Non-dimensional wall distance
$z$	Impingement distance [mm]

### *Greek Symbols*

$\delta_{ij}$	Kronecker delta
$\varepsilon$	Turbulent dissipation rate [N. m/kg]
$\mu$	Dynamic viscosity [Pa.s]
$\mu_\tau$	Turbulent viscosity [Pa.s]
$\nu$	Kinematic viscosity [m <sup>2</sup> /s]
$\rho$	Mass density [kg/m <sup>3</sup> ]
$\sigma_k$	Turbulent Prandtl number for kinetic energy
$\sigma_\varepsilon$	Turbulent Prandtl number for dissipation

$\tau$	Wall shear stress on the sheet substrate [Pa]
$\tau_{max}$	Maximum wall shear stress [Pa]
$\phi_i$	Scalar quantity
$\phi_i'$	Fluctuating scalar component
$\bar{\phi}_i$	Mean value of the scalar quantity
$\omega$	Specific dissipation rate [1/s]
$\xi_p$	Non-dimensional distance, $\xi_p = x/b_p$
$\xi_\tau$	Non-dimensional distance, $\xi_\tau = x/b_\tau$

### ***Abbreviations***

CGL	Continuous Galvanizing Line
DNS	Direct Numerical Simulation
EOC	Edge Over Coating
LES	Large Eddy Simulation
LDV	Laser Doppler Velocimetry

PIV	Particle Image Velocimetry
RANS	Reynolds Averaged Navier-Stokes
RMS	Root Mean Square
RNG	Re-Normalization Group
RSTM	Reynolds Stress Turbulence Model
SIMPLE	Semi-Implicit Method for Pressure-Linked Equations
SST	Shear Stress Transport



## **Chapter 1: Introduction**

### **1.1 Thesis Statement**

A numerical examination on air-knives with multiple-impinging slot jet configurations was performed to study the effect of wall pressure and wall shear stress distributions on the resultant coating weights for a moving sheet substrate over a range of process variables.

### **1.2 Motivation and Objectives**

In this research the application of an impinging slot jet in the hot-dip galvanizing line process is examined numerically. In this industrial process, steel is coated with molten zinc in order to shield it from corrosion. Zinc coated steel has many industrial applications, for example in the automobile industry and home appliances. An impinging slot jet is used to wipe excess zinc and control the coating weight on the moving steel sheet substrate by applying a controlled pressure gradient and shear stress distribution on the moving substrate after immersion in a bath of molten liquid zinc. Figure 1-1 shows a schematic of a conventional model of a single-impinging slot jet wiping excess zinc from the moving steel sheet substrate. The impinging jet wipes down the excess fluid from the moving substrate through the combined effect of pressure and shear stress distributions. According to this Figure, the excess zinc falls down into the bath of molten liquid zinc. The conventional model which is used in industry contains an air knife with a single-impinging slot jet of known gap that may vary along the length of the knife. In the

present work different geometries of multiple-impinging slot jets were studied numerically using computational fluid dynamics. The use of multiple-impinging slot jets in a hot-dip galvanizing line process is not common and in this research study different geometries of multiple-impinging slot jets were studied to determine the effect of wall pressure and shear stress distributions on the moving sheet substrate for different plate-to-nozzle ratios and Reynolds numbers on the resultant coating weights and compare the predicted results of multiple-impinging slot jets with the conventional model of a single-impinging slot jet.

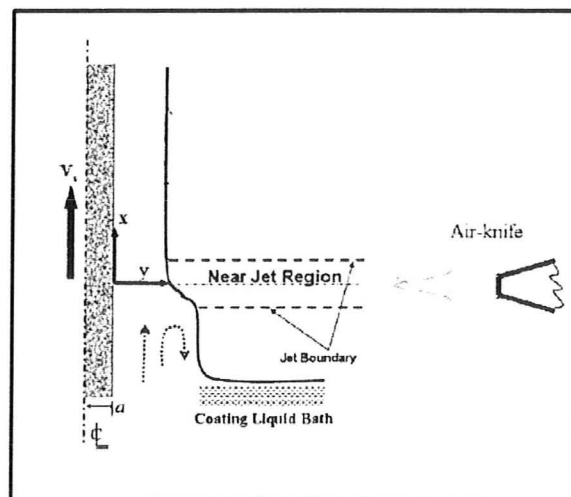


Figure 1-1: Schematic of a single-impinging slot jet case [Elsaadawy *et al.*, 2007].

A considerable body of work exists to model the coating weight using a single-impinging slot jet, which used both experimental and numerical methods to gain robust results in calculating the final film thickness on the moving substrate. Relatively little work has been done in using multiple-impinging slot jets in the hot-dip galvanizing process. In this study, we seek to understand the effect of different multiple-impinging

slot jets designs on the resultant wall pressure and shear stress distributions and consequently the final coating weight on the moving substrate. These configurations of multiple-impinging slot jets can be used not only in a hot-dip galvanizing line but also in cooling of electronic devices and turbine blades where heat removal from the substrate is a key target.

### **1.3 Thesis Layout**

The thesis consists of five chapters. The first chapter is an introduction to this research study. It commences with the thesis statement and continues with the motivation and objective of the research project. The first chapter ends up with the outline of the thesis. The subsequent four chapters are more technical in nature. The second chapter starts with a brief review on hot-dip galvanizing line process. It then focuses on different applications of air knives in industry, particularly in the continuous hot-dip galvanizing process for coating weight control. It continues with solving an analytical model for estimating the final coating weight on a moving substrate which was developed by solving the two-dimensional Navier-Stokes equations. The third chapter reviews the numerical methods which are used later to solve the Navier-Stokes equations in the computational domains of both configurations of a single-impinging slot jet and multiple-impinging slot jets. It contains a brief discussion on using different turbulence models in this field. Later on this chapter the standard  $k - \varepsilon$  turbulence model with non-equilibrium wall functions will be discussed in more depth; this model was used for turbulence modeling in the study's numerical domains. This chapter continues with

specifying the flow solver and discretization methods for the solution and ends with a discussion of the mesh types in the computational domains for each impinging jet configurations and the constraints on the mesh near the wall. Chapter four demonstrates numerical results and analysis for all impinging slot jets configurations. In the first section of this chapter the wall pressure and wall shear stress distribution results for different plate-to-nozzle ratios and main jet Reynolds numbers and the resultant coating weight for a single-impinging slot jet case demonstrates a base case for comparison with other configurations of multiple-impinging slot jet cases. In the second section, there is a discussion on the results for different configurations of multiple-impinging slot jet cases for which the geometry will be discussed later in the chapter. The coating weight results for each version of the modified multiple-impinging slot jets is then compared with the coating weight data of a single-impinging slot jet. In the fifth chapter, various suggestions are proposed for future work which can be done in the area of impinging slot jets and modifying and validating the numerical results.

An additional section is provided at the end of the thesis in Appendix A which studied the sensitivity of the coating weight for a single-impinging slot jet case to different turbulence models for different plate-to-nozzle ratios. The numerical results are compared with the experimental data of Lacanette *et al.* [2006] in order to validate the results from the different turbulence models.

## Chapter 2: Literature Review

This chapter introduces the continuous hot-dip galvanizing process in brief, continues with a description of turbulent impinging slot jets and their applications in the hot-dip galvanizing line process.

### 2.1 Continuous Hot-Dip Galvanizing Line Process

Figure 2-1 shows a schematic of the pot region in a continuous hot-dip galvanizing line. In this process, a steel sheet substrate is submerged in a hot dip bath of molten liquid zinc, around 460°C, in which the molten metal solution is deposited on the moving sheet substrate. The substrate should be clean before immersion in to the hot bath in order to remove any surface oxide that may prevent reactive wetting in the zinc pot [Marder, 2000].

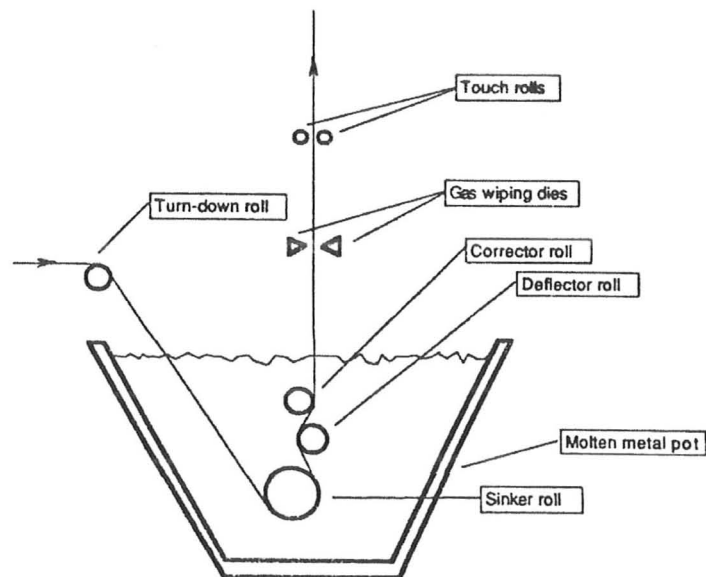


Figure 2-1: Schematic of a pot region in continuous hot-dip galvanizing line [Marder, 2000].

After dipping the substrate, the excess liquid zinc is removed from the moving sheet substrate by using turbulent impinging slot jets, which control the coating thickness on the moving substrate. The coating weight is monitored continuously using X-Ray coating thickness measurement equipment. After wiping the excess zinc from the surface, the sheet is cooled by forced air or subjected to heat treatment (called galvannealing) before being coiled or sheared into cut lengths at the exit of the line [Marder, 2000].

## 2.2 Air Knife Coating

An air knife, essentially an impinging slot jet, is a device which is used in various industrial applications, such as dryers, forming of plastic, annealing of metal and glass, cooling of electronic devices, cooling of turbine blades, drying of textiles and paper, and in the hot-dip galvanizing process as a wiping actuator.

There is a considerable body of previous work available in the area of impinging jets, most of which focuses on examining heat transfer to the substrate using different impinging jet configurations [Striegl and Diller, 1984; Kataoka et al, 1987; Kataoka, 1990; Gau and Chung, 1991; Gau and Lee, 1992; Sakakibara *et al.*, 1997; Sarkar *et al.*, 2004].

Maurel and Solliec [2001] studied turbulent impinging slot jet using laser Doppler velocimetry (LDV) and particle image velocimetry (PIV) to analyze the flow field. The velocity field of the impinging slot jet consists of zones which were studied thoroughly in their work. The first region which is quite important is called the *potential core zone*. In

this zone, the centerline velocity of the slot jet does not change significantly from the exit velocity of the jet and remains constant. The length of the potential core vary between  $3d$  and  $6d$  ( $d$ =jet width at the exit) and is strongly dependant on the initial conditions. The second zone is the *transition zone* where Maurel and Sollicec [2001] present an analytical solution for non-dimensional jet velocity as presented by Schlichting [1968]. The third region is called the *developed zone* where Beltaos and Rajaratnam [1976] provided a correlation for the non-dimensional velocity profile. The final region is called the *impinging zone* (or *recompression zone*) which has quite a complex velocity profile.

There are relatively few studies available in the literature on using turbulent impinging slot jet for wiping liquid zinc from the moving substrate. The method of coating weight approximation will be discussed in detail in the next section. One of the fundamental works in this area was done by Thornton and Graff [1976], which incorporated the effect of the maximum wall pressure gradient. Ellen and Tu [1984] developed a new method in which the effect of wall shear stress distribution was included in the boundary conditions for the coating weight model. It was shown that in using wall shear stress in the analytical model enhanced the correlation between the predicted coating weight and industrial line results for certain process parameter combinations. Tu and Wood [1996] measured wall pressure and shear stress distributions experimentally for a broad range of plate-to-nozzle ratios,  $2 < z/d < 20$ , and Reynolds number,  $3000 < Re_m < 11000$ , beneath a turbulent impinging slot jet. The wall pressure distributions were nearly Gaussian for  $z/d \geq 10$  and independent of Reynolds number, while the wall shear stress distributions were dependant on both the  $z/d$  ratio and  $Re_m$ . The wall shear

stress was measured using Stanton probes, where the Stanton tube with a 0.05 mm-high probe gave the most accurate results. Guo and Wood [2002] did measurements using a plane impinging jet onto a flat plate. In their work the wall shear stress distribution was compared to an analytical solution for the laminar development. The free stream turbulence was around 0.35% at the jet exit while for Tu and Wood [1996] was around 4%. By comparing the wall shear stress results of these two works, they concluded that the turbulence level had only a second-order influence on the wall shear stress around the stagnation region.

Hrymak *et al.* [2004] used computational methods to predict the wall pressure and wall shear stress distributions on the sheet substrate with the goal of improving the coating weight results for low impingement ratios. The predicted results were in an excellent agreement with the industrial data for low coating weights, while the numerical model was less accurate for high coating weights. This work also investigated the effects of variable slot width profiles, e.g. bow-tie profiled air knives, on the coating weight.

Naphade *et al.* [2005] developed a mathematical model for predicting the coating weight on a moving substrate. The proposed model estimated the coating weight as a function of strip velocity, jet nozzle pressure, plate-to-nozzle distance and nozzle gap width. The wall pressure results and wall shear stress distributions were calculated using FLUENT. The proposed correlation was validated with industrial line data (CGL#2 of Tata Steel) and the experimental results of Buchlin *et al.* [1996].

Elsaadawy *et al.* [2007] modified the pressure gradient distributions and shear stress results correlations of Ellen and Tu [1984]. Lacanette *et al.* [2005] studied the effect of turbulent impinging slot jet on a moving film. The interaction of the flow between the turbulent impinging slot jet and the liquid film makes the problem quite difficult. Figure 2-2 shows the time evolution of the film thickness for a fixed point throughout the wiping process. It is shown that after 0.50 s the film thickness does not change significantly at the defined location. Lacanette *et al.* [2005] visualized the shape of the liquid on the moving substrate for different zones. Figure 2-3(a) shows the liquid shape in the impingement region where the impinging jet bends the liquid on the substrate. Figure 2-3(b) shows the liquid profile upstream of the impingement region where the excess zinc wipes back into the zinc pot. Figure 2-3(c) represents the liquid profile downstream of the impingement region, where the coating weight is stable and does not change with time.

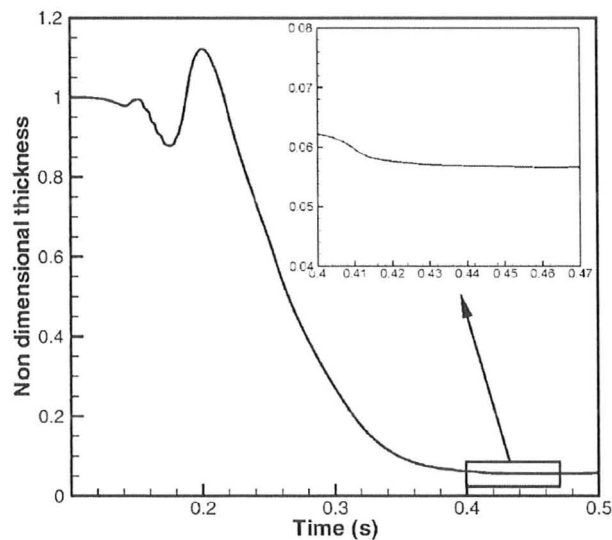


Figure 2-2: Time evolution of the film thickness throughout the wiping process [Lacanette *et al.*, 2005].

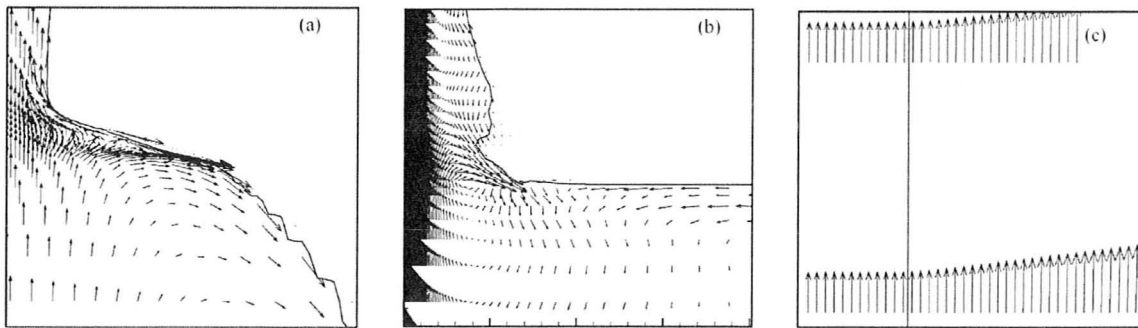


Figure 2-3: Visualization of the liquid film: (a) the impingement region; (b) upstream of the impingement region; (c) downstream of the impingement region [Lacanette *et al.*, 2005].

The application of turbulent impinging slot jets is limited due to liquid droplet emission upstream from the slot jet, called splashing. The splashing results produce defects, increase equipment maintenance and are a potential worker safety issue. Lacanette *et al.* [2006] studied this phenomenon using both numerical and experimental techniques, while Gosset and Buchlin [2007] studied this occurrence experimentally using two different impinging slot jet configurations. Both Lacanette *et al.* [2006] and Gosset and Buchlin [2007] used water as a liquid film on the moving substrate as an alternative to using molten liquid zinc. Figure 2-4(a) shows splashing in a hot-dip galvanizing line, while Figure 2-4(b) demonstrates that this phenomenon can be reproduced on a water model facility. Splashing investigation is beyond the scope of this project and the enthusiastic reader should review Yoneda [1993] for detailed information about film liquid instability.

Kim *et al.* [2003] investigated edge over coating (EOC) numerically near the edge of a galvanized steel substrate. According to the literature, the coating weight at the edge of the sheet substrate is 1.4-1.8 times larger than at the middle of the strip. In this work, a

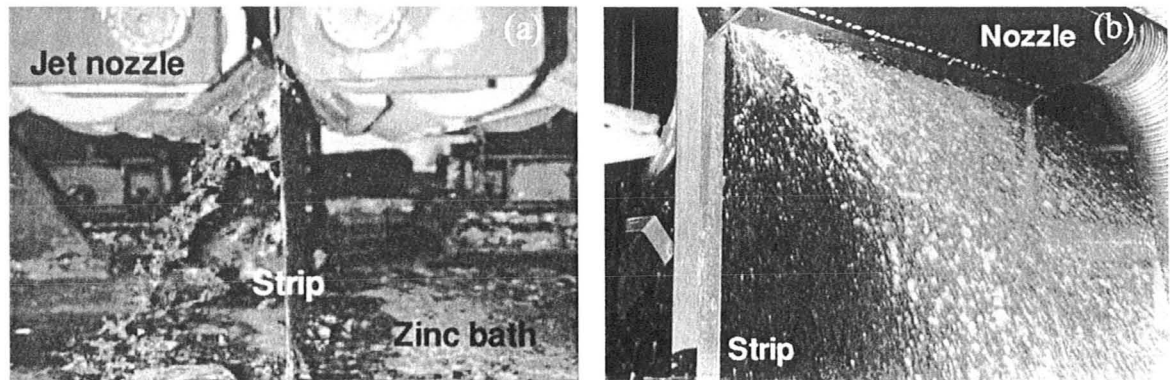


Figure 2-4: (a) Splashing in hot-dip galvanizing line; and (b) splashing on the substrate with water [Gosset and Buchlin, 2007].

3-D flow field of the impingement region was developed using a commercial code, STAR-CD. The vortices created at the edge of the strip by collision of two opposing jets (Figure 2-5(a)) causes a pressure drop on the sheet substrate which makes the coating weight increase at the edge of the substrate. EOC can be remedied by adjusting the impinging nozzle close to the strip or by adding a baffle plate parallel to the sheet substrate (Figure 2-5(b)).

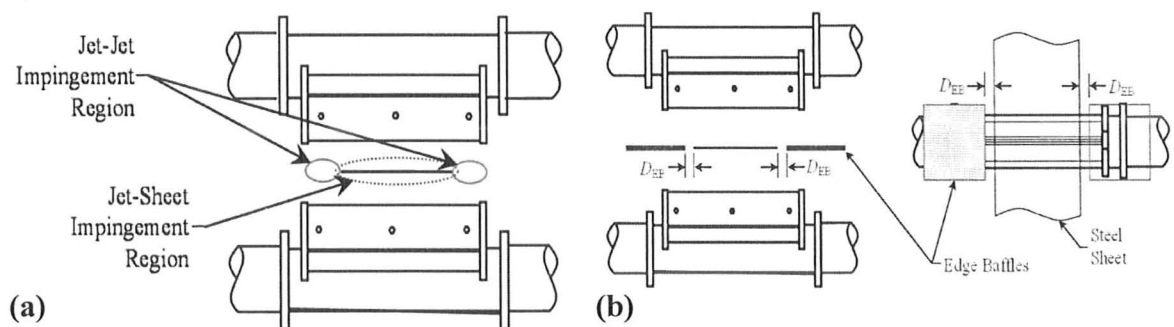


Figure 2-5: (a) Two opposing impinging slot jets without baffle; and (b) Two opposing impinging slot jets with baffle [Arthurs, 2007].

Ahn and Chung [2006] proposed a method to prevent EOC based on numerical analysis to investigate their proposed design. They concluded that when two opposing

jets collide at an angle less than  $180^\circ$ , the alternating vortices vanish at the edge of the sheet substrate. By eliminating the vortices at the edge of the sheet substrate, the wall pressure across the flat surface becomes quite uniform. When the pressure across the sheet substrate is constant, the predicted coating weight is consistent over the substrate section. Gilchrist *et al.* [1988] showed that a jet flows along the attached curved surface due to the Coanda effect (Figure 2-6). Ahn and Chung [2006] used this technique to change the direction of the jet flow by adding a small diameter cylinder at the lower lip of the impinging slot jet. By this method, the opposing jets collide at an angle lower than  $180^\circ$ , which makes the vortical structures disappear at the edge of the substrate.

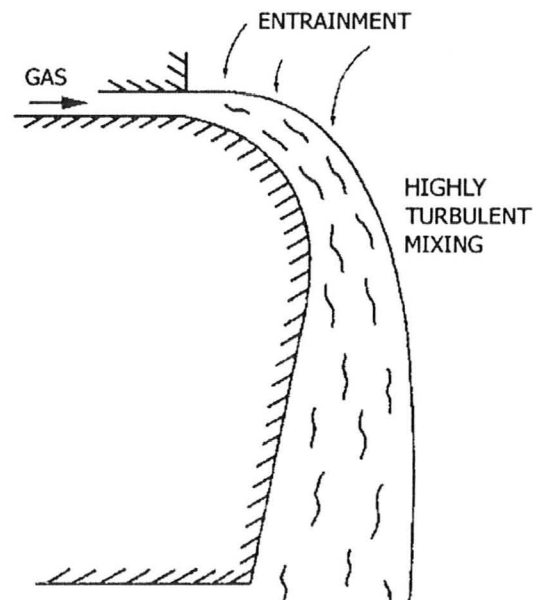


Figure 2-6: Deflection of the flow due to the Coanda effect [Ahn and Chung, 2006].

Cho *et al.* [2009] studied the effect of air knife tilting on the predicted coating thickness. To decrease the effect of splashing in the hot-dip galvanizing process, a new

design of air knife was proposed with a constant rate of expansion. The effects of expansion rate of the nozzle, sheet substrate velocity and tilt angle on the coating thickness were examined. The new design saves energy in comparison with the conventional design, while the effect of expansion rate of the nozzle on the coating thickness was quite negligible. Tilting the air knife around  $5^\circ$  is effective in restraining film splashing. Lee *et al.* [2007] used this design method to reduce the splashing problem on the surface. They concluded that a deflection angle of  $9^\circ$  was the most effective way to reduce splashing on the sheet substrate and have a thin coating weight on the substrate due to the increment in wall shear stress and pressure gradient.

Yoon and Chung [2010] studied the effect of check-mark stain on steel sheet substrates coated with zinc. Check-mark stain is the tilted pattern on the coating surface and is a serious industrial defect. Stream-wise vortices impinging on the sheet substrate periodically caused the check-mark stain on the flat surface. They designed a new model of impinging slot jet with one main slot jet which operates as a wiping actuator and a guide jet to decrease the flow instability of the main slot jet. The guide jet prevented the formation of vortical structures on the impingement surface. By removing the vortical structures on the flat surface, the check-mark stain restrains effects decreased significantly. Parametric studies were done to determine the optimum design for the proposed configuration. The flow field was simulated as a 3-D unsteady compressible turbulent flow using FLUENT.

Tu [1993, 1994] proposed new designs of turbulent impinging slot jets with multiple nozzles which can be used in the hot-dip galvanizing process. Two of the

proposed models are studied in this research project: two parallel impinging slot jet configurations and a main jet with inclined auxiliary impinging slot jets. However the effect of these proposed models on the wall pressure and wall shear stress distributions was not proposed. According to the present study, the wall pressure results and wall shear stress distributions are calculated numerically for the above configurations. The results obtained are used to estimate the coating weight on the moving sheet substrate and compared to the conventional model of a single-impinging slot jet case.

Kim *et al.* [2008] designed a multiple-impinging slot jet with one main slot jet and two adjacent inclined auxiliary slot jets discharging air at lower velocity in comparison with the main slot jet. This configuration is applicable to the continuous hot-dip galvanizing process for coating weight control. The above model is studied numerically to find a trend between the coating weight results of this model and the conventional model. The predicted coating weight results for all configurations are reported in Chapter 4.

### **2.3 Coating Thickness Model Estimation**

The final film thickness can be obtained by solving the two-dimensional Navier-Stokes equation [Thornton and Graff, 1976; Ellen and Tu, 1984] for a liquid film using the following assumptions. It should be assumed that the molten zinc is steady state, isothermal and incompressible with constant viscosity and density. The pressure across the liquid film is assumed constant due to the fact that the film velocity perpendicular to the plate is negligible compared to the flow velocity parallel to the substrate. It is

assumed that the effect of surface roughness, surface tension and oxidation are not significant. The simplified Navier-Stokes equation for the liquid film is written as:

$$\mu \frac{d^2u}{dy^2} = \rho g + \frac{dp}{dx} \quad (2-1)$$

here,  $u$  is the liquid film velocity,  $p$  is the pressure along the sheet substrate created by the turbulent impinging jet,  $\mu$  is the zinc viscosity,  $\rho$  the density of liquid zinc and  $g$  the gravitational constant. Equation (2-1) expresses the viscous shear forces on the substrate being in balance with gravitational forces and the pressure gradient on the surface. The boundary conditions for solving the above equation are written as:

$$u = V_{Strip} \quad \text{at } y=0 \quad (2-2)$$

$$\tau = \mu \frac{du}{dy} \quad \text{at } y=h \quad (2-3)$$

where  $\tau$  is the shear stress imposed by the turbulent impinging slot jet on the strip,  $V_{Strip}$  is the strip velocity and  $h$  film thickness on the moving strip. By integrating Equation (2-1) and applying the above boundary conditions results in the following solution:

$$\frac{u}{V_{Strip}} = \left(1 + \left(\frac{y}{h}\right)SH - \left(\frac{y}{h}\right)\left(2 - \frac{y}{h}\right)\frac{GH^2}{2}\right) \quad (2-4)$$

here,  $S = \frac{\tau}{\sqrt{\rho\mu V_{Strip}g}}$  is the non-dimensional shear stress,  $H = h\sqrt{\frac{\rho g}{\mu V_{Strip}}}$  is the non-dimensional film thickness and  $G = 1 + \frac{1}{\rho g} \frac{dp}{dx}$  is the effective gravitational acceleration.

The remaining vertical mass flow rate at any position is equal to the strip velocity multiplied by the final coating mass due to the conservation of mass. As a result the zinc flux,  $q$ , is written as follows:

$$q = \int_0^h u dy = V_{strip} h \left( 1 + \frac{SH}{2} - \frac{GH^2}{3} \right) \quad (2-5)$$

The non-dimensional withdrawal flux,  $Q = \frac{q}{V_{strip}} \sqrt{\frac{\rho g}{\mu V_{strip}}}$ , Equation (2-5) converts to:

$$Q = -\frac{GH^3}{3} + \frac{SH^2}{2} + H \quad (2-6)$$

The non-dimensional film thickness,  $H$ , resultant from the theoretical maximum withdrawal flux,  $Q_{Max}$ , is a function of  $S$  and  $G$  for any position on the sheet substrate is written as:

$$H = \frac{S \pm \sqrt{S^2 + 4G}}{2G} \quad (2-7)$$

It was shown that the non-dimensional film thickness,  $H$ , and the maximum non-dimensional withdrawal flux,  $Q_{Max}$ , is a function of  $S$  and  $G$  at any position on the sheet substrate. The final film thickness can be obtained by using the minimum value of the predicted non-dimensional maximum withdrawal flux,  $(Q_{Max})_{Min}$ , on the substrate. Once the liquid zinc solidifies, the film velocity is equal to the substrate velocity and the final film thickness is written as:

$$h_f = \frac{(Q_{Max})_{Min}}{\sqrt{\frac{\rho g}{\mu V_{Strip}}}} \quad (2-8)$$

According to Equation (2-8), in order to estimate the final film thickness on the moving sheet substrate, the wall pressure gradient and wall shear stress distributions are required. Lacanette *et al.* [2006] and Myrillas *et al.* [2009] used the maximum pressure gradient and maximum shear stress parameters in Equation (2-7) in order to estimate the coating thickness on a moving substrate.

In this research project, the obtained wall pressure distributions and wall shear stress results were used as inputs in an analytical solution (Equation (2-7)) to calculate the coating weight on the moving sheet substrate. The numerical methods used to solve the model are described in the following chapter.

## Chapter 3: Simulation Models

This chapter commences with introducing the Navier-Stokes equations and continues with presenting the various turbulence models which are appropriate for impinging slot jet modeling. It then introduces the Reynolds-Averaged Navier-Stokes (RANS) equations and the estimation method for Reynolds stresses. This chapter continues with introducing the transport equations for the standard  $k - \varepsilon$  turbulence model and the wall functions applied in the computational domain. In the next section, it presents the flow solver and discretization methods which are used for all configurations. This chapter comes to an end with explaining the mesh types for all configurations of a single-impinging slot jet and multiple-impinging slot jets and the constraints on the mesh size near the wall.

### 3.1 Navier-Stokes Equations

Fluid flow can be represented by the Navier-Stokes equations which contain the mass and momentum balance equations. The mass and momentum equations, respectively in Cartesian form can be written as:

$$\frac{\partial \rho}{\partial t} + \frac{\partial(\rho u_i)}{\partial x_i} = 0 \quad (3-1)$$

$$\frac{\partial \rho u_i}{\partial t} + \frac{\partial \rho u_i u_j}{\partial x_i} = -\frac{\partial p}{\partial x_i} + \frac{\partial}{\partial x_i} \left[ \left( \frac{\partial u_i}{\partial x_j} + \frac{\partial u_j}{\partial x_i} \right) \right] \quad (3-2)$$

The above equations represent the governing equations for fluid flow in general. In order to solve the above equations, a suitable method should be employed which is the subject of the next section.

### 3.2 Turbulence Modeling

Most engineering problems in fluid dynamics are turbulent in nature. There is not a universal method for computing the turbulence parameters in computational fluid dynamics. The ultimate aim is to obtain a tractable quantitative theory or model to calculate turbulence properties [Pope, 2000]. There are many turbulence models available for capturing turbulence parameters. Theoretically the simplest method is to solve the Navier-Stokes equations without any approximation or averaging of the turbulence quantities. The Navier-Stokes equations are solved directly by numerical discretization such that the numerical errors can be calculated and controlled approximately [Ferziger and Perić, 2002]. In this method, comprehensive information of the flow field is achieved which is not very useful for engineering applications. The computational time for solving each problem using direct numerical simulation (DNS) method is very costly because the mesh used in this technique should be fine enough to capture the dissipative scale of the flow field. The computational requirements for the DNS method rise so sharply by increasing the Reynolds number that the approach is only applicable for low or moderate Reynolds numbers [Pope, 2000]. This criterion leads to fine grid sizes in the computational domain. There has not been satisfactory research conducted using the DNS method for turbulent impinging slot jets, especially for the hot-dip galvanizing process. Chung *et al.* [2002] studied the momentum and heat transfer of

unsteady planar impinging jets at low Reynolds numbers using DNS. Hattori and Nagano [2004] used this technique to study the flow field and heat transfer for a single-impinging slot jet for a confined space.

Another method used for calculating the turbulence parameters in the flow field is by using the large eddy simulation (LES) method in the computational domain. In this method, larger three-dimensional unsteady turbulence structures are directly solved, while the smaller-scale motions are modeled mathematically [Pope, 2000]. The computational cost for LES is between that of the DNS and Reynolds-stress models. Voke *et al.* [1995] and Cziesla *et al.* [2001] studied the flow field of impinging slot jet using the LES method. Beaubert and Viazzo [2003] investigated a planar impinging jet with large eddy simulation (LES) using the dynamic Smagorinsky model. In this work all of the LES results are compared with experimental data. The above work inspected the flow field and heat transfer of the impinging slot jet on a flat surface thoroughly; however they did not study the effect of the impinging jet on the coating weight on the moving substrate, which is the key objective of this research. Lacanette *et al.* [2006] did an inclusive study on a single-impinging slot jet in a hot-dip galvanizing line using both the LES turbulence model and experimental validation. In their numerical model, the turbulent impinging jet and liquid coating are solved as a two-phase flow problem where the gas-jet and liquid film on the moving substrate were modeled together. The resulting numerical model permits the prediction of splashing on the moving substrate. Myrillas *et al.* [2009] studied a single-impinging slot jet using the LES turbulence model and compared the simulation results with analytical modeling, experimental validation and

realizable  $k - \varepsilon$  turbulence model data. The predicted LES results were in a good agreement with analytical and experimental method, while were not appropriate for the  $k - \varepsilon$  model.

Another class of turbulence models which have been extensively employed in engineering applications are two-equation models. In two-equation turbulence models, there are two additional transport equations to capture the turbulence properties of the flow field. One of the transport equations solves for the turbulent kinetic energy ( $k$ ) and the other transport equation depends on whether the turbulent dissipation rate ( $\varepsilon$ ) or the specific dissipation rate ( $\omega$ ) is to be solved. In this method the mean velocity field is determined by solving the Reynolds equations [Pope, 2000] and the Reynolds stresses are approximated by a turbulence model. There has been a considerable body of work performed using RANS models to capture the turbulence parameters for impinging slot jets. Naphade *et al.* [2005] and Elsaadawy *et al.* [2007] studied the flow field of a single-impinging slot jet in a hot-dip galvanizing line using Reynolds-number renormalization group (*RNG*) based on the  $k - \varepsilon$  turbulence model and the standard  $k - \varepsilon$  turbulence model correspondingly. Fernández *et al.* [2007] did inclusive research on using the standard and realizable  $k - \varepsilon$  and the standard  $k - \omega$  turbulence models for dual-impinging slot jets on a flat surface. They predicted that the above turbulence models underestimate the jet expansion rate and none of the above models estimate the flow field in the impingement region precisely, but are appropriate models for engineering purposes. Leschizner [1993] concluded that the Reynolds stress turbulence model (*RSTM*) is superior to the  $k - \varepsilon$  model for swirling jets and in a large recirculation flow

region but the computational results for impinging slot jets for both turbulence models are approximately the same. The turbulence model which is used in this research project for all cases is the standard  $k - \varepsilon$  model. The reason for selecting this turbulence model for capturing the turbulence quantities in the computational domains of impinging slot jets is twofold. First, the resultant coating weight for a single-impinging slot jet was in good agreement with industrial galvanizing line data [Elsaadawy *et al.*, 2007], which makes this model acceptable for engineering application. Also, solving the numerical domain through this turbulence method is less costly in computational time than the other schemes such as DNS or LES. In the next section of this chapter the RANS method and the standard  $k - \varepsilon$  turbulence model will be discussed in depth.

### 3.2.1 Reynolds-Averaged Navier-Stokes (RANS) Equations

In the RANS equations the solution variables are written in the form of mean and fluctuating elements. The velocity components are written as:

$$u_i = \bar{u}_i + u_i' \quad (3-3)$$

where  $\bar{u}_i$  and  $u_i'$  are the mean and fluctuating velocity elements respectively ( $i = 1,2,3$ ).

The other scalar components are described by:

$$\phi_i = \bar{\phi}_i + \phi_i' \quad (3-4)$$

where  $\phi$  indicates a scalar element in the Navier-Stokes equations. By decomposing the solution variables and inserting them in (3-1) and (3-2) and then taking an average on the

solution variables the Reynolds-Averaged Navier-Stokes (RANS) equations are derived.

The RANS equations can be written as:

$$\frac{\partial \rho}{\partial t} + \frac{\partial(\rho \bar{u}_i)}{\partial x_i} = 0 \quad (3-5)$$

$$\frac{\partial \rho \bar{u}_i}{\partial t} + \frac{\partial \rho \bar{u}_i \bar{u}_j}{\partial x_j} = -\frac{\partial p}{\partial x_i} + \frac{\partial}{\partial x_i} \left[ \mu \left( \frac{\partial \bar{u}_i}{\partial x_j} + \frac{\partial \bar{u}_j}{\partial x_i} \right) - \rho \overline{u'_i u'_j} \right] \quad (3-6)$$

The form of equations (3-5) and (3-6) are the same as Navier-Stokes equations in section 3.1 except for an additional property in equation (3-6) which characterizes the Reynolds stresses. In the next section, the Reynolds stress model is discussed along with the advantages and disadvantages of this modeling approach.

### 3.2.2 The Turbulent-Viscosity Model

The turbulent-viscosity postulation ( $\mu_T$ ), which is later used in the standard  $k - \varepsilon$  turbulence model, relates the Reynolds stresses to the mean velocity gradients of the flow [Pope, 2000]. The relationship is written as follows:

$$\overline{\rho u'_i u'_j} - \frac{2}{3} \rho k \delta_{ij} = -\mu_T \left( \frac{\partial \bar{u}_i}{\partial x_j} + \frac{\partial \bar{u}_j}{\partial x_i} \right) \quad (3-7)$$

In the above equation, the turbulent kinetic energy ( $k$ ) is defined as  $\frac{1}{2} \overline{u'_i u'_i}$ . The advantage of this approximation is the comparatively low computational price, while the weakness of this approach is that it supposes that the turbulence viscosity is an isotropic scalar quantity, which is likely not true within the flow impingement region on the flat surface where there are a high flow curvature and severe pressure gradients.

### 3.2.3 Standard $k - \varepsilon$ Turbulence Model

The standard  $k - \varepsilon$  turbulence model consists of two transport equations which solve the turbulent kinetic energy and turbulent dissipation rate. The transport equations are as follows:

$$\frac{\partial \rho k}{\partial t} + \frac{\partial \rho k u_i}{\partial x_i} = \frac{\partial}{\partial x_j} \left[ \left( \mu + \frac{\mu_t}{\sigma_k} \right) \frac{\partial k}{\partial x_j} \right] + G_k - \rho \varepsilon \quad (3-8)$$

$$\frac{\partial \rho \varepsilon}{\partial t} + \frac{\partial \rho \varepsilon u_i}{\partial x_i} = \frac{\partial}{\partial x_j} \left[ \left( \mu + \frac{\mu_t}{\sigma_\varepsilon} \right) \frac{\partial \varepsilon}{\partial x_j} \right] + C_{1\varepsilon} \frac{\varepsilon}{k} (G_k) - C_{2\varepsilon} \rho \frac{\varepsilon^2}{k} \quad (3-9)$$

Equations (3-8) and (3-9) represent the turbulent kinetic energy ( $k$ ) and turbulent dissipation rate ( $\varepsilon$ ) correspondingly.  $G_k$  stands for the production of turbulent kinetic energy due to the mean velocity gradients and  $C_{1\varepsilon}$  and  $C_{2\varepsilon}$  are model constants. In the above equations,  $\sigma_k$  and  $\sigma_\varepsilon$  are turbulent Prantl numbers for the turbulent kinetic energy and dissipation rate, respectively. The turbulent viscosity model for the standard  $k - \varepsilon$  turbulence model is written as follows:

$$\mu_t = \rho C_\mu k^2 / \varepsilon \quad (3-10)$$

where  $C_\mu$  is a model constant. Table 3-1 represents the standard  $k - \varepsilon$  model constants for the above equations due to Launder and Sharma [1974]. The model constants in Table 3-1 are not universal and can be customized in the code for different applications. For instance Tzeng *et al.* [1999] investigated numerical heat transfer under confined impinging slot jets using  $k - \varepsilon$  turbulence model through eight different model constants proposed by different researchers and compared the experimental data to these model

coefficients. In the next section, there is a brief introduction to the wall functions used for impinging slot jets in this research.

Table 3-1: Standard  $k - \varepsilon$  turbulence model constants

$C_\mu$	$C_{1\varepsilon}$	$C_{2\varepsilon}$	$\sigma_k$	$\sigma_\varepsilon$
0.09	1.44	1.92	1	1.3

### 3.2.4 Wall Functions

Wall functions are a collection of semi-empirical formulas and functions which relate the solution variables near-wall cells and the corresponding quantities at the wall [FLUENT 6.3 User's Guide, 2006]. There are three proper wall functions offered in FLUENT as: standard wall functions, non-equilibrium wall functions and enhanced wall treatment. Elsaadawy *et al.* [2007] made a comparison between the experimental wall shear stress distribution data of Tu and Wood [1996] and the computational results of both standard and non-equilibrium wall functions and found a good agreement between the experimental and numerical results by selecting the non-equilibrium wall functions. In this research project the non-equilibrium wall functions were used for simulation of all impinging slot jet configurations. All of the equations for the non-equilibrium wall treatment were represented by Kim and Choudhury [1995]. The non-equilibrium wall functions account for the effect of pressure gradients in their terms and are highly recommended for use in complex flows such as separation, reattachment and impinging regions [FLUENT 6.3 User's Guide, 2006].

### 3.3 Discretization Method

A double precision solver was used for all simulations. The segregated solver was used for the governing equations. The standard method was used for pressure term with a first order upwinding scheme for the turbulent kinetic energy ( $k$ ), turbulent dissipation rate ( $\epsilon$ ) and momentum. The SIMPLE method was employed for pressure-velocity coupling. The governing equations were solved using FLUENT computational fluid dynamics commercial code at each time step until the root-mean-square (RMS) relative residuals of all governing equations fell below  $10^{-5}$ . For each configuration of a single-impinging slot jet case and multiple-impinging slot jet cases, 15 seconds of flow field data were simulated. The time step for the computational model is  $2 \times 10^{-4}$  second to resolve time dependant flow fields. The pressure gradients and shear stress distributions, which play major roles in determining the coating weight on the flat surface, reached steady state after 5 to 10 seconds of real time flow depending on the main slot jet Reynolds number and plate-to-nozzle ratio.

### 3.4 Mesh

The mesh for all configurations was generated with GAMBIT. The mesh used for a single-impinging slot jet was comprised of quadrilaterals (Figure 3-1(a)). In order to check for mesh independence, refinement was done for all configurations for each plate-to-nozzle ratio. The number of nodes for a single-impinging slot jet varied between 70,000 and 130,000 depending on the  $z/d$  ratio. The mesh size for all modified version of multiple-impinging slot jet configurations was refined near the impingement wall and

the jet centerline about two times for each  $z/d$  ratio to check the independence of the solution to the mesh size. The mesh used for multiple-impinging slot jets was comprised of both quadrilaterals and triangles (Figure 3-1(b)). The number of nodes for different configurations of multiple-impinging slot jets varied from 95,000 to 183,000 depending on the  $z/d$  ratio.

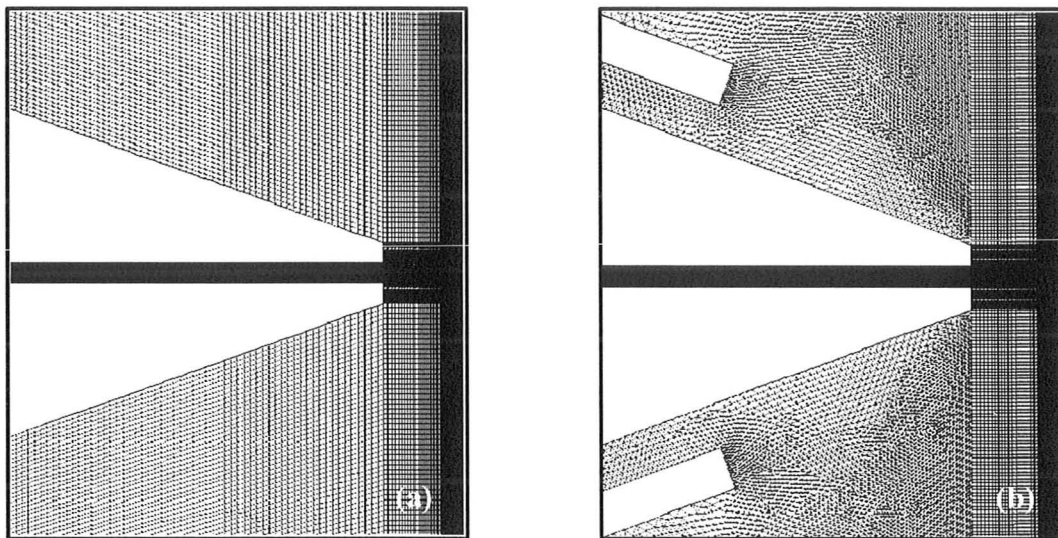


Figure 3-1: (a) The quadrilaterals mesh close to the centerline of the main jet for a single-impinging slot jet; and (b) The quadrilaterals mesh close to the centerline of the main jet and triangles near the auxiliary slot jets for multiple-impinging slot jets.

The  $y^+ = u_\tau y / \nu$  is the non-dimensional wall distance where  $u_\tau$  is the friction velocity,  $y$  is the distance of the first node near the wall and  $\nu$  is the kinematic viscosity. The  $y^+$  on the impingement plate should be checked for each simulation to make sure that it is in the log-law region where  $y^+$  changes between 30 to 300. The mesh near the impingement plate should be either coarse or fine to prevent  $y^+$  lying within the buffer layer and/or viscous sublayer regions. In the impingement region, where there are severe pressure gradient, the  $y^+$  tends to go to zero which deviates from the criteria of being

placed in the log-law region. This results in 8-10 nodes being outside the log-law region. However the number of these nodes is insignificant in comparison to the total number of nodes on the plate. The effect of this deviation on the wall pressure results and wall shear stress distributions are reasonably insignificant.

## Chapter 4: Numerical Analysis

This chapter begins with discussing the results of the wall pressure and shear stress distributions and the resultant coating weights for a single-impinging slot jet for different plate-to-nozzle ratios and Reynolds numbers. The coating weight estimation method was proposed in Chapter 2. The results of the flow field and coating weights for a single-impinging slot jet were a base case for comparison with modified multiple-impinging slot jet configurations. This chapter continues with examining the flow fields and coating weights of two parallel impinging slot jets for different plate-to-nozzle ratios, main jet Reynolds numbers and wall thickness-to-nozzle ratio effect. Later in this chapter, a modified configuration for the multiple-impinging slot jets is introduced, which consists of one main slot jet with one inclined auxiliary slot jet that discharges air at lower velocity in comparison with the main slot jet. The above configuration was proposed by Tu [1994]. Another multiple-impinging slot jet configuration consisted of one main slot jet with two adjacent inclined auxiliary slot jets [Kim *et al.*, 2008] discharging air at lower velocities in comparison with the main slot jet. The coating weight for different configurations of multiple-impinging slot jets were compared with the conventional model of a single-impinging slot jet.

### 4.1 Single-Impinging Slot Jet

Single-impinging slot jet results are briefly reviewed in this section with the goal of estimating the coating weights for different plate-to-nozzle ratios and main slot jet Reynolds numbers.

#### 4.1.1 Geometry, Boundary and Initial Conditions

The single-impinging slot jet consists of a main slot jet discharging air on the flat substrate. Figure 4-1 demonstrates the geometry for a single-impinging slot jet, where  $z$  represents the distance of the main slot jet to the strip.  $d$  is the nozzle gap which is fixed to  $1.52\text{ mm}$  in this study, but in practice can be varied both in average gap and in gap profile.  $l$  is the length of the computational domain and for all of the simulations is set to  $l/d = 100$ , which captures the far-field boundary condition. The velocity inlet condition was defined for a single-impinging slot jet and the Reynolds number is based on the width of the nozzle gap and inlet velocity magnitude.

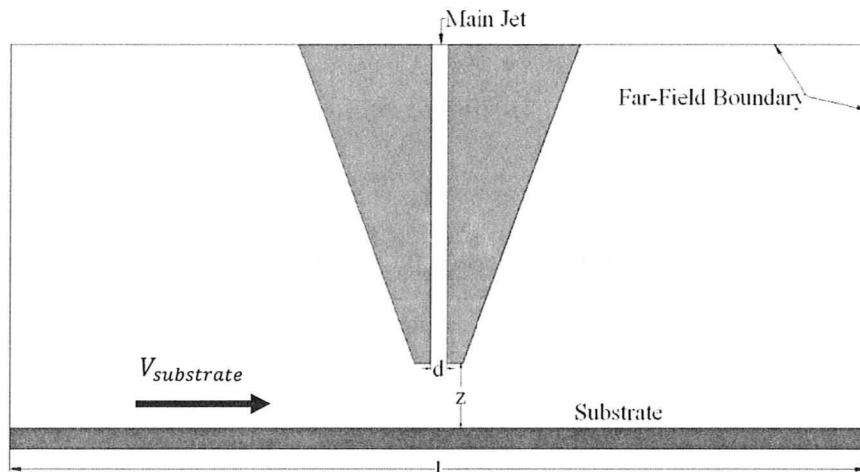


Figure 4-1: Schematic for a single-impinging slot jet.

Figure 4-2 represents a comparison of the non-dimensional velocity at the exit of the slot jet with the experimental data of Maurel and Solliec [2001] with  $Re_m = 27000$  and the numerical results with  $Re_m = 11000$ . The  $k - \varepsilon$  turbulence model was used to capture the turbulence properties in the flow field. The simulations were run with (5%) turbulence intensity, which is defined as the ratio of the root-mean-square of turbulent

velocity fluctuations to the mean flow velocity at the inlet of the nozzles. The turbulence length scale, 7% of the hydraulic diameter, was set to  $2.13 \times 10^{-4}$  for the main slot jet. The plate was modeled as static because the relative velocity of the sheet substrate is much less than the velocities of the air flow from the slot jet both within the gap and near the wall. No-slip conditions were exerted on every wall. The pressure far-field boundaries were set to atmospheric pressure. The flowfield was solved with FLUENT (Ansys) commercial code.

The wall pressure and wall shear stress distributions and the resulting coating weights for plate-to-nozzle ratios ( $z/d$ ) ranging between 2 and 12 and for Reynolds numbers ranging between 11000 and 16000 for  $z/d = 4$  were investigated numerically.

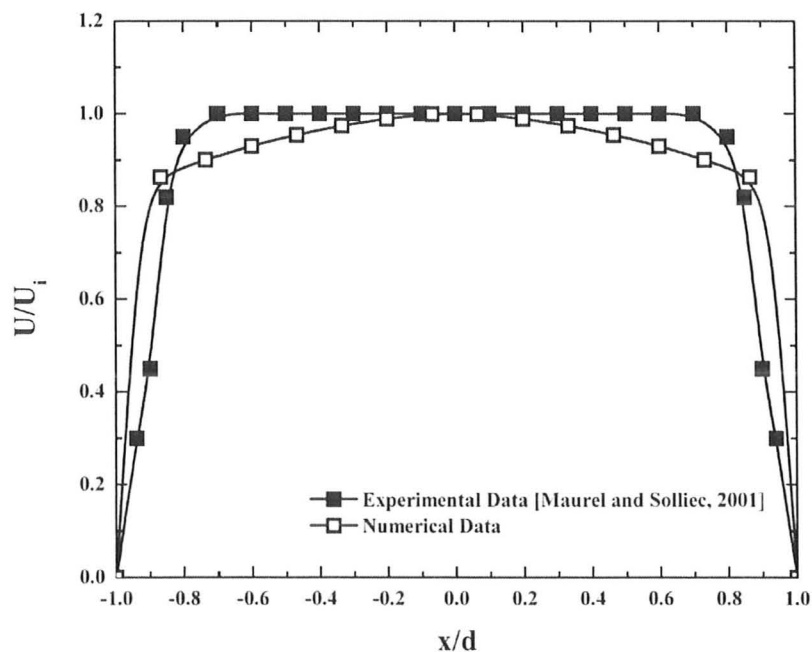


Figure 4-2: Non-dimensional mean velocity profile at the nozzle exit.

#### 4.1.2 Plate-to-Nozzle Ratio Effect

In this section, the effect of plate-to-nozzle ratios ( $z/d$ ) on the wall pressure and shear stress distributions were examined numerically. The main slot jet Reynolds number was fixed at 11000 which corresponds to an air velocity of approximately 105 m/s. The  $z/d$  value was varied between 2 and 12. Figure 4-3 illustrates the non-dimensional pressure distributions on the substrate surface for different  $z/d$  ratios. The horizontal axis is non-dimensionalized by the nozzle gap ( $d$ ) and the vertical axis is non-dimensionalized by twice the dynamic pressure of the main slot jet velocity ( $\rho u_i^2$ ). The non-dimensional wall pressure profiles were not sensitive to  $z/d$  for  $z/d \leq 8$ , which is within the potential core of the main slot jet. By going outside the potential core (i.e.  $z/d = 10$  and 12) of the main jet, the maximum impingement pressure decreased significantly. Figure 4-4 demonstrates the non-dimensional wall shear stress distributions for different  $z/d$  for a single-impinging slot jet. The non-dimensional wall shear stress changes linearly from zero to its maximum value in the impingement region and is not sensitive to  $z/d$  ratios [Ellen and Tu, 1984]. Phares *et al.* [2000] predicted that the maximum shear stress on the substrate is in the laminar boundary layer which is close to the strong favorable pressure gradient on the impingement region. In the wall jet region, occurring at  $x/d$  values greater than the maximum shear stress on the sheet substrate [Ellen and Tu, 1984], the wall shear stress decreased with increasing  $z/d$  ratio. The wall shear stress in this region plays a minor role in estimating the coating weight but still is an essential parameter in shaping the liquid layer profile on the moving substrate.

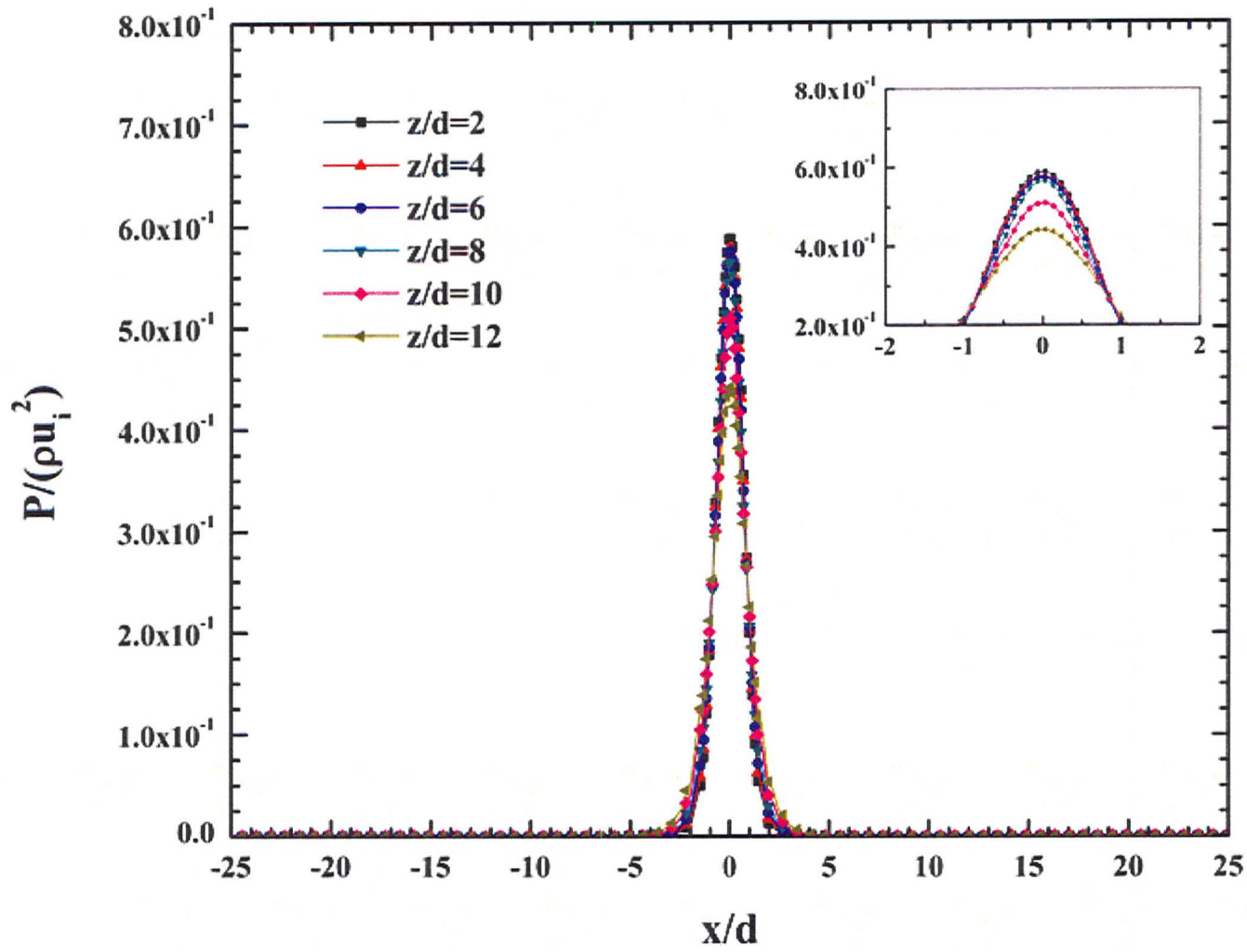


Figure 4-3: Non-dimensional wall pressure distributions for different  $z/d$  ratios with  $Re_m = 11000$ .

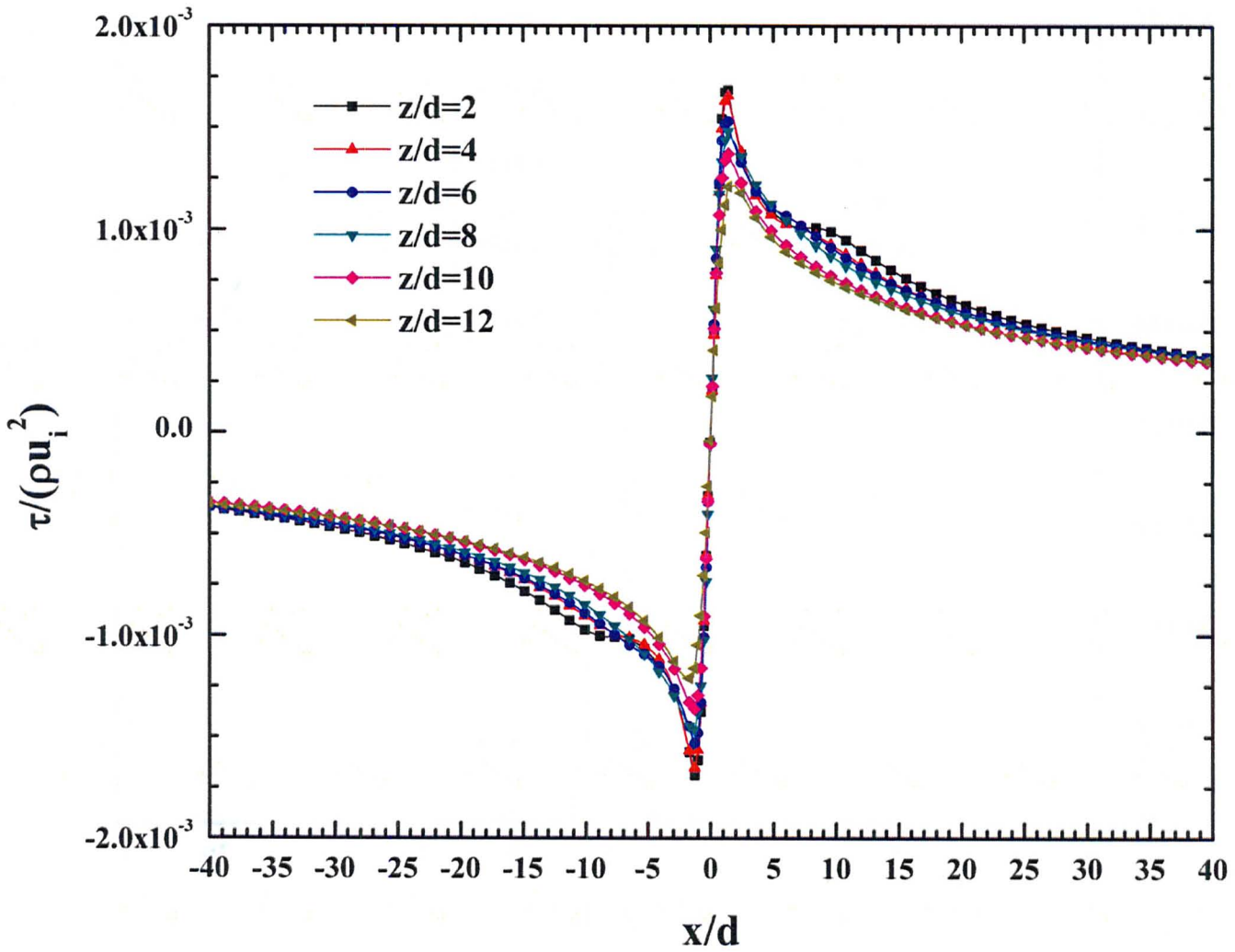


Figure 4-4: Non-dimensional wall shear stress distributions for different  $z/d$  ratios with  $Re_m = 11000$ .

The non-dimensional maximum wall pressure and maximum wall shear stress for different  $z/d$  ratios for a single-impinging slot jet case are presented in Figure 4-5. Figure 4-5(a) shows the non-dimensional maximum pressure on the substrate. The maximum wall pressure is not responsive to  $z/d$  less than 8 which is within the main slot jet potential core and by going outside the potential core the maximum pressure drops considerably. Figure 4-5(b) demonstrates the non-dimensional maximum wall shear stress for different  $z/d$  ratios. The maximum shear stress decreased continuously with increasing  $z/d$  ratio.

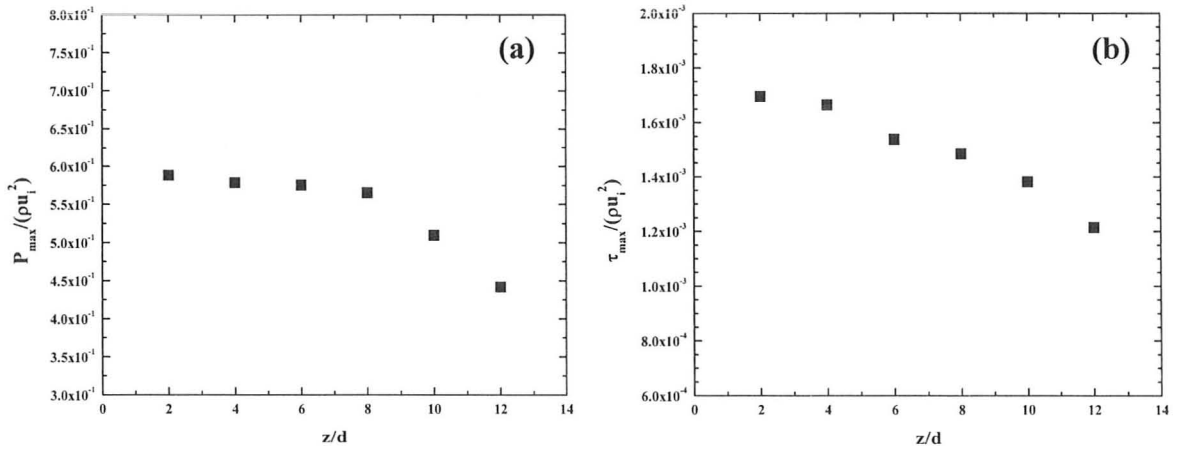


Figure 4-5: Non-dimensional maximum (a) wall pressure; and (b) wall shear stress for different  $z/d$  ratios with  $Re_m = 11000$  for a single-impinging slot jet.

Pressure contour and flow streamlines for  $z/d = 4$  is presented as a sample case in Figure 4-6. The impingement region is beneath the centerline of the main slot jet. The pressure across the boundary of the main slot jet is lower than the pressure magnitude in the far-field domain and this phenomenon causes the flow to entrain in this region which is shown clearly in Figure 4-6.

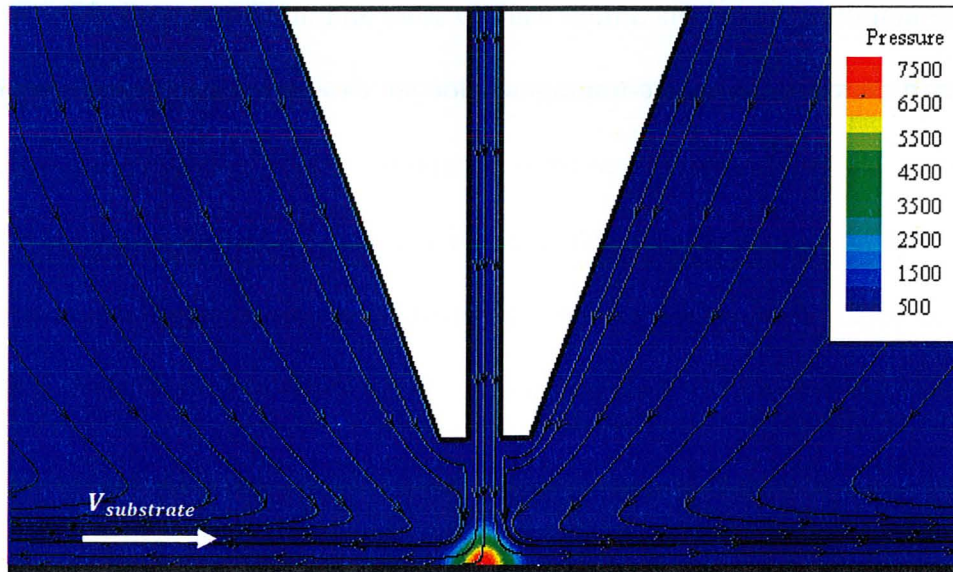


Figure 4-6: Pressure contour and streamlines for  $z/d = 4$  and  $Re_m = 11000$ .

As was depicted in the introduction of this chapter, the wall pressure and shear stress results were used as boundary conditions in an analytical formula, proposed in chapter 2, to estimate the coating weight on the moving substrate. Figure 4-7 illustrates the coating weight for different  $z/d$  ratios for  $V_{strip} = 0.50 \text{ m/s}$ . The coating weight does not vary significantly for  $z/d$  ratios less than 8 because as discussed previously, the main jet is in its potential core whereas by going outside the potential core (i.e. to  $z/d = 10$  and  $z/d = 12$ ) the coating weight increased considerably. Figure 4-8 shows the variation of the coating weight for different strip velocities ranging between  $0.50 \text{ m/s}$  and  $2.50 \text{ m/s}$  for different  $z/d$  ratios with  $Re_m = 11000$ . By increasing the strip velocity the coating weight increased continuously. Figure 4-8 also shows that the coating weight increases with  $z/d$  for any given strip velocity. The results in Figure 4-8 are used later as

a base case for comparison with the coating weight results of different version of multiple-impinging slot jet configurations.

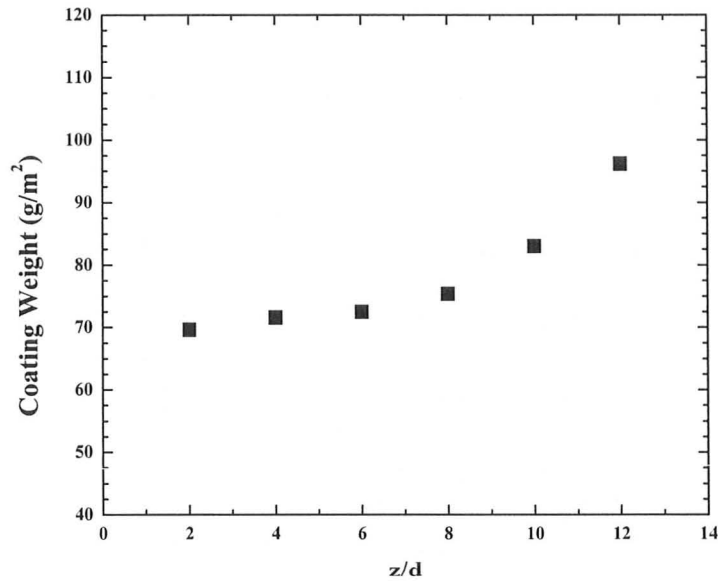


Figure 4-7: Coating weight for different  $z/d$  ratios, with  $V_{Strip} = 0.50 \text{ m/s}$  and  $Re_m = 11000$ .

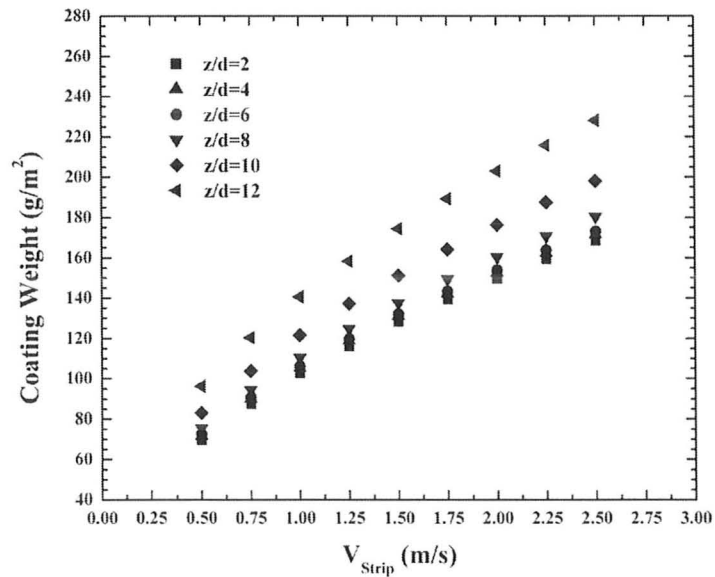


Figure 4-8: Coating weight for different  $V_{Strip}$  and  $z/d$  ratios with  $Re_m = 11000$ .

### 4.1.3 Main Slot Jet Reynolds Numbers Effect

In this section, the effect of the main jet Reynolds numbers on the wall pressure and shear stress distributions and consequently the coating weight is examined numerically when fixing  $z/d = 4$ . The Reynolds number at the exit of the jet changed by varying the plenum pressure and is rigorously related to the design of the jet exit. The range of Reynolds numbers explored was between 11000 and 16000. Figure 4-9 demonstrates the non-dimensional pressure distributions for different Reynolds numbers for  $z/d = 4$ , which is in the potential core of the main slot jet. The dynamic pressure was calculated for each  $Re_m$  separately based on the jet exit velocity. The pressure normalization removes the effect of  $Re_m$  on the wall pressure [Tu and Wood, 1996]. According to this Figure, the non-dimensional maximum pressure on the flat substrate is invariable for different  $Re_m$ . It is worth noting that at higher  $z/d$ , the effect of  $Re_m$  on the wall pressure is the same as the results shown in Figure 4-9 [Ellen and Tu, 1984]. Figure 4-10 demonstrates the non-dimensional wall shear stress distributions for different  $Re_m$  with  $z/d = 4$ . The wall shear stress is non-dimensionalized by twice the dynamic pressure which varies for each  $Re_m$ . The normalization method removes the effect of  $Re_m$  in the impingement region [Tu and Wood, 1996], while in the wall jet region, the non-dimensional wall shear stress decreased slightly with increasing  $Re_m$ . The non-dimensional maximum shear stress decreased slightly by increasing  $Re_m$ . As before, the wall pressure and shear stress distributions were used in an analytical equation as boundary conditions, respectively, to approximate the coating weight on the moving sheet substrate for different substrate velocities and different  $Re_m$ .

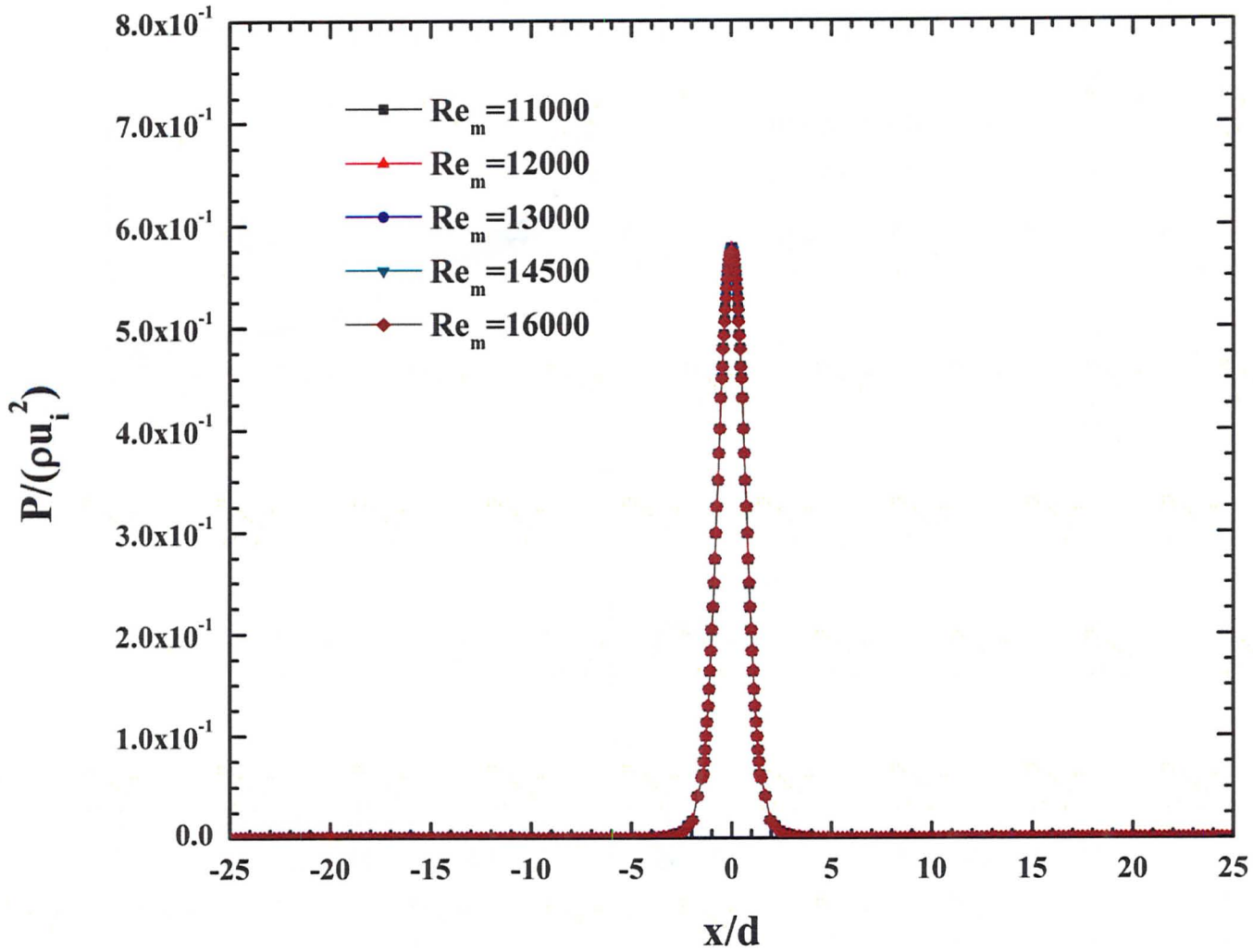


Figure 4-9: Non-dimensional wall pressure distributions for different  $Re_m$  with  $z/d = 4$ .

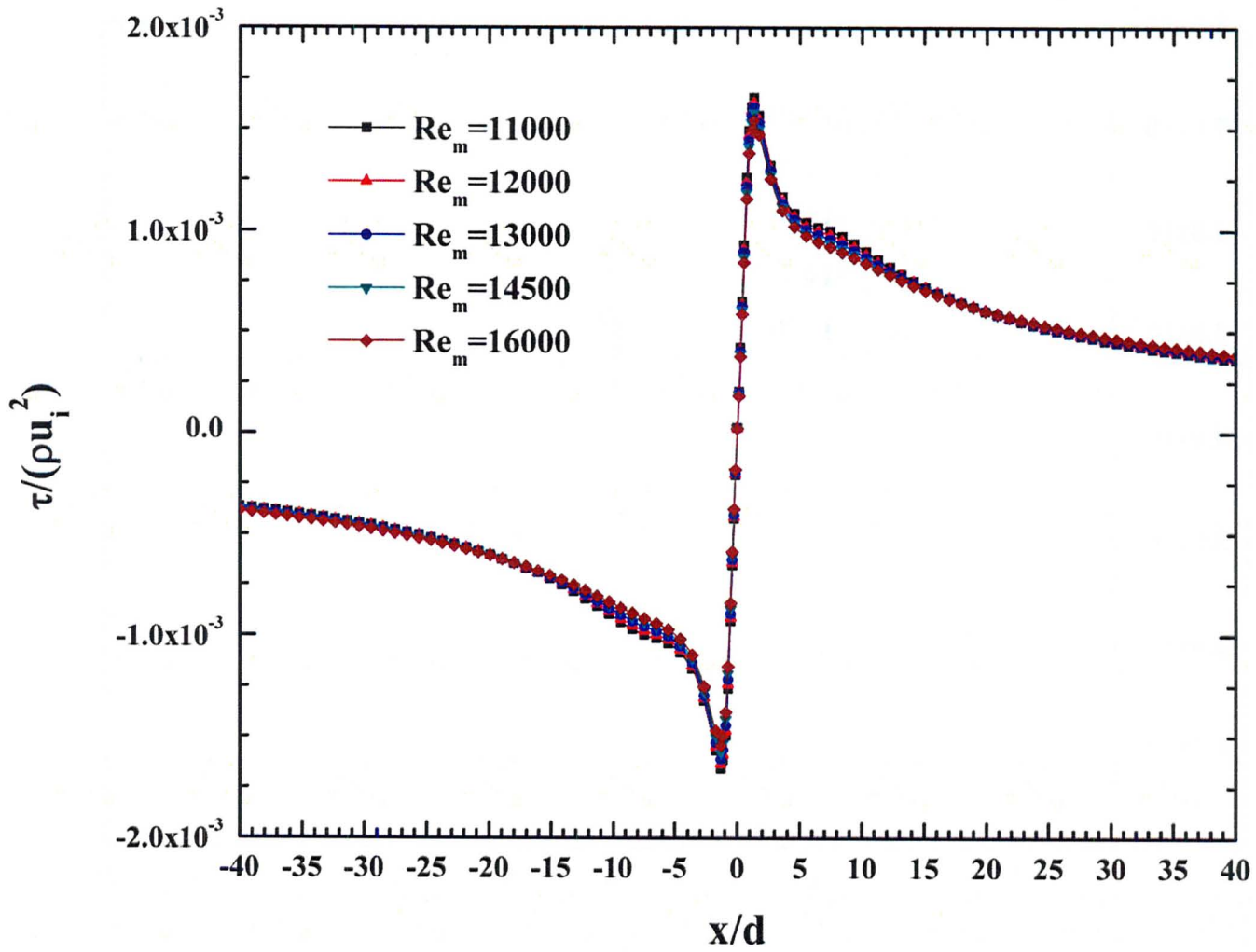


Figure 4-10: Non-dimensional wall shear stress distributions for different  $Re_m$  with  $z/d = 4$ .

Figure 4-11 shows the coating weight for different  $Re_m$  with  $z/d = 4$  and  $V_{strip} = 0.50 \text{ m/s}$  for a single-impinging slot jet. By increasing  $Re_m$  from 11000 to 16000 the coating weight decreased continuously from  $70 \text{ g/m}^2$  to  $45 \text{ g/m}^2$  which is quite significant. The consequence of  $Re_m$  for different strip velocities on the coating weight is examined in Figure 4-12. According to this Figure, by increasing the strip velocity the coating weight increased significantly. The rate of coating weight increment decreased significantly by increasing strip velocity for each  $Re_m$ . The coating weight trend is similar for higher  $z/d$  ratio [Naphade *et al.*, 2005]. In the next section, a modified geometry of multiple-impinging slot jets with two parallel impinging slot jets discharging air perpendicularly on the flat substrate with a wall between the jets is investigated.

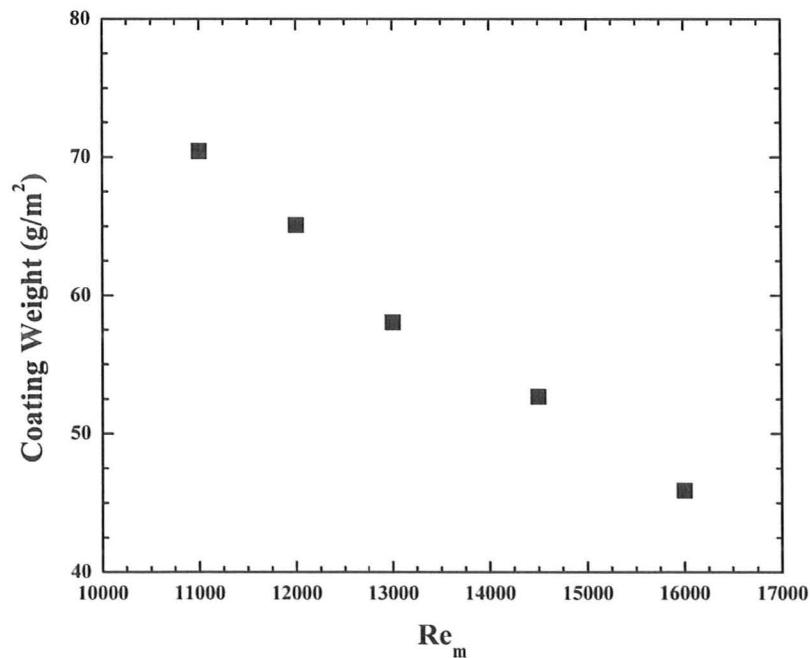


Figure 4-11: Coating weight variation with  $Re_m$ , with  $V_{strip} = 0.50 \text{ m/s}$  and  $z/d = 4$ .

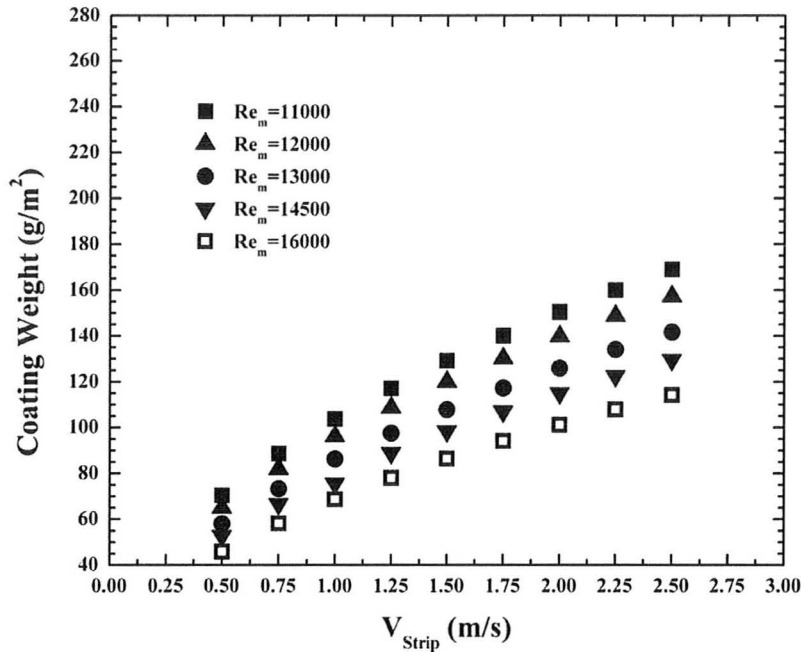


Figure 4-12: Coating weight for varying  $Re_m$  and  $V_{Strip}$  with  $z/d = 4$ .

## 4.2 Two Parallel Impinging Slot Jets

In this section, a modified geometry of multiple-impinging slot jets with two parallel impinging jets is investigated numerically. The concept of this configuration is thoroughly presented in Tu [1994]. Because of its length, the strip tends to vibrate which may cause inconsistent  $z/d$  ratio over time. This vibration can cause the coating weight to be inconsistent along the strip length. The concept of this multi-slot air knife configuration is to generate a static pressure region between the two jets which is defined as a pressurized region to stabilize the substrate from vibration. The wall pressure and shear stress distributions for different plate-to-nozzle ratios, main jet Reynolds numbers and wall thickness-to-nozzle ratios were studied in order to estimate the coating weight on the moving strip.

#### 4.2.1 Geometry, Boundary and Initial Conditions

The configuration which is investigated in this section consists of two parallel impinging slot jets with a wall between them. Figure 4-13 shows this configuration in more detail. The only difference between the boundary and initial conditions for this configuration and the conventional single-impinging slot jet is the wall distance between the two jets, which is represented by  $a$ . The effect of  $z/d$  ratios on the wall pressure and shear stress distributions and therefore on the coating weight is investigated for  $a/d = 12$ . In the next step, the effect of the main slot jet Reynolds numbers on the coating weight with  $z/d=4$  is examined. The range of  $Re_m$  was varied between 11000 and 16000. The effect of wall thickness-to-nozzle ratio ( $a/d$ ) on the coating weight with  $Re_m = 11000$  and  $z/d=4$  is examined to find trends for this configuration. The coating weight for this configuration is then compared to the results of conventional model of a single-impinging slot jet for different  $z/d$  ratios and  $Re_m$ .

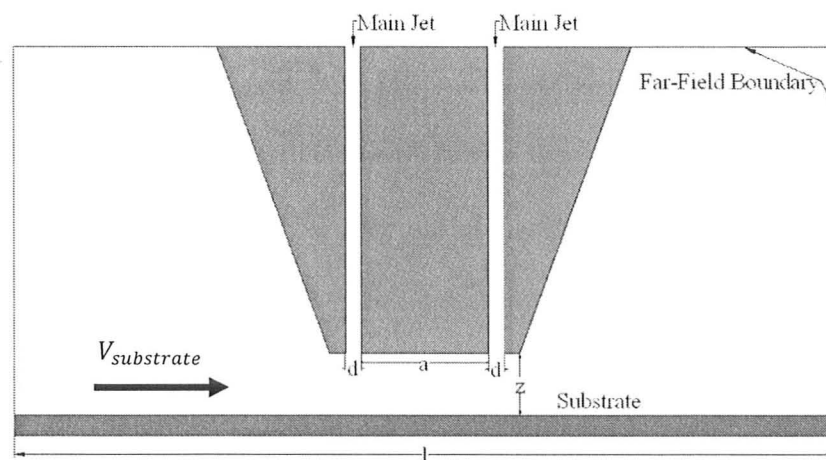


Figure 4-13: Schematic for two parallel impinging slot jets.

#### 4.2.2 Plate-to-Nozzle Ratio Effect

In this section, the wall pressure and wall shear stress distributions for  $z/d$  ratios ranging between 2 and 12 were investigated numerically for  $Re_m = 11000$ . For the coating weight estimation, it was assumed that the first impinging slot jet wipes the excess zinc from the moving substrate [Tu, 1994] and the second impinging slot jet had an insignificant effect on the wiping process but had considerable effect on generating static pressure between the two jet region for stabilizing the substrate. Figure 4-14 represents the non-dimensional wall pressure distributions for different  $z/d$  ratios with  $Re_m = 11000$  and  $a/d = 12$ . The location of the maximum impingement pressure moved away from the main slot jet centerline with increasing  $z/d$  ratio between  $-10 < x/d < -7$  (left impinging jet). It can be seen that in the pressurized region, defined as the region between the two parallel impinging slot jets, the stagnation pressure increased slightly for  $z/d$  ratio greater than 6 and dropped significantly due to the creation of a vortex in this region, which is shown in Figure 4-17. Figure 4-15 shows the non-dimensional wall shear stress distributions for different  $z/d$  ratios with  $Re_m = 11000$  and  $a/d = 12$ . The position of the maximum wall shear stress deviates slightly from the centerline of the main slot jet for increasing  $z/d$  ratios. In the wall jet region, the non-dimensional wall shear stress distribution decreased for increasing  $z/d$  ratios, while in the pressurized region the maximum value of the wall shear stress increased for increasing  $z/d$  ratios. In the pressurized region, the two opposing wall jets interact with each other near the center of the wall which creates fountain upwash flow in that region.

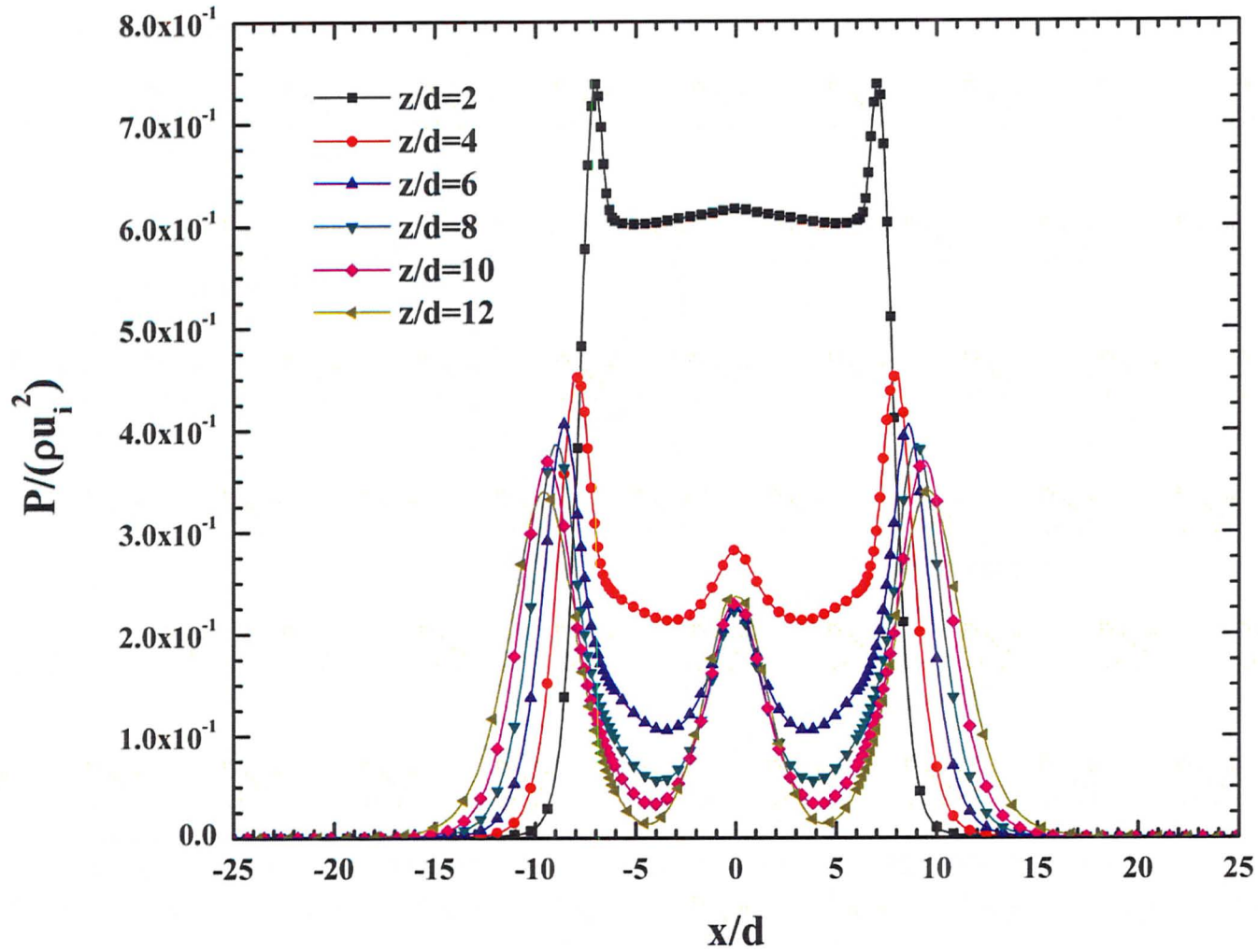


Figure 4-14: Non-dimensional wall pressure distributions for different  $z/d$  ratios with  $Re_m = 11000$  and  $a/d = 12$ .

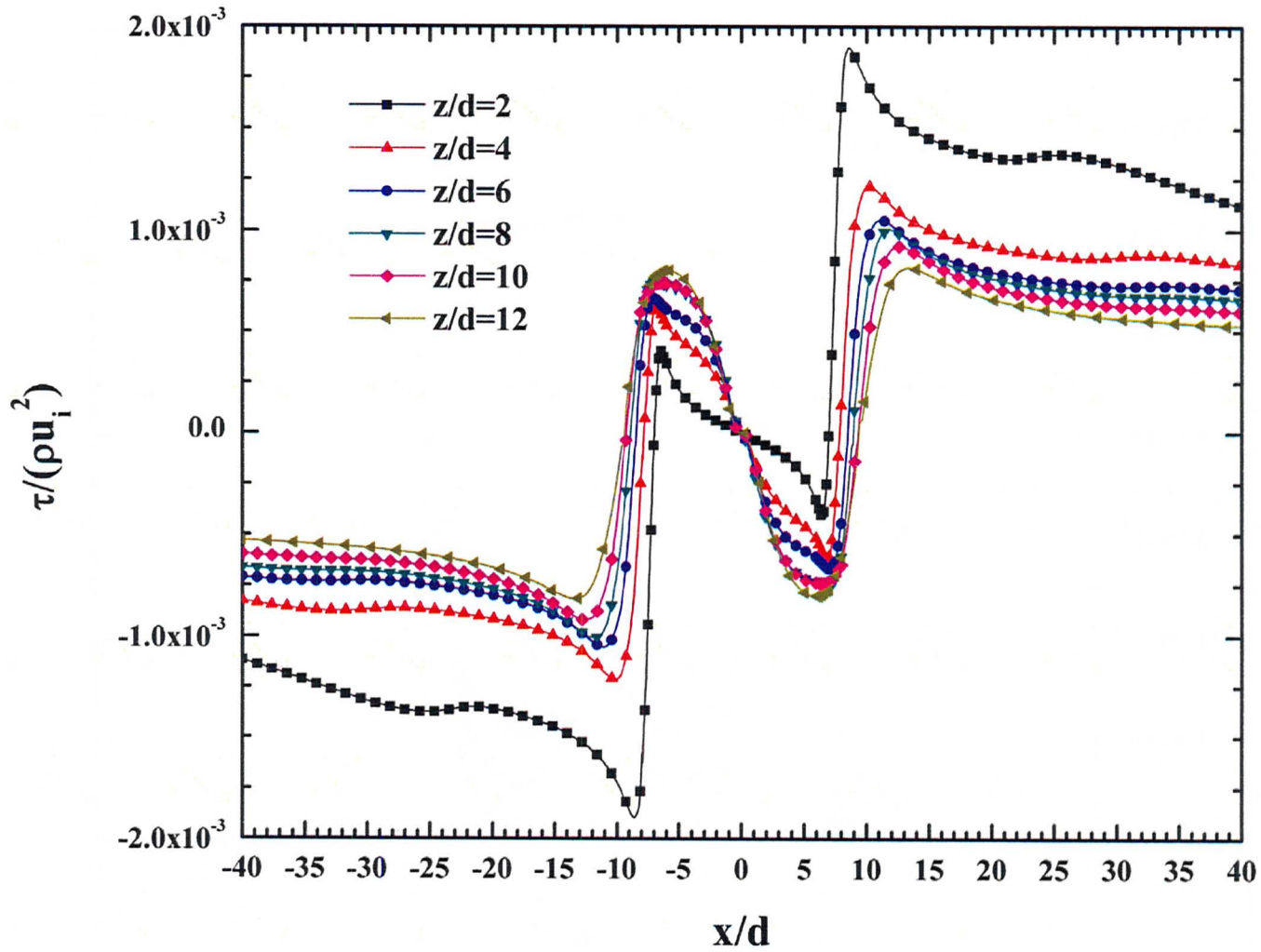


Figure 4-15: Non-dimensional wall shear stress distributions for different  $z/d$  ratios with  $Re_m = 11000$  and  $a/d = 12$ .

The maximum value of the non-dimensional wall pressure and shear stress for this configuration are compared with the results of the conventional single-impinging slot jet. According to Figure 4-16(a), the maximum value of the non-dimensional pressure for this configuration is less than the magnitude of the conventional model for all  $z/d$  ratios greater than  $z/d = 2$ . For this configuration, the maximum value of pressure decreased continuously with increasing  $z/d$  ratio. Figure 4-16(b) shows a comparison of the non-dimensional maximum shear stress for both the single-impinging slot jet and two parallel impinging slot jets. The value of the non-dimensional maximum shear stress for both cases decreased for increasing  $z/d$  ratios. The magnitude of this property for the multiple-impinging slot jets is less than the results for the conventional model for each  $z/d$  ratio except for  $z/d = 2$ , which is higher in value for both maximum wall pressure and shear stress.

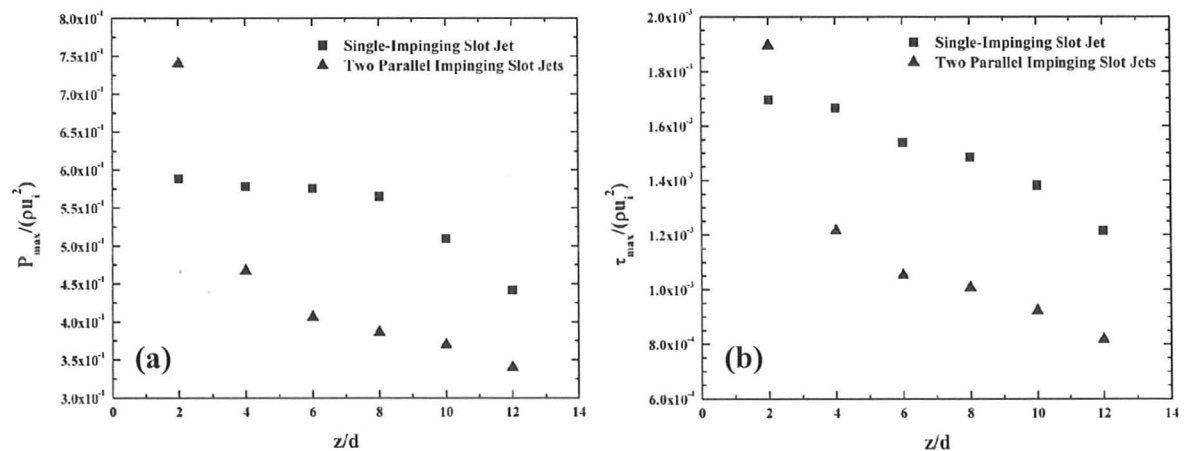


Figure 4-16: Comparison of non-dimensional maximum (a) wall pressure; and (b) shear stresses for different  $z/d$  ratios for both configuration of a single-impinging slot jet and two parallel impinging slot jets.

The pressure contour and streamlines with  $z/d = 4$ ,  $Re_m = 11000$  and  $a/d = 12$  for this configuration is shown in Figure 4-17. The impingement point deviates from the centerline of the main jet, and as was shown in Figure 4-14, by increasing the  $z/d$  ratio the impingement point moves further away from the centerline of each impinging slot jet. Fernández *et al.* [2007] studied the flow field of twin impinging slot jets using the standard and realizable  $k - \varepsilon$  and the standard  $k - \omega$  turbulence model. They compared their results with experimental data and made the conclusion that none of the above turbulence models can predict the flow in the impingement region accurately, but these inaccuracies were tolerable for engineering practice. The counter rotating vortices between the impinging jets caused the pressure drop on the sheet substrate and by increasing the  $z/d$  ratio the pressure fell more in this region.

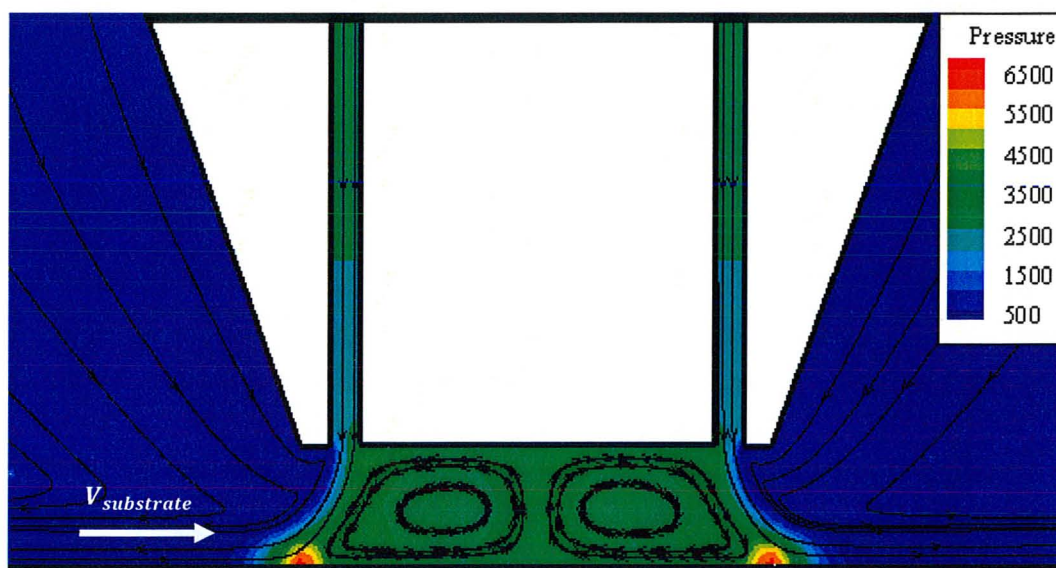


Figure 4-17: Pressure contour and streamlines with  $z/d = 4$ ,  $Re_m = 11000$  and  $a/d = 12$ .

As Saripalli [1983] studied twin impinging round jets experimentally using visualization techniques, he declared that the important characteristics of this configuration are the fountain upwash flow created by colliding the opposite wall jets and also the entrainment of flow between the jets region which can be seen also in Figure 4-17. The wall pressure results and wall shear stress distributions reported in Figure 4-14 and Figure 4-15 were used as boundary conditions for the analytical formula to approximate the coating weight on a moving substrate for different  $z/d$  ratios. The coating weights for both configurations of a single-impinging slot jet and two parallel impinging slot jets for  $z/d$  ratios ranging between 2 and 12, with  $Re_m = 11000$  and  $V_{Strip} = 0.50 \text{ m/s}$  are shown in Figure 4-18. According to this Figure, the coating weight for  $z/d = 2$  is approximately the same for both configurations, while for higher  $z/d$  ratios the coating weight for two parallel impinging slot jets is higher. The coating weight for this configuration is highly responsive and increases for the entire range of  $z/d$  ratios. The effect of strip velocity on the coating weight for different  $z/d$  ratios with  $V_{Strip} = 0.50 \text{ m/s}$  and  $Re_m = 11000$  is shown in Figure 4-19. The substrate velocity ranged from  $0.50 \text{ m/s}$  and  $2.50 \text{ m/s}$ . By increasing strip velocity the coating weight increased significantly because when the strip velocity increased the time needed to wipe down excess zinc from the moving substrate decreased. The modified version of multiple-impinging slot jets, which is presented in this section has the advantage of preventing variation in coating weight thickness due to substrate vibration but has the disadvantage of unwanted surface roughness in the finished coating [Tu, 1994].

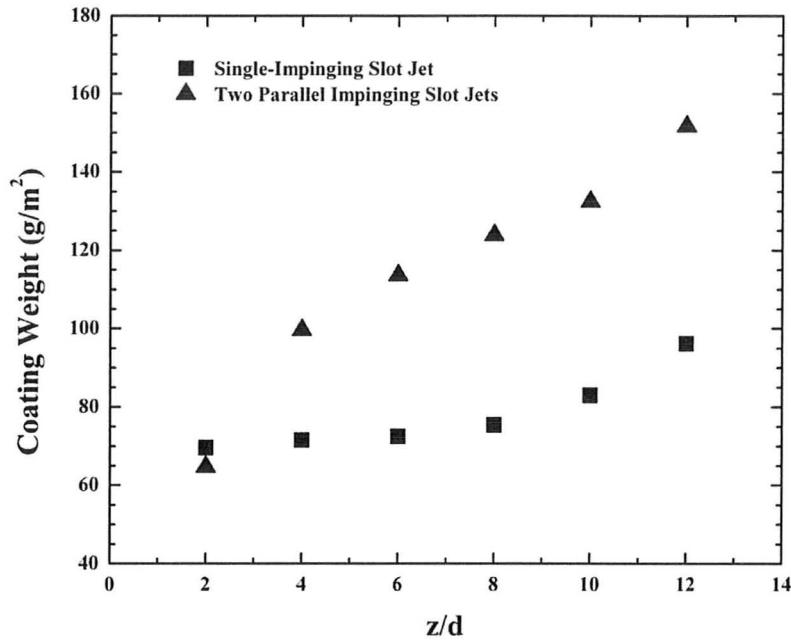


Figure 4-18: Comparison of coating weight for a single-impinging slot jet and two parallel impinging slot jets for different  $z/d$  ratios, with  $V_{Strip} = 0.50$  m/s and  $Re_m = 11000$ .

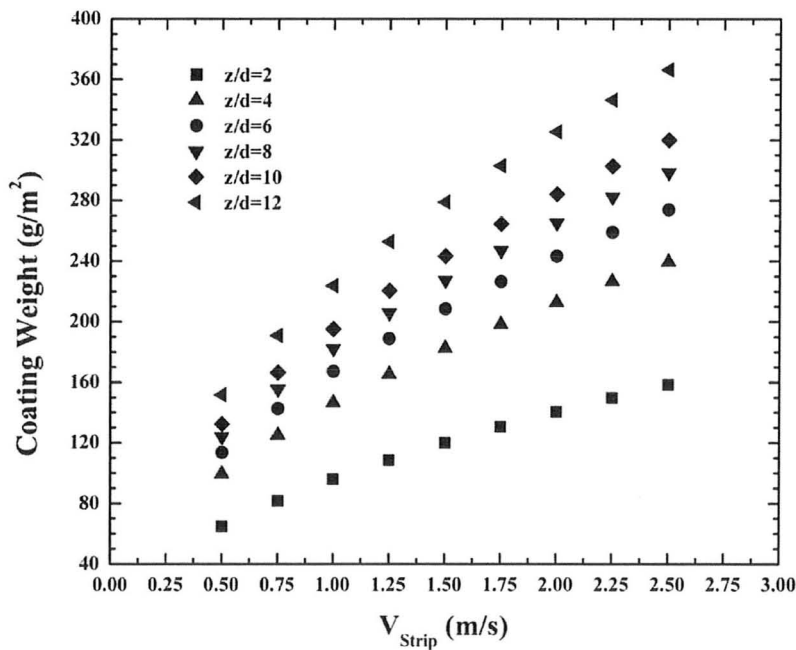


Figure 4-19: Coating weight for different  $V_{Strip}$  and  $z/d$  ratios with  $Re_m = 11000$ .

### 4.2.3 Main Slot Jet Reynolds Numbers Effect

The effect of main slot jet Reynolds numbers ( $Re_m$ ) on the coating weight was investigated numerically for a configuration with two parallel impinging slot jets. The range of  $Re_m$  was between 11000 and 16000 for  $z/d = 4$ . Figure 4-20 demonstrates a comparison between the non-dimensional maximum wall pressure for different  $Re_m$  for  $z/d = 4$  for both configurations of a single-impinging slot jet and two parallel impinging slot jets. The non-dimensional maximum wall pressure was not responsive to  $Re_m$  for both configurations but the magnitude of the maximum pressure increased on the substrate by the square root of jet velocity. It is shown that the magnitude of maximum pressure for a single-impinging slot jet is higher than two parallel impinging slot jets for all  $Re_m$ .

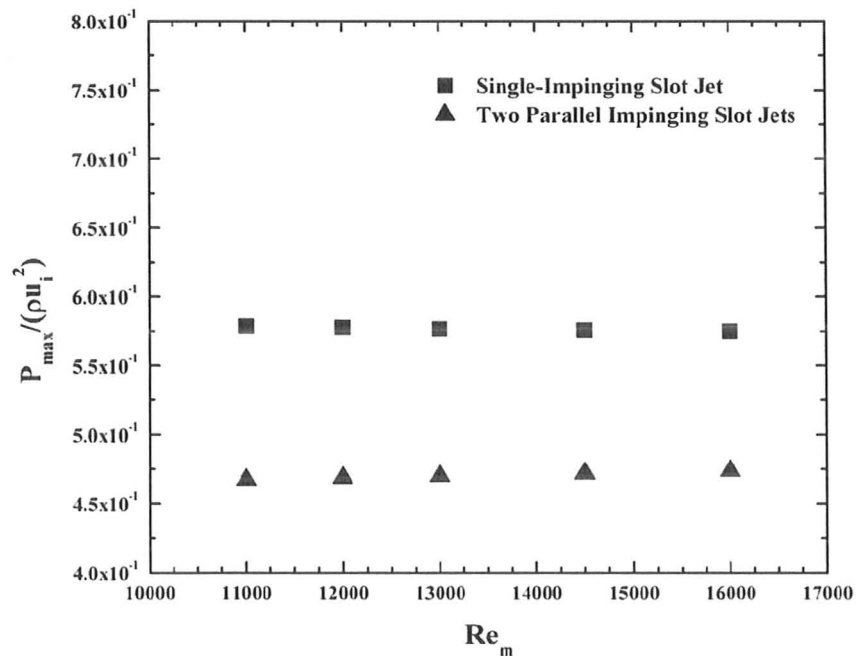


Figure 4-20: Comparison of non-dimensional maximum wall pressure for different  $Re_m$  for  $z/d = 4$ .

The effect of  $Re_m$  on the substrate non-dimensional maximum shear stress sheet for both configurations of a single-impinging slot jet and two parallel impinging slot jets is shown in Figure 4-21. It is shown that for both configurations that the non-dimensional maximum wall shear stress decreased with increasing  $Re_m$ .

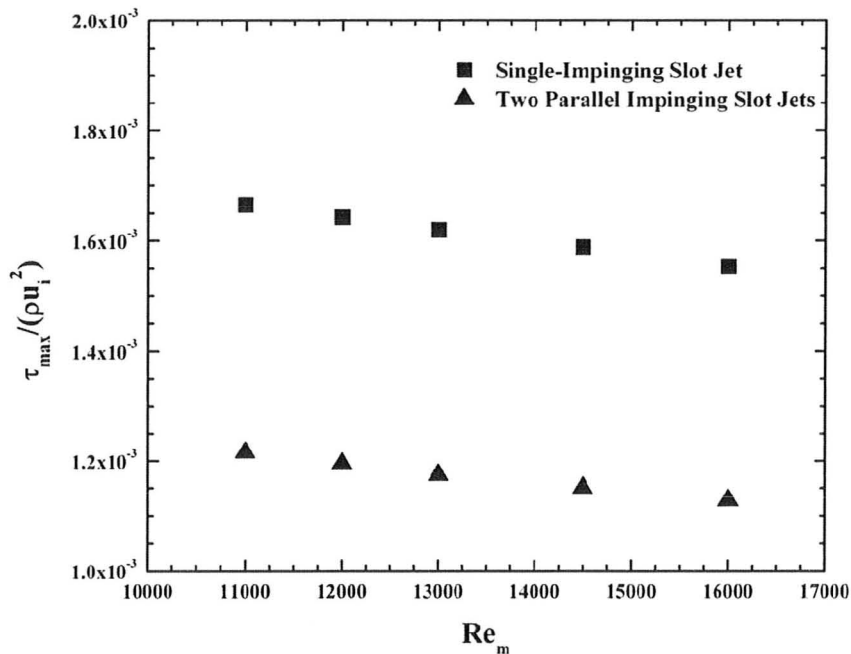


Figure 4-21: Comparison of non-dimensional maximum wall shear stress for different  $Re_m$  for  $z/d = 4$  for a single-impinging slot jet and two parallel impinging slot jets.

The wall pressure and shear stress distributions were used to calculate the coating weight for different  $Re_m$  and  $V_{Strip}$ . Figure 4-22 represents the coating weight for two parallel impinging slot jets for  $z/d = 4$  for different  $Re_m$  and  $V_{Strip}$ . By comparing these results with Figure 4-12, it can be seen that the coating weight for a single-impinging slot jet is less than the modified version of multiple-impinging slot jets for all  $Re_m$ .

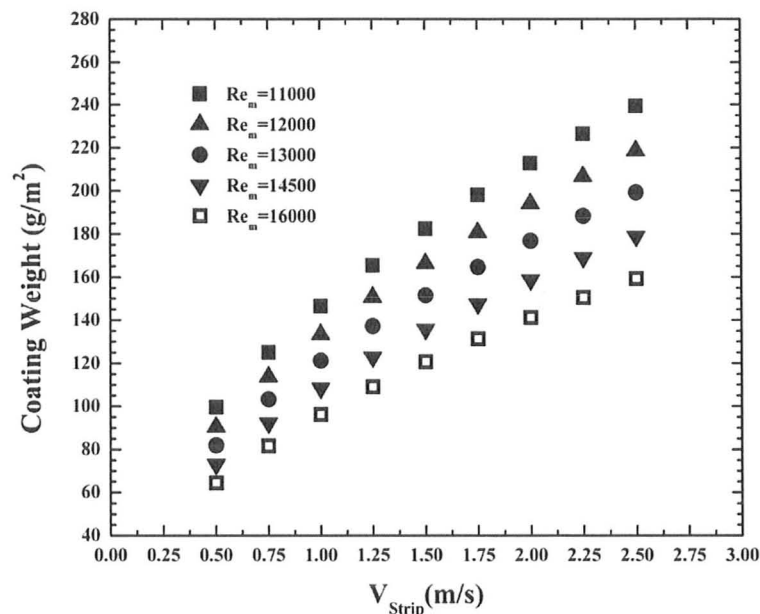


Figure 4-22: Coating weight for different  $Re_m$  and  $V_{Strip}$  with  $z/d = 4$ .

#### 4.2.4 Wall Thickness-to-Nozzle Ratio Effect

In this section, the effect of wall thickness-to-nozzle ratio ( $a/d$ ) on the coating weight is investigated numerically for  $z/d = 4$ . The wall pressure results and shear stress distributions will not be presented in this section on the ground that by changing  $a/d$  ratio the overall shape of the wall pressure and shear stress distributions do not change significantly except for the maximum pressure gradient which affects on the coating weight. The effect of  $a/d$  ratio ranging between 4 and 15 on coating weight was investigated numerically for  $z/d = 4$  and  $Re_m = 11000$ . Figure 4-23 demonstrates the effect of  $a/d$  ratio on the coating weight for two parallel impinging slot jets configuration for different substrate velocities. By increasing the  $a/d$  ratio and/or decreasing the substrate velocity the coating weight decreased significantly. The coating weight results which are estimated for this configuration should be verified with experimental

measurements. In the next section, different multiple-impinging slot jet geometry will be developed numerically.

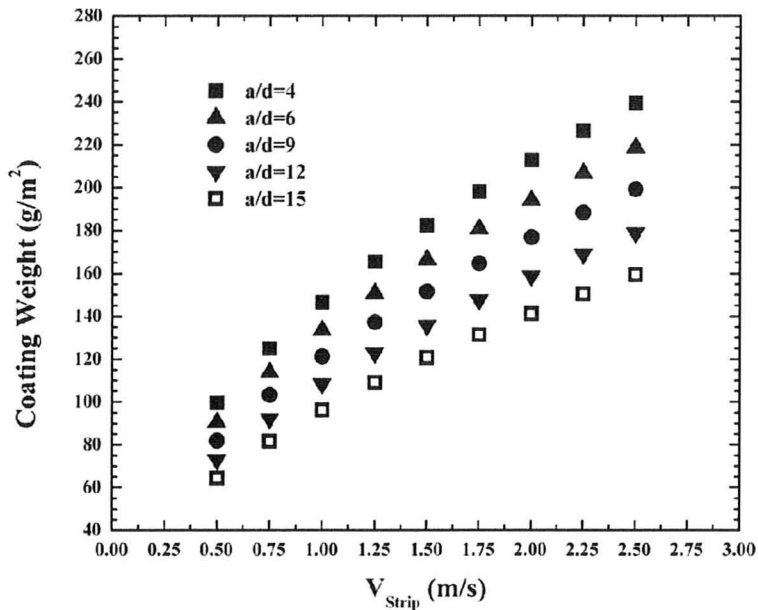


Figure 4-23: Coating weight for different  $a/d$  and  $V_{strip}$  with  $z/d = 4$  and  $Re_m = 11000$ .

### 4.3 Main Jet with Inclined Auxiliary Impinging Slot Jet

In this section, a modified version of the multiple-impinging slot jets is studied numerically. The configuration consists of one main impinging slot jet discharging air perpendicularly on the substrate and one inclined auxiliary impinging slot jet discharging air with lower velocity in comparison with the main slot jet [Tu, 1993]. The wall pressure and shear stress distributions and as a result the coating weight on the moving substrate for different plate-to-nozzle ratios, main jet Reynolds numbers, auxiliary jet Reynolds numbers and wall thickness-to-nozzle ratios are studied in this section. The geometry,

boundary and initial conditions for this modified configuration are studied in the next subsection.

#### 4.3.1 Geometry, Boundary and Initial Conditions

Figure 4-24 shows the geometry of a modified multiple-impinging slot jets. The main slot jet discharges air perpendicularly on the substrate, while the auxiliary slot jet discharges air at a lower velocity versus the main slot jet at a 20 degree angle from the main slot jet centerline. The auxiliary slot jet width is two times of the main slot jet gap which results in a lower velocity in comparison with the main slot jet. The turbulent length scale, 7% of the hydraulic diameter, was set to  $2.13 \times 10^{-4}$  for the main slot jet and  $4.26 \times 10^{-4}$  for the auxiliary slot jet, correspondingly.

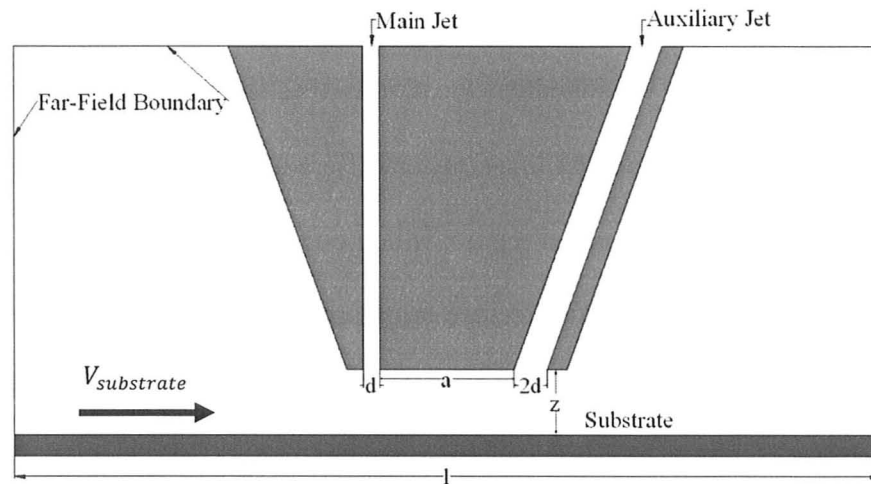


Figure 4-24: Schematic for a main with an inclined auxiliary impinging slot jets.

The effect of plate-to-nozzle ratios ( $z/d$ ) changing between 2 and 12, main slot jet Reynolds numbers ( $Re_m$ ) changing between 11000 and 16000, auxiliary slot jet Reynolds numbers ( $Re_a$ ) which is changed between 4000 and 13000 and wall thickness-

to-nozzle ratios ( $a/d$ ) changing between 4 and 15 on the coating weight were investigated numerically on the moving substrate. The substrate was considered fixed because the ratio of the jet velocity to substrate velocity is high. The pressure at the far-field boundary condition was set to atmospheric pressure.

#### 4.3.2 Plate-to-Nozzle Ratio Effect

The effect of  $z/d$  ratio on the wall pressure and shear stress distributions were investigated numerically for the above configuration with the purpose of estimating the coating weight on the moving substrate. Figure 4-25 shows the non-dimensional wall pressure distributions for different  $z/d$  ratios with  $Re_m = Re_a = 11000$ . It is shown that the wall pressure is not symmetric unlike the previous configurations. The impingement location on the substrate deviates from the centerline of the main slot jet and by increasing the  $z/d$  ratio the impingement location moves to the left of the centerline of the main slot jet. The impingement location for different  $z/d$  ratios changes between  $-2.50 < x/d < -0.50$ . The pressurized region, which occurs between the main slot jet and auxiliary slot jet, shows a significant pressure drop on the substrate and also makes the jet flow deviate from the centerline of the main slot jet. This region makes the substrate stable from vibration which prevents variations in the coating weight [Tu, 1994]. The wall pressure in this region decreases with increasing  $z/d$  ratios. It is obvious that the auxiliary impinging slot jet creates a local maxima in the range of  $12 < x/d < 15$ . This maxima moves slightly toward the centerline of the main jet with increasing  $z/d$  ratio.

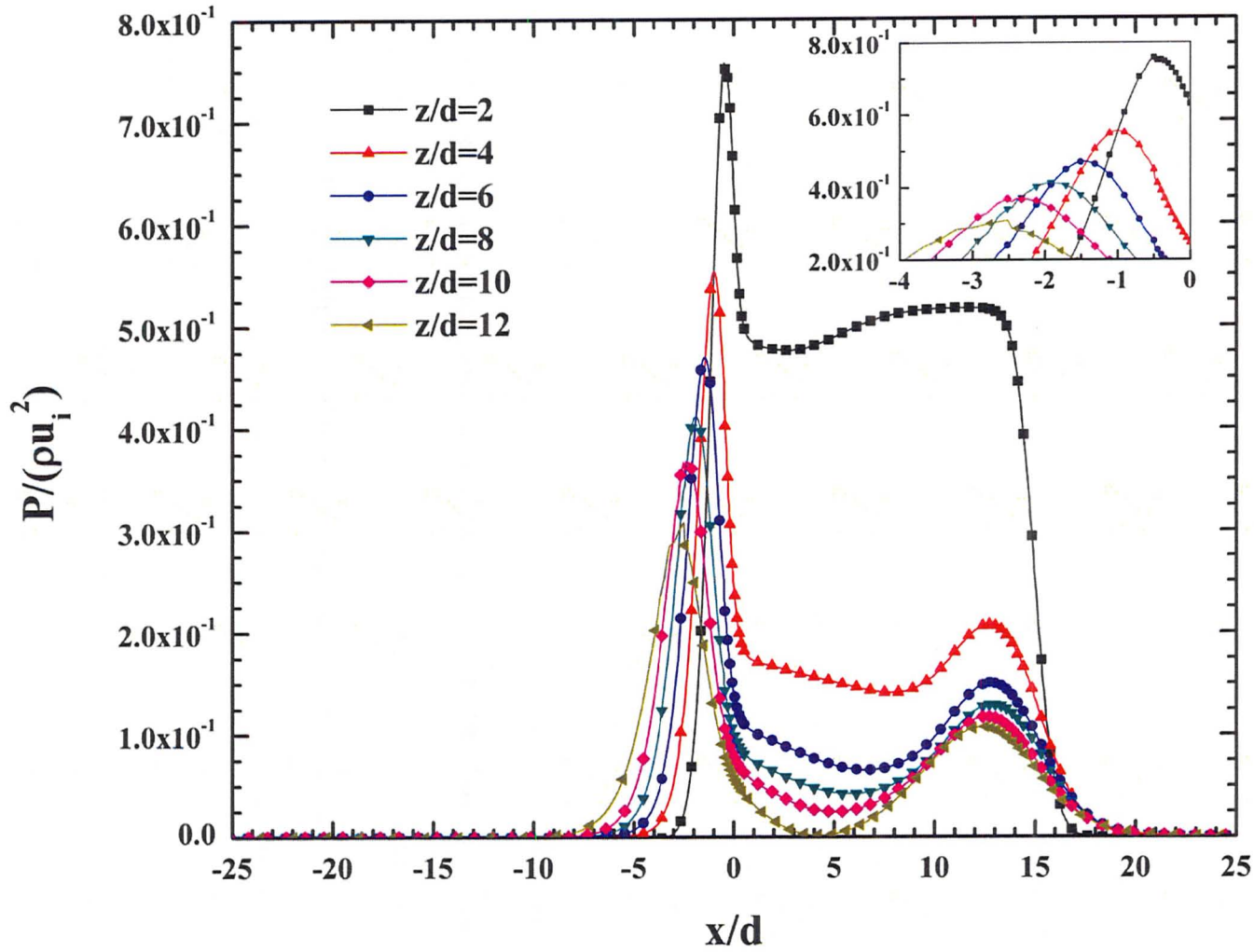


Figure 4-25: Non-dimensional wall pressure distributions for different  $z/d$  ratios with  $Re_m = Re_a = 11000$ .

Figure 4-26 shows the non-dimensional wall shear stress distributions for different  $z/d$  ratios on the substrate with  $Re_m = Re_a = 11000$ . It is shown in the Figure that the non-dimensional maximum shear stress moves away from the centerline of the main slot jet with increasing  $z/d$  ratios.

Figure 4-27 shows the non-dimensional maximum wall pressure and shear stress on the substrate for different  $z/d$  ratios with  $Re_m = Re_a = 11000$ . Figure 4-27(a) compares the non-dimensional maximum wall pressure. The maximum wall pressure is sensitive to  $z/d$  ratio for this configuration and decreased with increasing  $z/d$  ratio. The magnitude of maximum wall pressure for all  $z/d$  ratios for this configuration is less than the magnitude for the conventional model of a single-impinging slot jet except for  $z/d = 2$ . Figure 4-27(b) compares the non-dimensional maximum wall shear stress for different  $z/d$  ratios for both configurations of a single-impinging slot jet and a modified version of multiple-impinging slot jets describing the geometry in the last subsection. It is responsive to  $z/d$  ratios and by increasing  $z/d$  ratio the maximum wall shear decreased significantly for both configurations.

Figure 4-28 shows pressure contour and streamlines with  $z/d = 4$  and  $Re_m = Re_a = 11000$ . The location of the maximum pressure was not under the centerline of the main slot jet which was shown for different  $z/d$  ratios in Figure 4-25. A counter-clockwise vortex is created between the main and auxiliary impinging slot jet which causes pressure drop on the substrate as was shown in Figure 4-25.

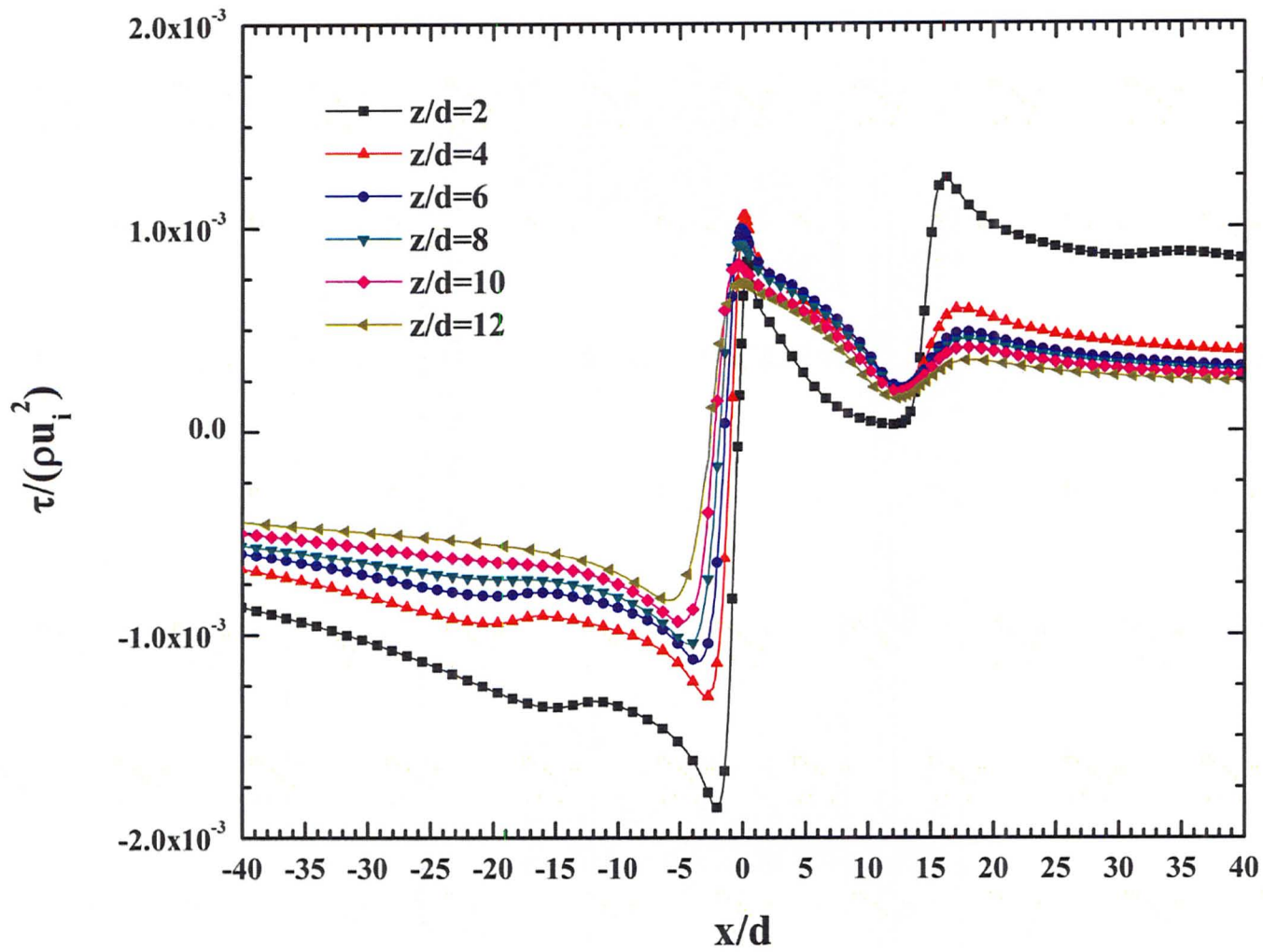


Figure 4-26: Non-dimensional wall shear stress distributions for different  $z/d$  ratios with  $Re_m = Re_a = 11000$ .

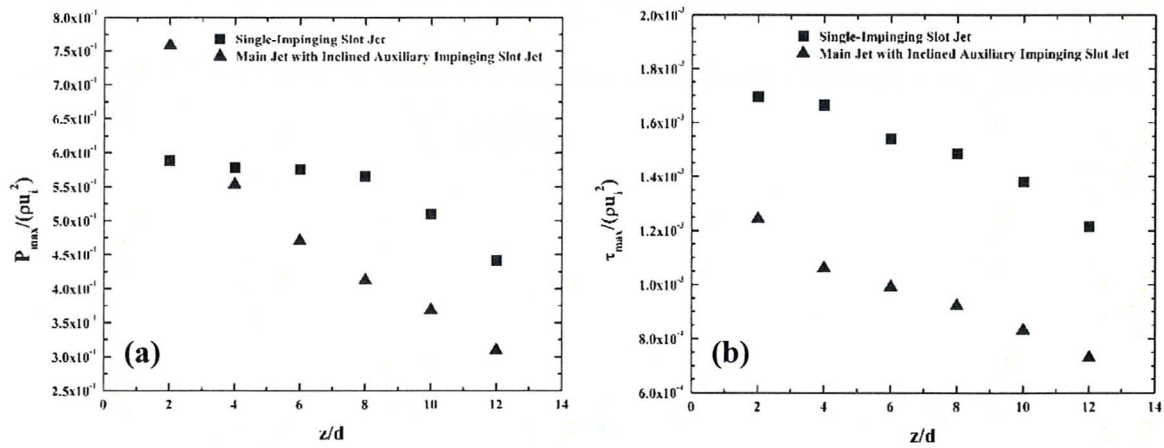


Figure 4-27: Comparison of non-dimensional maximum (a) wall pressure; and (b) wall shear stress for different  $z/d$  ratios for both configurations of a single-impinging slot jet and a main jet with inclined auxiliary impinging slot jet.

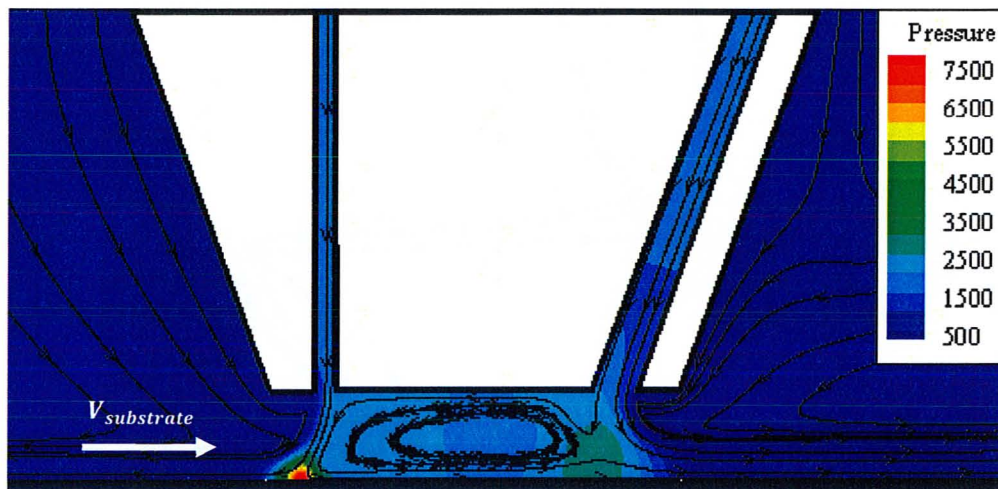


Figure 4-28: Pressure contour and streamlines for  $z/d = 4$  and  $Re_m = Re_a = 11000$ .

The quality of the coating weight cannot be predicted for this configuration but as Tu [1993] proposed this modified version of the multiple-impinging slot jets can reduce the vibration of the substrate and therefore reduce coating weight inconsistency on the moving substrate. The pressurized region can influence the quality of the final product and makes the coating weight coarse and unpleasant, while it has an insignificant effect

on the wiping process. Figure 4-29 shows the coating weight for different  $z/d$  ratios with  $V_{Strip} = 0.50 \text{ m/s}$  for this design and a conventional single-impinging slot jet model. The coating weight for this configuration is quite sensitive to  $z/d$  ratio and changes between the ranges of  $67 \text{ g/m}^2$  and  $150 \text{ g/m}^2$ , while it changes between  $70 \text{ g/m}^2$  and  $97 \text{ g/m}^2$  for a single-impinging slot jet.

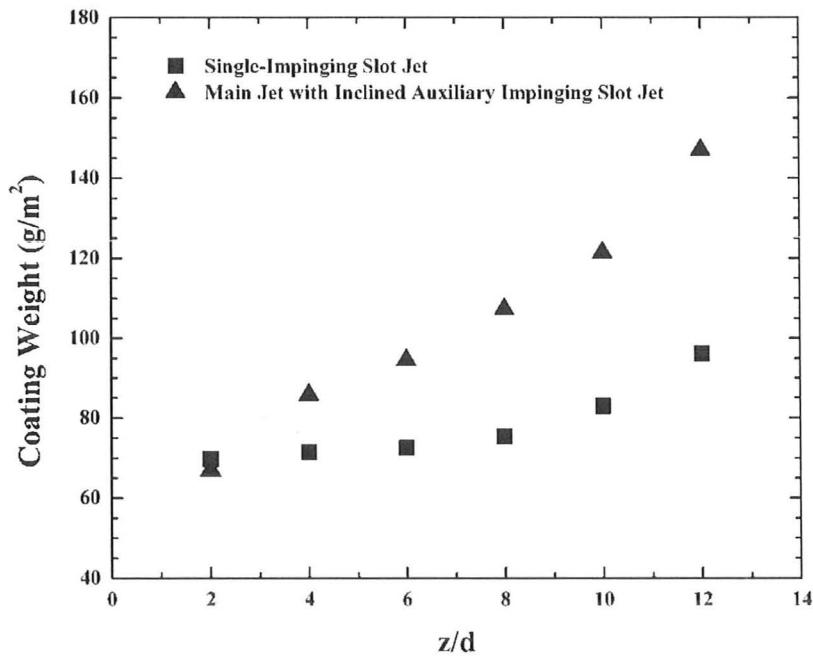


Figure 4-29: Comparison of coating weight for a single-impinging slot jet and a main with inclined auxiliary impinging slot jet for different  $z/d$  ratios, with  $V_{Strip} = 0.50 \text{ m/s}$ ,  $Re_m = 11000$  and  $Re_a = 11000$ .

Figure 4-30 shows the coating weight for different  $z/d$  ratios and  $V_{Strip}$  for the modified configuration of multiple-impinging slot jets. The trends of the results were the same as those of a single-impinging slot jet. The computed results shown in this Figure can be compared with Figure 4-8 where the coating weight results of a single-impinging slot jet were reported. The coating weight for the modified configuration is higher at a

constant strip velocity for all  $z/d$  ratios except  $z/d = 2$ . One of the major reasons is that the wall shear stress which plays key role in determining the coating weight for this configuration is less than with a single-impinging slot jet for each  $z/d$  ratio.

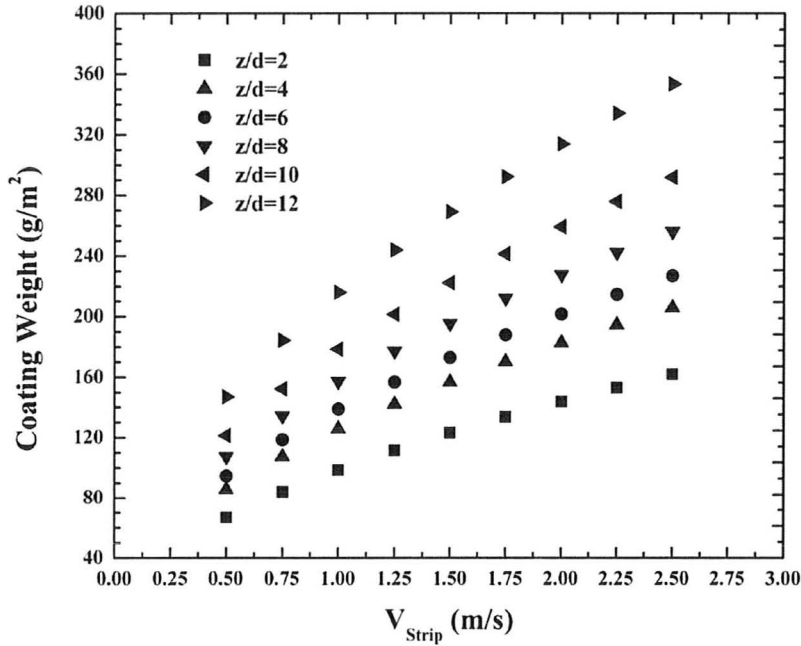


Figure 4-30: Coating weight for different  $V_{Strip}$  and  $z/d$  ratios with  $Re_m=Re_a=11000$ .

### 4.3.3 Main Slot Jet Reynolds Number Effect

The effect of main slot jet Reynolds number on the coating weight was investigated numerically for  $z/d = 4$ . The range of main slot jet Reynolds number changed between 11000 and 16000, while the auxiliary slot jet Reynolds number was fixed to 11000.

Figure 4-31 shows the non-dimensional wall pressure distributions for different  $Re_m$ , with  $Re_a=11000$  and  $z/d = 4$ . By decreasing the main slot jet Reynolds number the

impingement region goes further from the centerline of the main jet, while the non-dimensional maximum wall pressure increased with increasing  $Re_m$ . In the pressurized region the non-dimensional wall pressure overall shape was relatively constant over different  $Re_m$  but decreased with increasing  $Re_m$ . It is shown that the location of the maxima ( $x/d \approx 13$ ) is constant and is not sensitive to  $Re_m$  because the fluid flow from the main slot jet deviates to the downstream of the substrate and had insignificant impact on the location of the maxima ( $x/d \approx 13$ ), while the auxiliary slot jet has a dominant effect on the pressure magnitude and maximum location ( $10 < x/d < 15$ ) in its area.

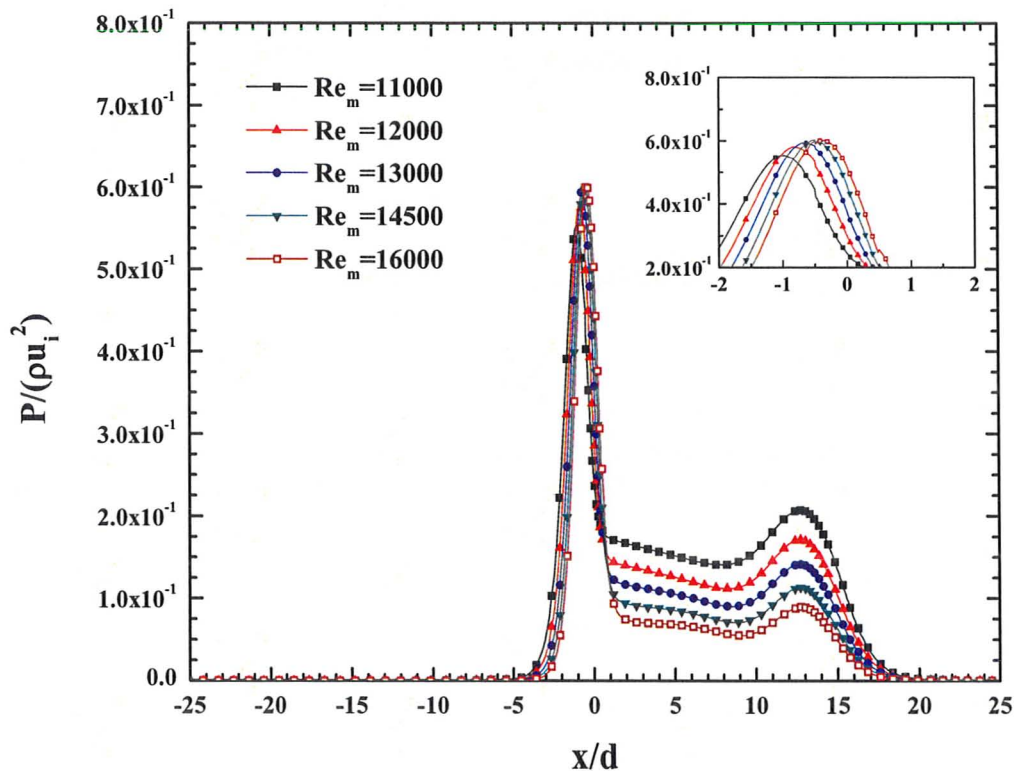


Figure 4-31: Non-dimensional wall pressure distributions for different  $Re_m$ , with  $Re_a = 11000$  and  $z/d = 4$ .

Figure 4-32 shows the non-dimensional wall shear stress distributions for different  $Re_m$ , with  $Re_a=11000$  and  $z/d=4$ . The location of the maximum shear stress moves slightly away from the centerline of the main slot jet by decreasing  $Re_m$ . In the wall jet region ( $x/d < -2.5$ ), the non-dimensional wall shear stress distribution decreased by increasing  $Re_m$ , while it is vice versa in the pressurized region ( $2 < x/d < 12$ ).

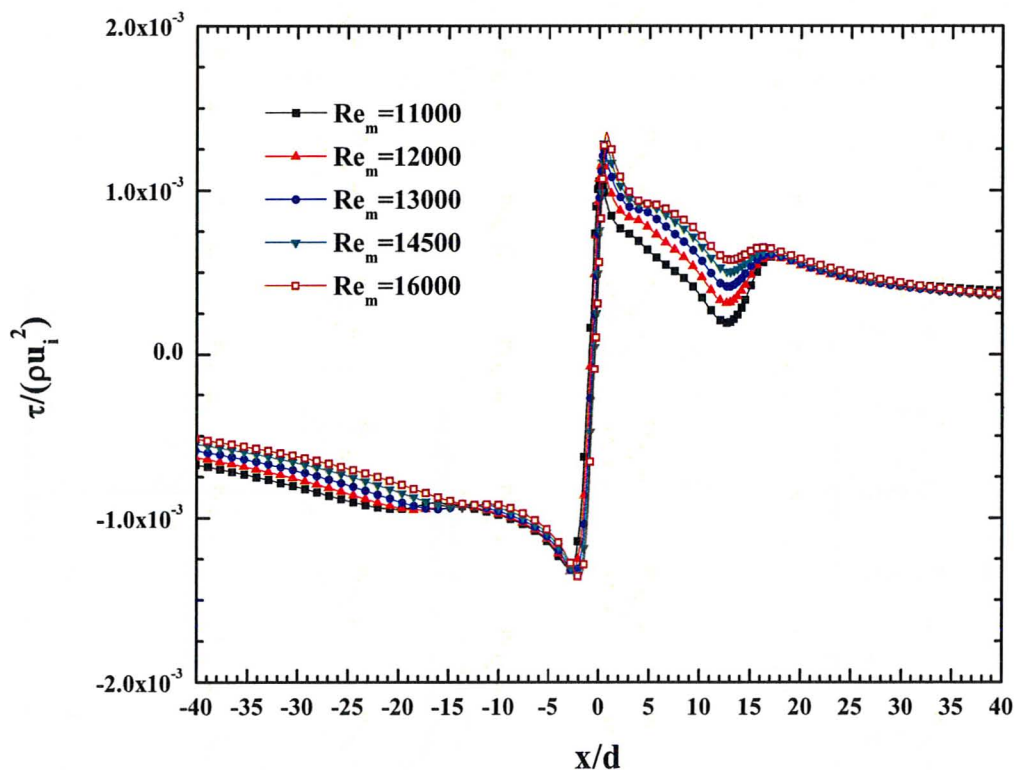


Figure 4-32: Non-dimensional wall shear stress distributions for different  $Re_m$ , with  $Re_a = 11000$  and  $z/d = 4$ .

The coating weight for different  $V_{Strip}$  and  $Re_m$ , with  $Re_a = 11000$  and  $z/d = 4$  is shown in Figure 4-33. The wall pressure profiles (Figure 4-31) and shear stress distributions (Figure 4-32) were used to estimate the coating weight on the moving substrate. The substrate moves from left to right in which the main slot jet wipes down

the excess zinc and the auxiliary impinging slot jet has no effect on wiping except creating a pressurized region in which the substrate vibration is decreased.  $Re_m$  has a significant effect on the coating weight on the moving substrate since by increasing  $Re_m$  the coating weight decreased significantly for a given value of  $V_{Strip}$ . By increasing  $Re_m$  from 11000 to 16000 the coating weight decreased up to 50% for a constant  $V_{Strip}$ . The coating weight differences of this configuration (Figure 4-33) and the conventional model of a single-impinging slot jet (Figure 4-12) for different  $Re_m$  is decreased with increasing  $Re_m$ .

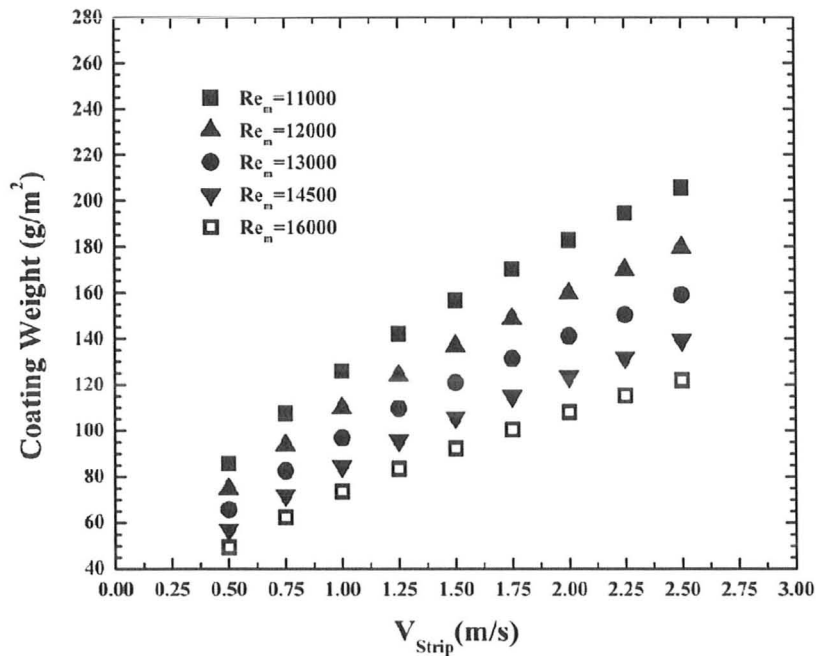


Figure 4-33: Coating weight for different  $V_{Strip}$  and  $Re_m$ , with  $Re_a = 11000$  and  $z/d = 4$ .

#### 4.3.4 Auxiliary Slot Jet Reynolds Number Effect

The effect of  $Re_a$  on the coating weight is investigated numerically in this section. The  $Re_a$  changed between 4000 and 13000, while  $Re_m = 11000$ . Figure 4-34 represents

the non-dimensional wall pressure distributions for different  $Re_a$ , with  $Re_m = 11000$  and  $z/d = 4$ . The pressure is non-dimensionalized by twice the dynamic pressure of the main slot jet ( $Re_m = 11000$ ). The location of the non-dimensional maximum impingement pressure moves further away from the centerline of the main slot jet by increasing  $Re_a$ . The non-dimensional maximum impingement pressure decreased when the auxiliary slot jet Reynolds number was greater than the main slot jet Reynolds number. The pressure in the pressurized region ( $0 \lesssim x/d < 15$ ) increased by increasing the auxiliary jet Reynolds number, while the maxima location ( $13 < x/d < 15$ ) moves further away from the centerline of the main slot jet.

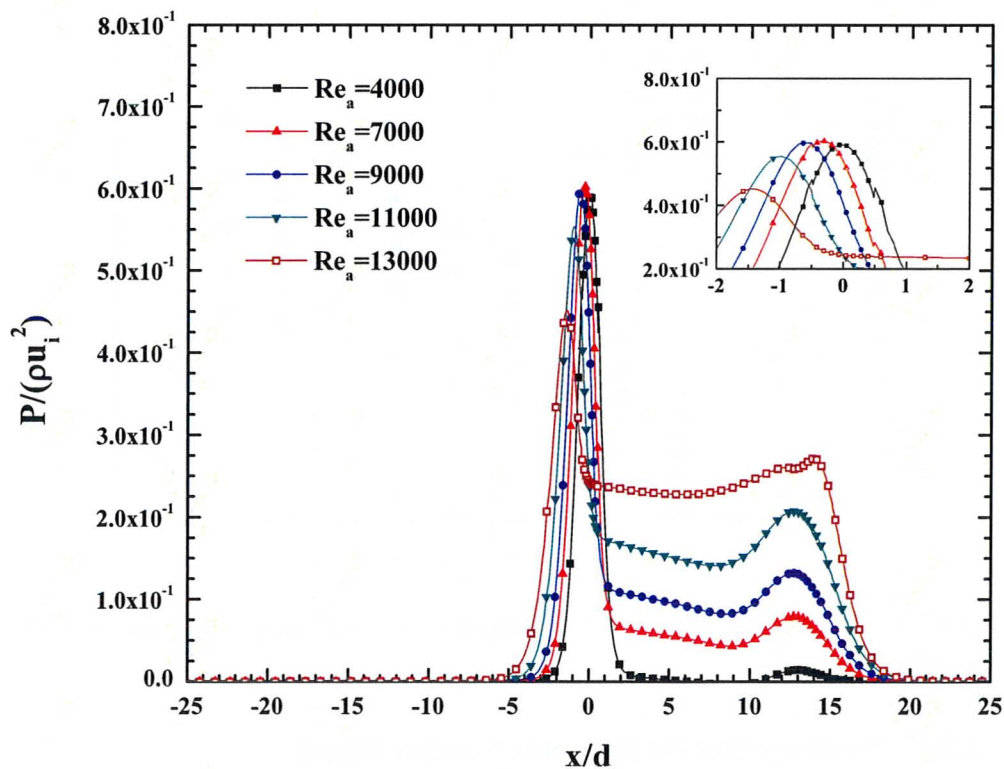


Figure 4-34: Non-dimensional wall pressure distributions for different  $Re_a$ , with  $Re_m = 11000$  and  $z/d = 4$ .

Figure 4-35 shows the non-dimensional wall shear stress distributions for different  $Re_a$ , with  $Re_m = 11000$  and  $z/d = 4$ . By increasing the  $Re_a$ , the maximum non-dimensional shear stress ( $-5 < x/d < 0$ ) decreased and moved further away from the centerline of the main slot jet, while the non-dimensional wall shear stress in the wall jet region increased. The wall shear stress in the pressurized region decreased by increasing  $Re_a$ , while it was quite insensitive in the wall jet region ( $x/d > 16$ ).

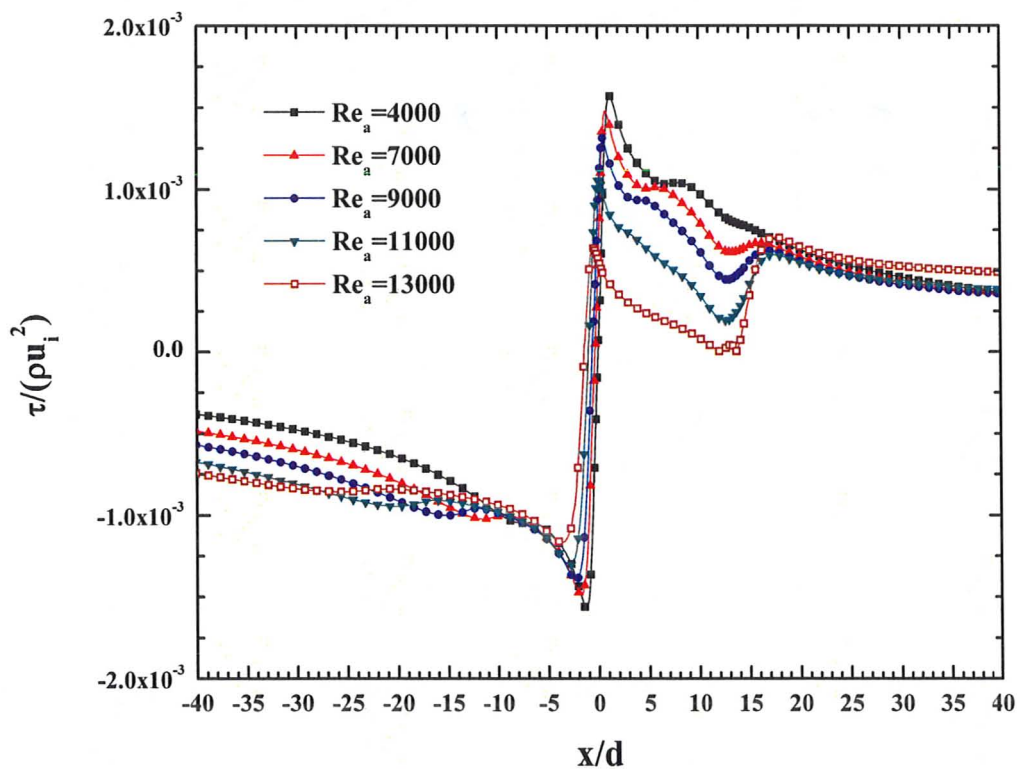


Figure 4-35: Non-dimensional wall shear stress distributions for different  $Re_a$ , with  $Re_m = 11000$  and  $z/d = 4$ .

The wall pressure and shear stress distributions were used to estimate the coating weight on the moving substrate. Figure 4-36 represents the coating weight for different  $Re_a$  and  $V_{Strip}$ , with  $Re_m = 11000$  and  $z/d = 4$ . It is shown that by increasing  $Re_a$  the

coating weight increased. It can be seen for all  $Re_a$  the coating weight increased with increasing substrate velocity. By increasing the substrate velocity, the differences between the coating weights of the cases with various  $Re_a$  were increased.

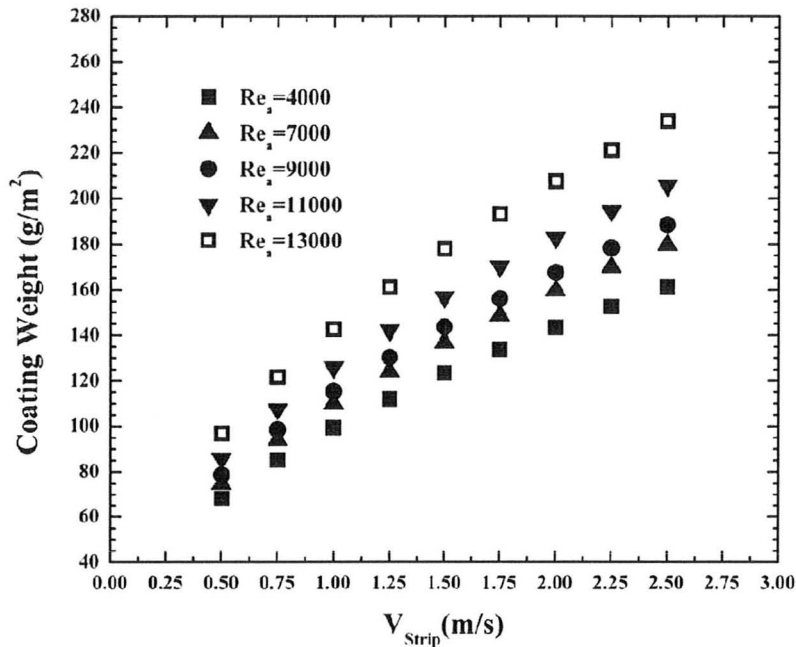


Figure 4-36: Coating weight for different  $V_{Strip}$  and  $Re_a$ , with  $Re_m = 11000$  and  $z/d = 4$ .

### 4.3.5 Wall Thickness-to-Nozzle Ratio Effect

In this section, the effect of wall thickness-to-nozzle ratios ( $a/d$ ) on the coating weight on a moving substrate is examined numerically. Figure 4-37(a) shows the non-dimensional pressure distributions for  $a/d$  ratios changing between the range of 4 and 15 with  $Re_m = Re_a = 11000$  and  $z/d = 4$ . It is shown that by changing the  $a/d$  ratio there is no effect on the maximum impingement pressure value and location. The pressure loss in the pressurized region was not sensitive to  $a/d$  ratio. Figure 4-37(b) shows the non-dimensional wall shear stress distributions for different  $a/d$  ratios. According to this

Figure the non-dimensional maximum wall shear stress is not sensitive to  $a/d$  ratios. The coating weight on the moving substrate based on the wall pressure profiles and shear stress results (Figure 4-37) were estimated numerically and the results for different  $a/d$  ratios and  $V_{Strip}$ , with  $Re_m = Re_a = 11000$  and  $z/d = 4$  are shown in Figure 4-38.

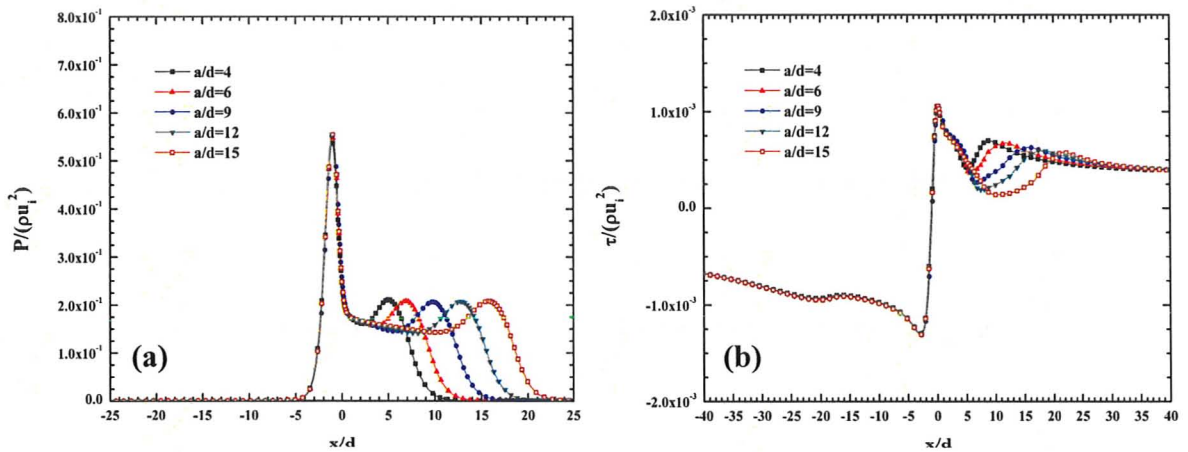


Figure 4-37: Non-dimensional (a) wall pressure (b) wall shear stress distributions for different  $a/d$  ratios, with  $Re_m = Re_a = 11000$  and  $z/d = 4$ .

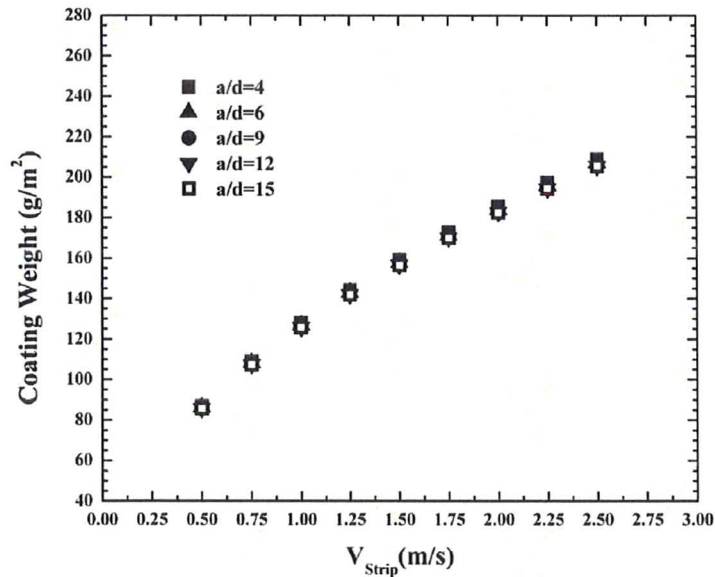


Figure 4-38: Coating weight for different  $a/d$  ratios and  $V_{Strip}$ .

The coating weight is not sensitive to  $a/d$  ratios because the auxiliary slot jet is downstream of the main jet. For all  $a/d$  ratios the coating weight increased with increasing strip velocity. In the next section, a modified version of the multiple-impinging slot jets with one main jet and two inclined auxiliary slot jets is developed numerically to estimate the coating weight on the moving substrate.

#### **4.4 Main Jet with Two Adjacent Inclined Auxiliary Impinging Slot Jets**

In this section, a modified version of multiple-impinging slot jets with one main slot jet and two adjacent inclined auxiliary impinging slot jets, developed by Kim *et al.* [2008], discharging air at lower velocity in comparison with the main slot jet is investigated numerically. The motivation of having two auxiliary slot jets is to stabilize the main slot jet. The coating weight on the moving substrate was estimated for different plate-to-nozzle ratios, main jet Reynolds numbers, auxiliary slot jets Reynolds numbers and ratio between the distance of the main slot jet and auxiliary impinging slot jet to nozzle gap.

##### **4.4.1 Geometry, Boundary and Initial Conditions**

Figure 4-39 shows the geometry of this configuration. The main impinging slot jet is perpendicular to the strip and the angle between the main jet and auxiliary slot jets is fixed at 20 degrees. The properties of the auxiliary slot jets are the same as the auxiliary impinging slot jet in the previous configuration. The turbulent length scale was set to  $2.13 \times 10^{-4}$  for the main slot jet and  $4.26 \times 10^{-4}$  for each of the auxiliary impinging slot jets, correspondingly. The effect of plate-to-nozzle ratios ( $z/d$ ) changing between 2 and 12,

main slot jet Reynolds numbers ( $Re_m$ ) changing between 11000 and 16000, auxiliary slot jets Reynolds numbers ( $Re_a$ ) changed between 4000 and 13000 simultaneously and the ratio between the distance of the main slot jet to auxiliary impinging slot jet to main slot gap ( $s/d$ ) changing between 4.93 and 13.15 on the coating weight on the moving substrate were investigated numerically. The substrate was considered fixed and the pressure at the far-field boundary condition was set to atmospheric pressure. Figure 4-39 shows the geometry of this configuration.

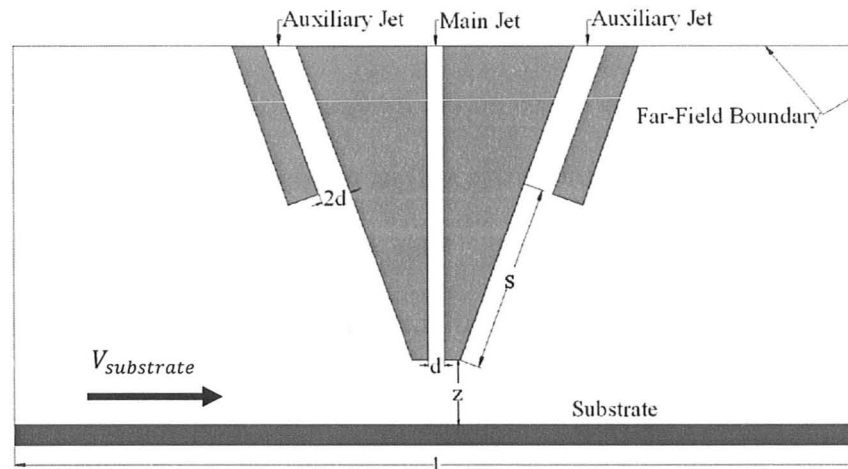


Figure 4-39: Schematic for a main with two adjacent inclined auxiliary impinging slot jets.

#### 4.4.2 Plate-to-Nozzle Ratios Effect

In this section, the effect of  $z/d$  ratio on the wall pressure and shear stress results and consequently the coating weights on a moving substrate are investigated. The results of the flow field and coating weight are compared with the results of the conventional model of a single-impinging slot jet. Figure 4-40 represents the non-dimensional wall pressure distributions for different  $z/d$  ratios with  $s/d = 13.15$  and  $Re_m = Re_a = 11000$ .

The auxiliary impinging slot jets shape the pressure profile for  $z/d < 6$  and for  $z/d > 6$  the shoulders seen in the pressure profile for lower  $z/d$  disappear. The auxiliary impinging slot jets modify the shape of the wall pressure profile, and increase the pressure along the wall compared to the results of a single-impinging slot jet (Figure 4-3).

Figure 4-41 shows the non-dimensional wall shear stress profiles for different  $z/d$  ratios with  $s/d = 13.15$  and  $Re_m = Re_a = 11000$ . In the impingement region the non-dimensional wall shear stress is not sensitive to  $z/d$  ratio, while in the wall jet region the wall shear stress decreased with increasing  $z/d$ . The auxiliary impinging slot jets reduce the value of the maximum shear stress on the moving substrate. The fluid flow from the auxiliary slot jets mix with the flow in the wall jet region of the main slot jet and increase the speed of the flow on the substrate. This velocity increment is a main cause in increasing the wall shear stress for this configuration in comparison with the conventional single-impinging slot jet case. Kim *et al.* [2008] did experimental measurements on estimating the splashing limit for this configuration and predicted that this model restrains zinc from splashing.

The non-dimensional maximum wall pressure and shear stress for different  $z/d$  ratios for both configurations of a single-impinging slot jet (Figure 4-2) and a modified version of multiple-impinging slot jets (Figure 4-39) are shown in Figure 4-42. It is shown in Figure 4-42(a) that the non-dimensional maximum wall pressure for the modified configuration of multiple-impinging slot jets is higher than for a single-impinging slot jet for all  $z/d$  ratios and decreased continuously with increasing  $z/d$ ,

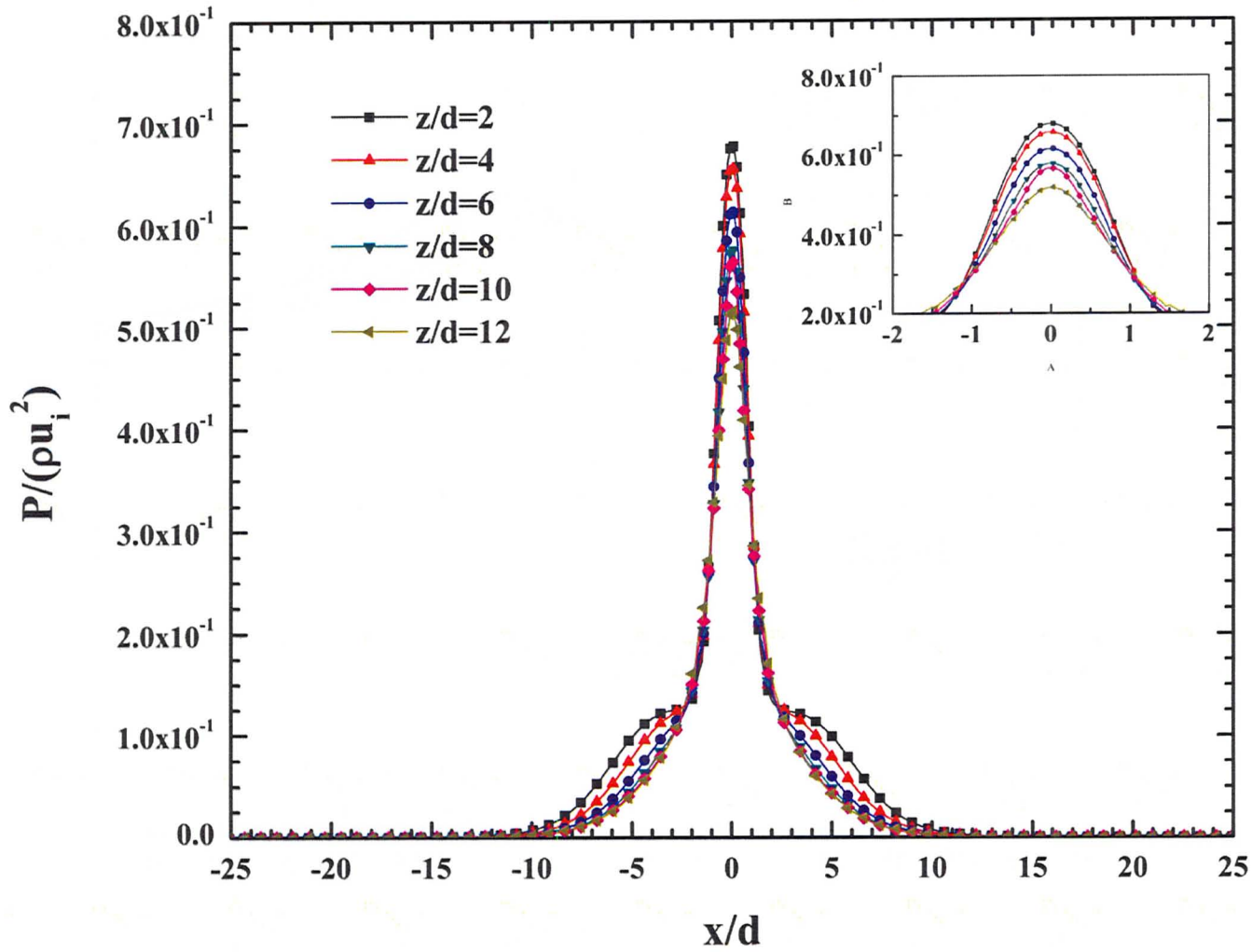


Figure 4-40: Non-dimensional wall pressure distributions for different  $z/d$ , with  $s/d = 13.15$  and  $Re_m = Re_a = 11000$ .

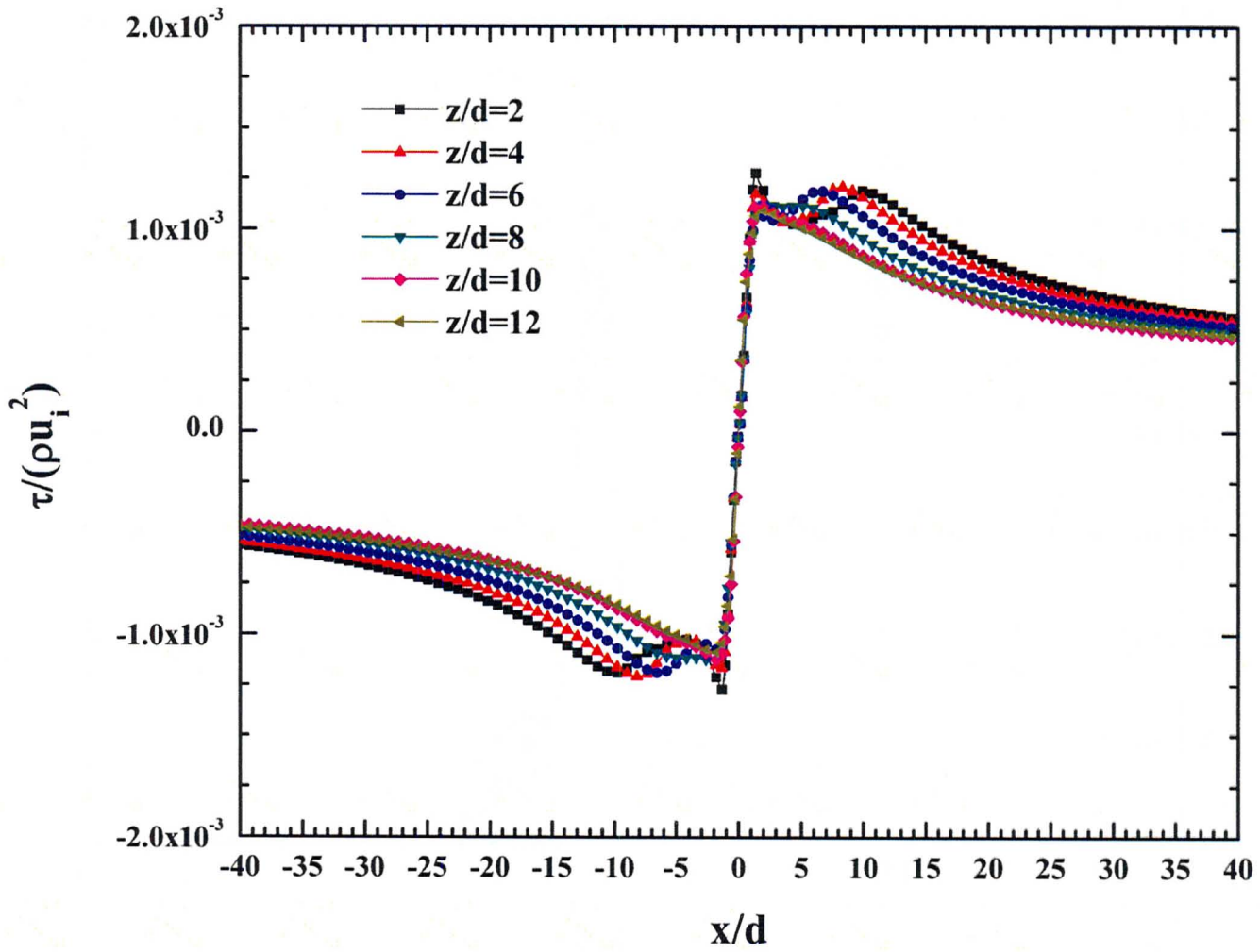


Figure 4-41: Non-dimensional shear stress distributions for different  $z/d$ , with  $s/d = 13.15$  and  $Re_m = Re_a = 11000$ .

where the largest difference was approximately around 14% for  $z/d = 2$  and the smallest difference about 2% for  $z/d = 8$ . Figure 4-42(b) shows the non-dimensional maximum wall shear stress. For both configurations this property decreased with increasing  $z/d$  ratio, while the rate of shear stress decrement for a single-impinging slot jet was higher than the modified multiple-impinging slot jets. The value of the maximum shear stress was higher for the conventional model for each  $z/d$  ratio. The largest difference between the maximum wall shear stress was about 27.5% for  $z/d = 4$ , while the smallest one was approximately 10.7% for  $z/d = 12$ .

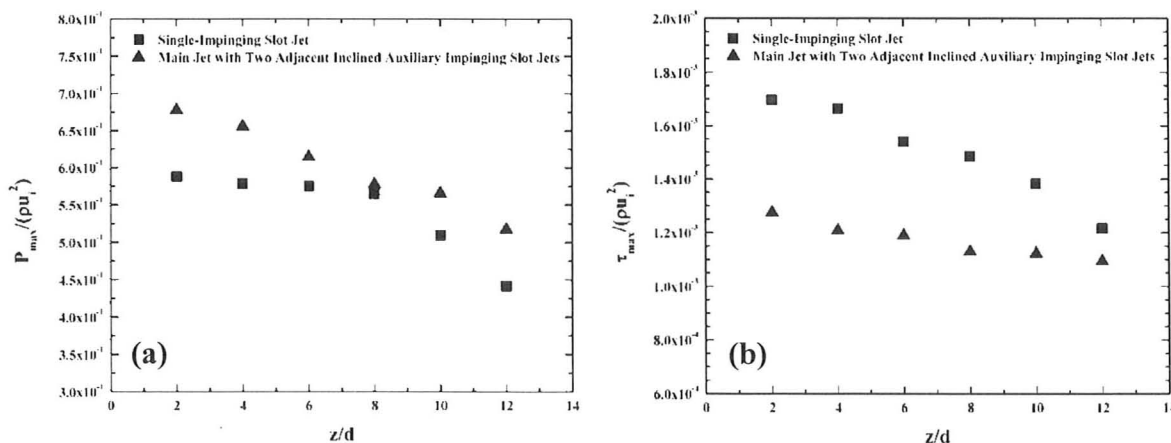


Figure 4-42: Comparison of non-dimensional maximum (a) wall pressure; and (b) shear stress for different  $z/d$  ratios.

The pressure contour and streamlines with  $z/d = 4$ ,  $s/d = 13.15$  and  $Re_m = Re_a = 11000$  is shown in Figure 4-43. Figure 4-43 can be compared to Figure 4-6, the single slot case, and we see that the fluid flow from the auxiliary slot jets shape the wall pressure profiles (Figure 4-40), increase the value of the maximum impingement pressure

(Figure 4-42(a)), and decrease the maximum wall shear stress on the substrate (Figure 4-42(b)).

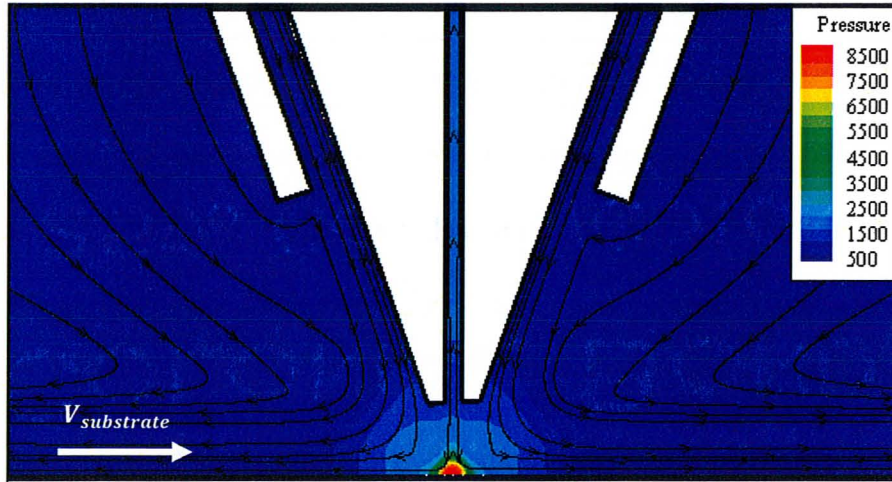


Figure 4-43: Pressure contour and streamlines with  $z/d = 4$ ,  $s/d = 13.15$  and  $Re_m = Re_a = 11000$ .

Figure 4-44 shows a comparison of the coating weights for a single-impinging slot jet and modified multiple-impinging slot jets for different  $z/d$  ratios with  $V_{Strip} = 0.50$  m/s,  $Re_m = 11000$  and  $Re_a = 11000$ . It is shown that the coating weight of this modified model is sensitive to the  $z/d$  ratio and increased with increasing  $z/d$ . According to this Figure, the coating weight for this configuration is greater than the single-impinging slot jet case for each  $z/d$  ratio, with the largest difference of about 14.74% for  $z/d = 8$  and the smallest about 3.22% for  $z/d = 12$ . The coating weight on a moving substrate of this configuration for different  $z/d$  ratios and  $V_{Strip}$  with  $Re_m = Re_a = 11000$  is shown in Figure 4-45.

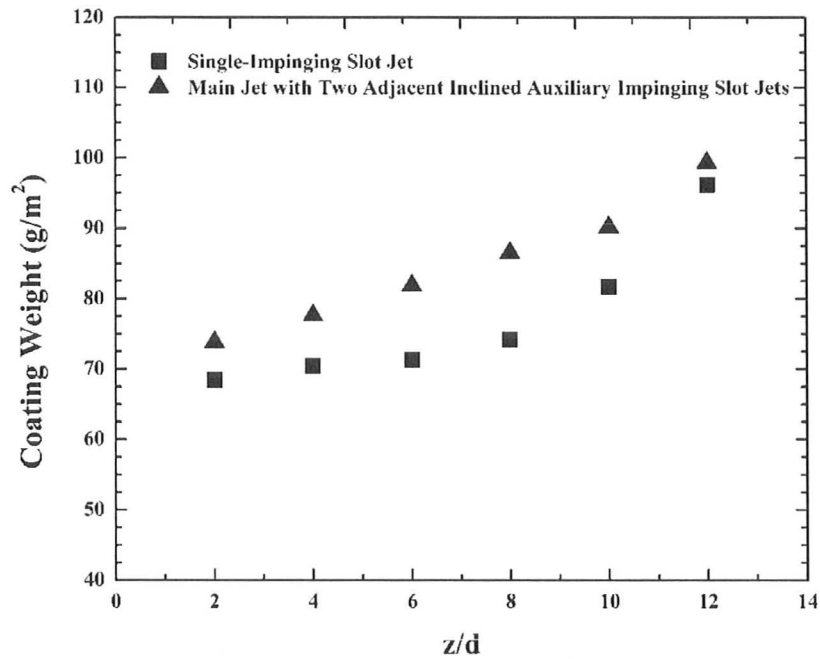


Figure 4-44: Comparison of coating weight for a single-impinging slot jet and a main with two adjacent inclined auxiliary impinging slot jets for different  $z/d$  ratios, with  $V_{Strip} = 0.50 \text{ m/s}$ ,  $Re_m = 11000$  and  $Re_a = 11000$ .

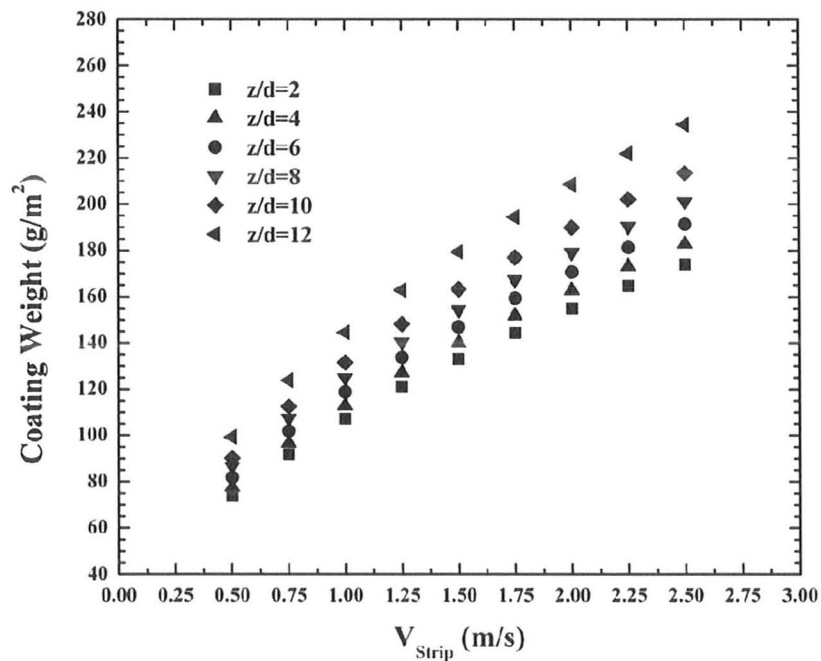


Figure 4-45: Coating weight for different  $V_{Strip}$  and  $z/d$  ratios with  $Re_m = Re_a = 11000$ .

By increasing the strip velocity the coating weight increased significantly and by comparing this Figure to Figure 4-8, it is shown that for each  $z/d$  ratio and  $V_{strip}$  the coating weight for a conventional model will be less than for this configuration. The main slot jet Reynolds numbers effect on the coating weight is investigated in the next section.

#### 4.4.3 Main Slot Jet Reynolds Number Effect

The effect of main slot jet Reynolds number on the coating weight is investigated in this section. The  $Re_m$  changed between 11000 and 16000 with  $z/d = 4$  and  $Re_a = 11000$ . This configuration (Figure 4-39) can be designed in a manner such that the main slot jet and auxiliary slot jets work separately. According to the above statement, the effect of the main slot jet Reynolds numbers on the coating weight can be studied independently, while the auxiliary slot jet Reynolds number is fixed. The non-dimensional pressure profiles for different  $Re_m$  with  $Re_a = 11000$  and  $z/d = 4$  is shown in Figure 4-46. According to this Figure, the non-dimensional maximum wall pressure decreased with increasing  $Re_m$  and the non-dimensional pressure value is larger for this configuration versus the single-impinging slot jet case (Figure 4-9). It is shown that the effect of  $Re_a$  on the pressure profiles decreased with increasing  $Re_m$  ( $-10 < x/d < -2$  and  $2 < x/d < 10$ ).

The non-dimensional wall shear stress results for different  $Re_m$  is shown in Figure 4-47. In the impingement region ( $-2 \lesssim x/d \lesssim 2$ ) the non-dimensional wall shear stress is not sensitive to  $Re_m$ , while in the wall jet region ( $x/d \lesssim -2$  and  $x/d \gtrsim 2$ ) the non-

dimensional wall shear stress decreased with increasing  $Re_m$ . The maximum value of the non-dimensional wall shear stress for this configuration for each  $Re_m$  is less than the value for a conventional single-impinging slot jet (Figure 4-10).

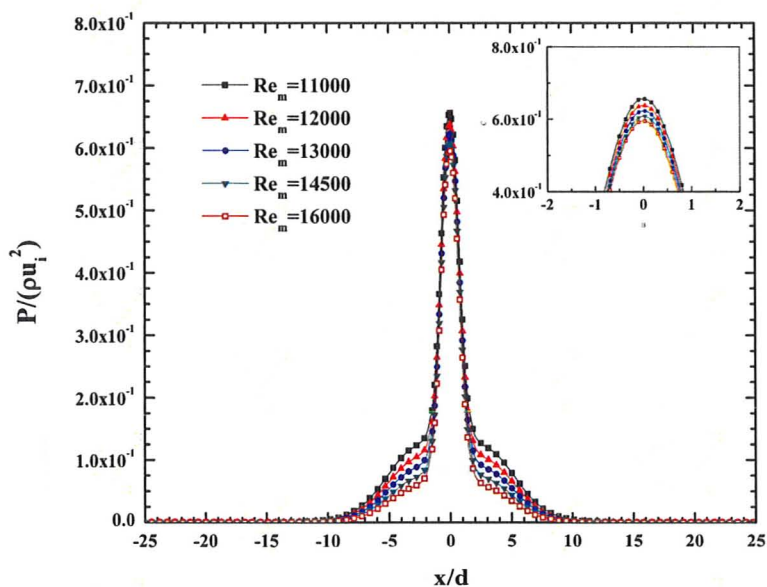


Figure 4-46: Non-dimensional wall pressure distributions for different  $Re_m$ , with  $Re_a = 11000$  and  $z/d = 4$ .

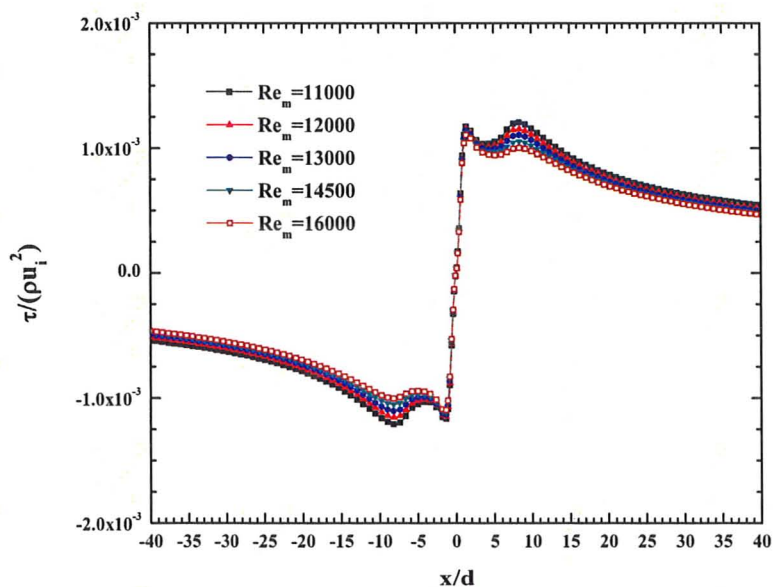


Figure 4-47: Non-dimensional wall shear stress distributions for different  $Re_m$ , with  $Re_a = 11000$  and  $z/d = 4$ .

Figure 4-48 shows the coating weight on a moving substrate for different  $Re_m$  and  $V_{Strip}$ , with  $Re_a = 11000$  and  $z/d = 4$ . By increasing  $Re_m$  the coating weight decreased for each  $V_{Strip}$  and increased with increasing strip velocity. The results achieved in this section can be compared with the single-impinging slot jet coating weight data shown in Figure 4-12. It is concluded that the coating weight for this configuration is higher for each  $Re_m$  and  $V_{Strip}$ . It should be noted that the coating weight results are not verified by any experimental measurements and are estimated using the analytical formula proposed in Chapter 2.

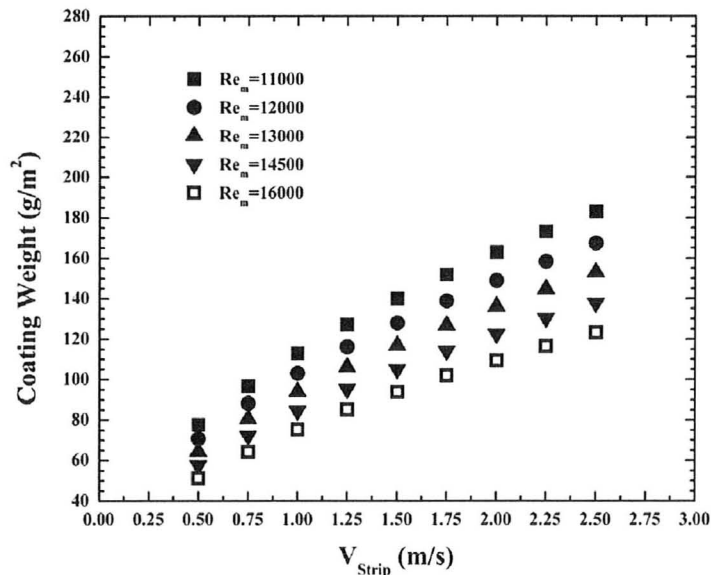


Figure 4-48: Coating weight for different  $Re_m$  and  $V_{Strip}$  with  $z/d = 4$  and  $Re_a = 11000$ .

#### 4.4.4 Auxiliary Slot Jets Reynolds Number Effect

It was noted in the last section that this configuration can be designed in a way that both main and auxiliary slot jets work independently. For this reason the effect of auxiliary slot jets Reynolds numbers on the coating weight is investigated numerically,

while the main slot jet Reynolds number was fixed. Figure 4-49 shows the non-dimensional wall pressure distributions and wall shear stress results for different  $Re_a$  ranging between 4000 and 13000 with  $Re_m = 11000$  and  $z/d = 4$ . The wall pressure and wall shear stress are non-dimensionalized by two times of the dynamic pressure of the main slot jet. It is shown in Figure 4-49(a) that the non-dimensional maximum wall pressure, which is under the centerline of the main slot jet, is sensitive to  $Re_a$  and increased with increasing  $Re_a$ . The shoulder effect on the wall pressure ( $-10 < x/d < -2$  and  $2 < x/d < 10$ ) increased with increasing  $Re_a$ . Figure 4-49(b) represents the non-dimensional wall shear stress results for this case. In the impingement region the non-dimensional wall shear stress was not sensitive to  $Re_a$ , while in the wall jet region this property increased by increasing  $Re_a$  because the flow from these slot jets has more momentum and increased the velocity of the wall jet region discharge from the main slot jet.

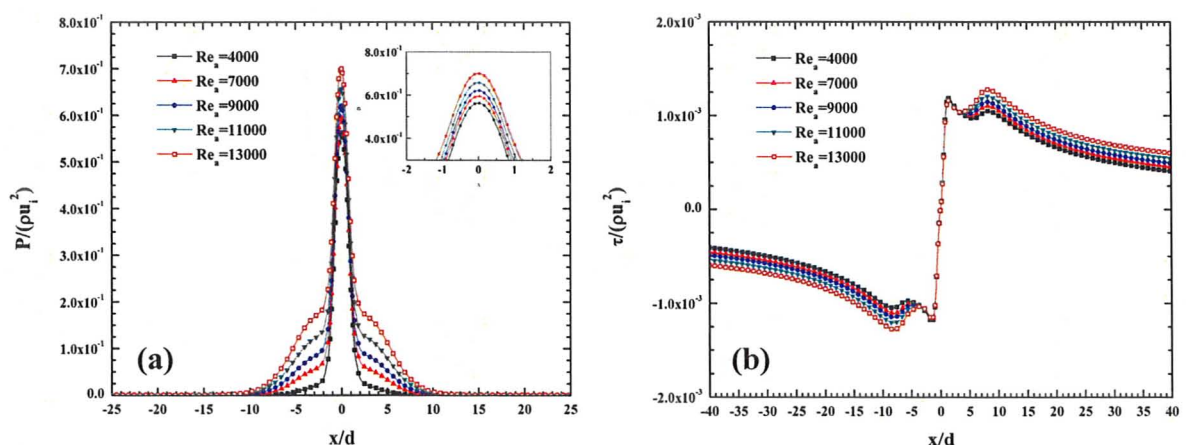


Figure 4-49: Non-dimensional (a) wall pressure; and (b) wall shear stress distributions for different  $a/d$  ratios, with  $Re_m = Re_a = 11000$  and  $z/d = 4$ .

The coating weight results are shown in Figure 4-50. Increasing  $Re_a$  did not have any significant effect on the coating weight on a moving substrate with  $z/d = 4$  and  $Re_m = 11000$ . The effect of  $Re_a$  on the coating weight with  $z/d = 10$  and  $Re_m = 11000$  is investigated in Figure 4-51. By increasing  $Re_a$  the coating weight increased for each  $V_{Strip}$  and increased with increasing strip velocity.

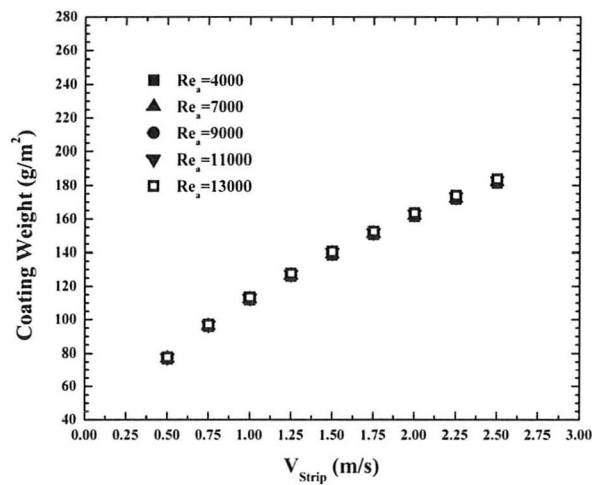


Figure 4-50: Coating weight for different  $V_{Strip}$  and  $Re_a$ , with  $Re_m = 11000$  and  $z/d = 4$ .

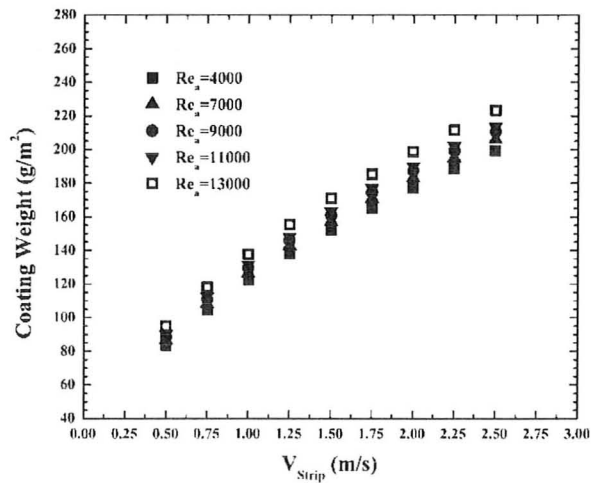


Figure 4-51: Coating weight for different  $V_{Strip}$  and  $Re_a$ , with  $Re_m = 11000$  and  $z/d = 10$ .

#### 4.4.5 The Ratio Between the Distance of the Main Slot Jet and Auxiliary Slot Jet to Nozzle Gap Effect

In this section, the effect of  $s/d$  ratio changing between 4.93 and 13.15 on the coating weight is investigated with  $Re_m = Re_a = 11000$  and  $z/d = 4$ . The effect of this ratio on the wall pressure and wall shear stress distributions are quite negligible and consequently make the coating weight results consistent over different  $s/d$  ratios, as is shown in Figure 4-52 for  $V_{strip} = 0.50$  m/s.

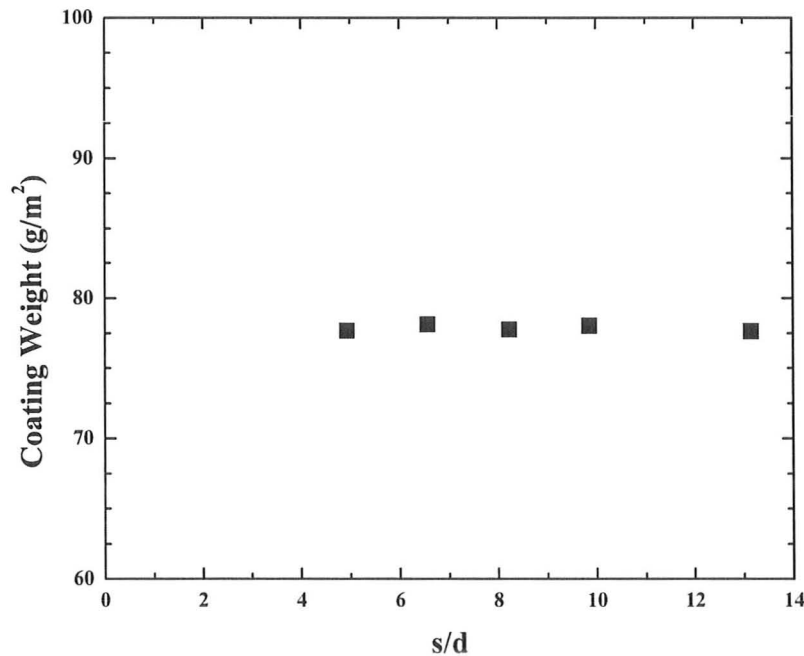


Figure 4-52: Coating weight for different  $s/d$  ratios, with  $V_{strip} = 0.50$  m/s and  $Re_m = Re_a = 11000$  and  $z/d = 4$ .

For this configuration the  $s/d$  ratio cannot be less than or equal to 3.28 because the interaction of the fluid flow from the auxiliary slot jets and main impinging slot jet is high and makes the flow field unsteady. Figure 4-53 represents the impingement pressure under the centerline of the main slot jet versus time ( $2 < t < 20$ ) for  $s/d = 3.28$ . It can be

seen that this configuration ( $s/d \leq 3.28$ ) is not practical for the wiping process since the unsteady flow field makes the coating weight non-uniform.

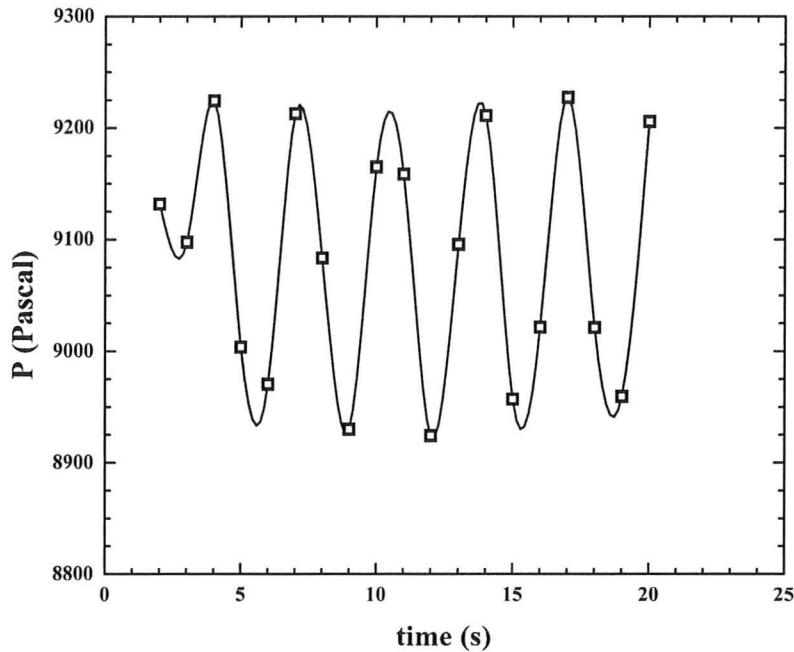


Figure 4-53: Pressure under the centerline of the main slot jet with respect to time for  $s/d=3.28$  ratios, with  $Re_m = Re_a = 11000$  and  $z/d = 4$ .

#### 4.5 Comparison Between the Coating Weights for All Configurations

In this section, the predicted coating weight results for all turbulent impinging slot jet configurations are compared with each other. Figure 4-54 shows the coating weight for different  $z/d$  ratios with  $Re_m = Re_a = 11000$  and  $V_{Strip} = 0.50 \text{ m/s}$  where the cases are represented as follows:

Case 1: Single-Impinging Slot Jet

Case 2: Two Parallel Impinging Slot Jets

Case 3: Main Jet with Inclined Auxiliary Impinging Slot Jet

## Case 4: Main Jet with Two Adjacent Inclined Auxiliary Impinging Slot Jets

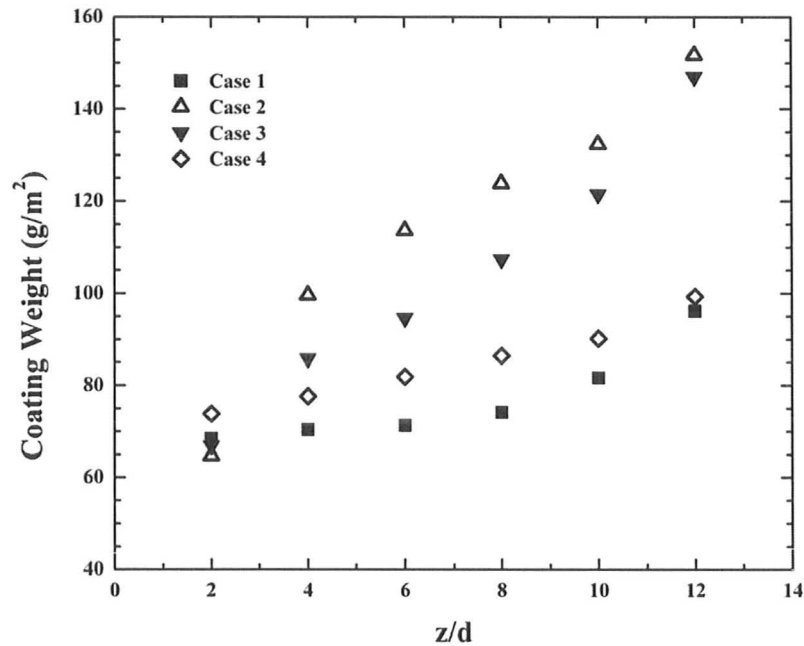


Figure 4-54: Coating weight for different turbulent impinging slot jet configurations with  $V_{Strip} = 0.50 \text{ m/s}$  and  $Re_m = Re_a = 11000$  and  $z/d = 4$ .

By assuming Case 1 as a base case for comparison, it is shown that the predicted coating weight results for all multiple-impinging slot jet configurations are higher than the base case for different  $z/d$  ratios except for  $z/d = 2$  for Case 2 and Case 3. For all multiple-impinging slot jet cases, the coating weight results are sensitive to  $z/d$  and increase significantly for Case 2 and Case 3. The rate of increment of coating weight results is low for Case 4. The coating weight results are not robust for different multiple-impinging slot jet configurations for different  $z/d$ . Kim *et al.* [2008] proposed that the configuration with main jet with two adjacent inclined auxiliary impinging slot jets (Case 4) has an advantage of delaying the splashing limit on the moving sheet substrate in comparison with the conventional model of a single-impinging slot jet (Case 1). They

claimed that in the wall jet region, the wall shear stress distribution for Case 4 is lower than Case 1 and this delays the splashing of molten liquid zinc from the moving sheet substrate, while the numerical simulations showed that the wall shear stress in wall jet region for Case 4 is higher than Case 1. The determination of splashing limit for Case 4 needs experimental measurements, while the numerical simulation studied in this research project is not an appropriate tool for estimating the splashing limit.

## Chapter 5: Conclusions and Proposals for Future Work

### 5.1 Conclusions

Numerical simulations for different configurations of turbulent impinging slot jets were carried out in this research using FLUENT commercial code to estimate the air knife wall pressure and shear stress profiles for the purpose of predicting the coating weight on the moving substrate using a 2-D steady state model. The turbulence model used in this research project was the standard  $k - \varepsilon$  model with non-equilibrium wall treatments as previously used by Elsaadawy *et al.* [2007].

For the two parallel impinging slot jets configuration, the maximum impingement pressure deviates from the centerline of the main slot jet and moved further away from the centerline of the jet with increasing  $z/d$  ratio. The predicted coating weight of this model was quite sensitive to  $z/d$ . A modified version of the multiple-impinging slot jets with a main slot jet and an inclined auxiliary impinging slot jet discharging air at lower velocity in comparison with the main slot jet was also simulated. The coating weight for this configuration was fairly responsive to  $z/d$  ratio and increased significantly by increasing this ratio. The final model which was developed in this research was proposed by Kim *et al.* [2008] and involved a centre jet with symmetric tilted adjacent slot jets. The coating weight estimated for this configuration for different  $z/d$  ratios was compared to a single-impinging slot jet base case. Although, the standard  $k - \varepsilon$  turbulence model had some difficulty in predicting the length of the potential core for a single-impinging slot jet case, the wall pressure results and wall shear stress distributions obtained through

this model and the resultant coating weight based on earlier studies with acceptable agreement with industrial data makes this model reliable for air-coating. Because there were no experimental coating weight data available for multiple-impinging slot jets for a comparison with the conventional model, the  $k - \varepsilon$  turbulence model was used to capture the flow field results which were used later to estimate the coating weight on the moving substrate. The predicted coating weight results gave a reasonable trend of coating weight change for different  $z/d$  ratios,  $Re_m$ ,  $Re_a$  and  $a/d$  ratios.

## 5.2 Proposals for Future Work

The opportunity for additional research on this field is endless. The simplified 2-D models presented in this research were only useful in determining the trends of coating weight data for different configurations of turbulent impinging slot jets. The wall pressure results and wall shear stress distributions for different multiple-impinging slot jets need to be measured experimentally and the calculated data compared with numerical results available in this research for verification. The wall pressures are fairly simple to measure using pressure transducer sensors, while determining the wall shear stress distributions are quite complex and need careful investigation. The flow field can also be obtained using PIV images and later compared with the numerical velocity and vorticity fields. Another branch of research with turbulent impinging slot jets should be using 3-D numerical simulations with complex turbulence models such as LES or DNS and compare the obtained results with the 2-D data presented in this research to determine whether there are any significant differences between the predicted coating weight results or not.

The numerical domain can be solved using two-phase flow in which the liquid side can be modeled on the moving substrate. In this case the shape of the liquid film can be predicted more accurately using different turbulent impinging slot jet configurations.

It is obvious that there is still huge room for progress in the area of turbulent impinging slot jets. The basic tools are available to accomplish this work, to expand our knowledge behind it, and to build more efficient impinging slot jets in order to reach consistent coating weight with better quality.

## References

- Ahn, K. J. and M. K. Chung (2006). "A noble gas wiping system to prevent the edge overcoating in continuous hot-dip galvanizing." *ISIJ International* 46(4): 573-578.
- Arthurs, D., (2007). "Noise generation in the gas wiping process." Master of Science dissertation, McMaster University, Hamilton, ON.
- Beaubert, F. and S. Viazzo (2003). "Large eddy simulations of plane turbulent impinging jets at moderate Reynolds numbers." *International Journal of Heat and Fluid Flow* 24(4): 512-519.
- Beltaos, S., and Rajaratnam, N., (1976). "Plane turbulent impinging jets." *J. Hydraul. Res.*, 11: 29–59.
- Buchlin J. M., M. Manna, et al. (1996). European coating symp. on the mechanism of thin film coating, 168.
- Cho, T. S., Y. D. Kwon, et al. (2009). "A Study of the influence of air-knife tilting on coating thickness in hot-dip galvanizing." *Journal of Thermal Science* 18(3): 262-267.
- Chung, Y. M. and K. H. Luo (2002). "Unsteady heat transfer analysis of an impinging jet." *Journal of Heat Transfer-Transactions of the ASME* 124(6): 1039-1048.
- Cziesla, T., G. Biswas, et al. (2001). "Large-eddy simulation of flow and heat transfer in an impinging slot jet." *International Journal of Heat and Fluid Flow* 22(5): 500-508.
- Ellen, C. H. and C. V. Tu (1984). "An analysis of jet stripping of liquid coatings." *Journal of Fluids Engineering-Transactions of the ASME* 106(4): 399-404.
- Elsaadawy, E. A., G. S. Hanumanth, et al. (2007). "Coating weight model for the continuous hot-dip galvanizing process." *Metallurgical and Materials Transactions B-Process Metallurgy and Materials Processing Science* 38(3): 413-424.

Fernandez, J. A., J. C. Elicer-Cortes, et al. (2007). "Comparison of low-cost two-equation turbulence models for prediction flow dynamics in twin-jets devices." *International Communications in Heat and Mass Transfer* 34(5): 570-578.

Ferziger, J. H. and M. Peric (2002). *Computational methods for fluid dynamics*. Berlin ; New York, Springer.

FLUENT 6.3 User's Guide (2006), Fluent Inc., Lebanon, NH.

Gau, C. and C. M. Chung (1991). "Surface curvature effect on slot-air-jet impingement cooling flow and heat-transfer process." *Journal of Heat Transfer-Transactions of the ASME* 113(4): 858-864.

Gau, C. and C. C. Lee (1992). "Impingement cooling flow structure and heat-transfer along rib-roughened walls." *International Journal of Heat and Mass Transfer* 35(11): 3009-3020.

Gilchrist, A. R. and D. G. Gregorysmith (1988). "Compressible coanda wall jet - predictions of jet structure and comparison with experiment." *International Journal of Heat and Fluid Flow* 9(3): 286-295.

Gosset, A. and J. M. Buchlin (2007). "Jet wiping in hot-dip galvanization." *Journal of Fluids Engineering-Transactions of the ASME* 129(4): 466-475.

Guo, Y. and D. H. Wood (2002). "Measurements in the vicinity of a stagnation point." *Experimental Thermal and Fluid Science* 25(8): 605-614.

Hattori, H. and Y. Nagano (2004). "Direct numerical simulation of turbulent heat transfer in plane impinging jet." *International Journal of Heat and Fluid Flow* 25(5): 749-758.

Hrymak, A. N., Forbes, J. F., Elsaadawy, E., Balthazaar, A., Hu, Q., & Knight, J. (2004). *ZCO-2-3: Improving Coating Weight Consistency. Final Report*. McMaster University & University of Alberta.

Kataoka, K. (1990). "Impingement heat-transfer augmentation due to large-scale eddies." *Heat Transfer 1990, Vols 1-7*: 255-273

Kataoka, K., M. Suguro, et al. (1987). "The effect of surface renewal due to large-scale eddies on jet impingement heat-transfer." *International Journal of Heat and Mass Transfer* 30(3): 559-567.

Kim, S. J., J. W. Cho, et al. (2003). "Numerical analysis of edge over-coating in continuous hot-dip galvanizing." *ISIJ International* 43(10): 1495-1501.

Kim, S. E. and D. Choudhury (1995). "A Near-Wall Treatment Using Wall Functions Sensitized to Pressure Gradient." In *ASME FED Vol. 217, Separated and Complex Flows*. ASME.

Kim, G., H. Park, et al. (2008) "Gas Wiping Apparatus Having Multiple Nozzles." World Intellectual Property Organization, International Publication Number WO 2008/069362 A1.

Lacanette, D., A. Gosset, et al. (2006). "Macroscopic analysis of gas-jet wiping: Numerical simulation and experimental approach." *Physics of Fluids* 18(4).

Lacanette, D., S. Vincent, et al. (2005). "A numerical experiment on the interaction between a film and a turbulent jet." *Comptes Rendus Mecanique* 333(4): 343-349.

Launder, B. E. and B. I. Sharma (1974). "Application of the energy dissipation model of turbulence to the calculation of flow near a spinning disc." *Lett. Heat Mass Transf.* (1): 131-138.

Lee, D. W., J. G. Hwang, et al. (2007). "A study on the air knife flow with Coanda effect." *Journal of Mechanical Science and Technology* 21(12): 2214-2220.

Leschizner, M. A. (1993). "Application of second-moment closure in complex flows." VKI Lecture Series, Von Karman Institute for Fluid Dynamics.

Marder, A. R. (2000). "The metallurgy of zinc-coated steel." *Progress in Materials Science* 45(3): 191-271.

Maurel, S. and C. Sollicec (2001). "A turbulent plane jet impinging nearby and far from a flat plate." *Experiments in Fluids* 31(6): 687-696.

Myrillas, K., A. Gosset, et al. (2009). "CFD simulation of gas-jet wiping process." *European Physical Journal-Special Topics* 166: 93-97.

Naphade, P., A. Mukhopadhyay, et al. (2005). "Mathematical modeling of jet finishing process for hot-dip zinc coatings on steel strip." *ISIJ International* 45(2): 209-213.

Phares, D. J., G. T. Smedley, et al. (2000). "The wall shear stress produced by the normal impingement of a jet on a flat surface." *Journal of Fluid Mechanics* 418: 351-375.

Pope, S. B. (2000). *Turbulent flows*. Cambridge ; New York, Cambridge University Press.

Sakakibara, J., K. Hishida, et al. (1997). "Vortex structure and heat transfer in the stagnation region of an impinging plane jet (simultaneous measurements of velocity and temperature fields by digital particle image velocimetry and laser-induced fluorescence)." *International Journal of Heat and Mass Transfer* 40(13): 3163-3176.

Saripalli, K. R. (1983). "Visualization of multijet impingement flow." *AIAA Journal* 21(4): 483-484.

Sarkar, A., N. Nitin, et al. (2004). "Fluid flow and heat transfer in air jet impingement in food processing." *Journal of Food Science* 69(4): R113-R122.

Schlichting, H. (1968). *Boundary-layer theory*. New York,, McGraw-Hill.

Striegl, S. A. and T. E. Diller (1984). "The effect of entrainment temperature on jet impingement heat-transfer." *Journal of Heat Transfer-Transactions of the ASME* 106(1): 27-33.

Tu, C. V. (1993). "Strip coating device having jet strippers to control coating thickness." Patent number 5,254,166.

Tu, C. V. (1994). "Stripping liquid coatings." Patent number 5,360,641.

Tu, C. V. and D. H. Wood (1996). "Wall pressure and shear stress measurements beneath an impinging jet." *Experimental Thermal and Fluid Science* 13(4): 364-373.

Tzeng, P. Y., C. Y. Soong, et al. (1999). "Numerical investigation of heat transfer under confined impinging turbulent slot jets." *Numerical Heat Transfer Part a-Applications* 35(8): 903-924.

Voke, P. R., S. Gao, et al. (1995). "Large-Eddy Simulations of Plane Impinging Jets." *International Journal for Numerical Methods in Engineering* 38(3): 489-507.

Yoneda, H., (1993). "Analysis of air-knife coating." Master of Science dissertation, University of Minnesota, Minneapolis, MN.

Yoon, H. G. and M. K. Chung (2010). "Development of novel air-knife system to prevent check-mark stain on galvanized strip surface." *ISIJ International* 50(5): 752-759.

## Appendix A: Coating Thickness Sensitivity to Different Turbulence Models

In this section, the sensitivity of the predicted coating thickness on a moving sheet substrate in a hot-dip galvanizing line process due to the effect of different turbulence model assumptions is determined. The numerical results are compared with the experimental data of Lacanette *et al.* [2006]. In this study the standard  $k - \varepsilon$  turbulence model with non-equilibrium and enhanced wall treatments, *RNG*  $k - \varepsilon$  turbulence model with enhanced wall functions,  $k - \omega$  and shear stress transport (*SST*) turbulence models are used to approximate the coating thickness on the moving substrate. The transport equations for each turbulence model are available in FLUENT 6.3 User's Guide [2006].

### i. Numerical Simulations

All simulations were solved using FLUENT commercial code. Figure 4-1 showed the 2-D configuration of a single-impinging slot jet. In Figure 4-1,  $z$  represents the distance between the main impinging slot jet to the sheet substrate,  $d$  is the slot gap which is fixed at 1.40 mm and  $l$  is the numerical domain length along the substrate direction. For all simulations,  $l/d = 100$ . The wall pressure and shear stress distributions were computed for different  $z/d$  ratios, which varied between 2 and 12. The mesh used was comprised of quadrilaterals and was refined for all  $z/d$  ratios such that the solution was independent of mesh size. The numbers of nodes varied between 70,000 and 140,000 for different  $z/d$  ratios. The 1<sup>st</sup> order upwind scheme was used for discretization and a double precision solver was used. The main slot jet velocity is about 50 m/s which

corresponds to  $Re_m = 4500$ . The simulations were run with (5%) turbulence intensity. The turbulent length scale was set to  $9.8 \times 10^{-5}$  for the main slot jet. The non-dimensional wall distance for non-equilibrium wall treatment should lie within log-law region in which  $30 \leq y^+ \leq 300$  and inside viscous sub-layer for enhanced wall functions,  $k - \omega$  and  $SST$  turbulence models where  $y^+ \approx 1$ .

## ii. Wall Pressure Correlations

In this section, the numerical results are used to find correlations for different turbulence models. The cases are represented as follows:

case 1: Standard  $k - \varepsilon$  model with non-equilibrium wall treatment

case 2: Standard  $k - \varepsilon$  model with enhanced wall treatment

case 3: RNG  $k - \varepsilon$  model with enhanced wall treatment

case 4:  $k - \omega$  model

case 5:  $SST$  model

The numerical results are used to estimate the value of the half width of the wall pressure distributions,  $b_p$ , for different turbulence models by fitting the obtained results using second order polynomial as follows:

$$\text{case 1: } b_p/d = 0.004 (z/d)^2 - 0.0336 (z/d) + 0.8511 \quad (\text{A-1})$$

$$\text{case 2: } b_p/d = 0.0046 (z/d)^2 - 0.0273 (z/d) + 0.8227 \quad (\text{A-2})$$

$$\text{case 3: } b_p/d = 0.0011 (z/d)^2 - 0.0082 (z/d) + 0.7977 \quad (\text{A-3})$$

$$\text{case 4: } b_p/d = 0.0019 (z/d)^2 - 0.0068 (z/d) + 0.7745 \quad (\text{A-4})$$

$$\text{case 5: } b_p/d = 0.0048 (z/d)^2 - 0.0299 (z/d) + 0.8144 \quad (\text{A-5})$$

The non-dimensional wall pressure distributions are fitted to the Gaussian distribution as follows:

$$\text{case 1: } P/P_{max} = e^{-0.6920\xi_p^2} \quad (\text{A-6})$$

$$\text{case 2: } P/P_{max} = e^{-0.6886\xi_p^2} \quad (\text{A-7})$$

$$\text{case 3: } P/P_{max} = e^{-0.6218\xi_p^2} \quad (\text{A-8})$$

$$\text{case 4: } P/P_{max} = e^{-0.6651\xi_p^2} \quad (\text{A-9})$$

$$\text{case 5: } P/P_{max} = e^{-0.6702\xi_p^2} \quad (\text{A-10})$$

where  $\xi_p$  is the normalized distances,  $x/b_p$ . Based on the numerical results, the maximum pressure on the sheet substrate can be estimated using second order polynomial as follows:

$$\text{case 1: } P_{max}/(\frac{1}{2}\rho u_i^2) = -0.0042 (z/d)^2 + 0.0286 (z/d) + 1.1517 \quad (\text{A-11})$$

$$\text{case 2: } P_{max}/(\frac{1}{2}\rho u_i^2) = -0.0043 (z/d)^2 + 0.0174 (z/d) + 1.1931 \quad (\text{A-12})$$

$$\text{case 3: } P_{max}/(\frac{1}{2}\rho u_i^2) = -0.0025 (z/d)^2 + 0.0164 (z/d) + 1.1828 \quad (\text{A-13})$$

$$\text{case 4: } P_{max}/(\frac{1}{2}\rho u_i^2) = -0.0031 (z/d)^2 + 0.0110 (z/d) + 1.2139 \quad (\text{A-14})$$

$$\text{case 5: } P_{max}/(\frac{1}{2}\rho u_i^2) = -0.0040 (z/d)^2 + 0.0109 (z/d) + 1.2170 \quad (\text{A-15})$$

In the next section, the obtained wall shear stress results for each turbulence models are used to find different correlations.

### iii. Wall Shear Stress Correlations

The numerical results are used to estimate the value of the maximum location of the wall shear stress distributions,  $b_\tau$ , for different turbulence models by fitting the obtained results using linear regression as follows:

$$\text{case 1: } b_\tau/d = 0.0214 (z/d) + 1.2667 \quad (\text{A-16})$$

$$\text{case 2: } b_\tau/d = 0.0582 (z/d) + 1.1762 \quad (\text{A-17})$$

$$\text{case 3: } b_\tau/d = 0.0255 (z/d) + 1.3333 \quad (\text{A-18})$$

$$\text{case 4: } b_\tau/d = 0.0418 (z/d) + 1.1952 \quad (\text{A-19})$$

$$\text{case 5: } b_{\tau}/d = 0.0490 (z/d) + 1.3000 \quad (\text{A-20})$$

The non-dimensional wall shear stress distributions are correlated by the following formula:

$$\begin{aligned} \tau/\tau_{max} &= 1 - e^{-2.79\xi_{\tau}} & 0 \leq \xi_{\tau} < 1 \\ \text{case 1: } \tau/\tau_{max} &= 1.0 - 0.238 \ln(\xi_{\tau}) & \xi_{\tau} \geq 1 \end{aligned} \quad (\text{A-21})$$

$$\begin{aligned} \tau/\tau_{max} &= 1 - e^{-2.53\xi_{\tau}} & 0 \leq \xi_{\tau} < 1 \\ \text{case 2: } \tau/\tau_{max} &= 0.95 - 0.238 \ln(\xi_{\tau}) & \xi_{\tau} \geq 1 \end{aligned} \quad (\text{A-22})$$

$$\begin{aligned} \tau/\tau_{max} &= 1 - e^{-2.60\xi_{\tau}} & 0 \leq \xi_{\tau} < 1 \\ \text{case 3: } \tau/\tau_{max} &= 1.61 - 0.40 \ln(\xi_{\tau} + 4.54) & \xi_{\tau} \geq 1 \end{aligned} \quad (\text{A-23})$$

$$\begin{aligned} \tau/\tau_{max} &= 1 - e^{-2.79\xi_{\tau}} & 0 \leq \xi_{\tau} < 1 \\ \text{case 4: } \tau/\tau_{max} &= 1.10 - 0.27 \ln(\xi_{\tau}) & \xi_{\tau} \geq 1 \end{aligned} \quad (\text{A-24})$$

$$\begin{aligned} \tau/\tau_{max} &= 1 - e^{-2.72\xi_{\tau}} & 0 \leq \xi_{\tau} < 1 \\ \text{case 5: } \tau/\tau_{max} &= 1.16 - 0.28 \ln(\xi_{\tau}) & \xi_{\tau} \geq 1 \end{aligned} \quad (\text{A-25})$$

where  $\xi_\tau$  is the normalized distances,  $x/b_\tau$ . Based on the numerical results, the maximum wall shear stress on the sheet substrate can be correlated using linear regression as follows:

$$\text{case 1: } \tau_{max}/(\frac{1}{2}\rho u_i^2) = -0.0001 (z/d) + 0.0042 \quad (\text{A-26})$$

$$\text{case 2: } \tau_{max}/(\frac{1}{2}\rho u_i^2) = -0.0001 (z/d) + 0.0049 \quad (\text{A-27})$$

$$\text{case 3: } \tau_{max}/(\frac{1}{2}\rho u_i^2) = -3(10^{-6}) (z/d) + 0.0035 \quad (\text{A-28})$$

$$\text{case 4: } \tau_{max}/(\frac{1}{2}\rho u_i^2) = -0.0001 (z/d) + 0.0038 \quad (\text{A-29})$$

$$\text{case 5: } \tau_{max}/(\frac{1}{2}\rho u_i^2) = -0.00005 (z/d) + 0.0036 \quad (\text{A-30})$$

#### iv. Coating Thickness Results

The turbulence models used in this study have been classified as two-equation models. The above models have two transport equations for turbulent kinetic energy ( $k$ ) and the turbulent dissipation rate ( $\varepsilon$ ) or the specific dissipation rate ( $\omega$ ). These models are commonly used in engineering applications and result in lower computational costs in comparison with large eddy simulation (*LES*) method. Figure A-1 shows the coating thickness versus  $z/d$  ratio based on the wall pressure profile and shear stress results for

different turbulence models compared to the experimental data of Lacanette *et al.* [2006]

for  $V_{strip}=1.53\text{ m/s}$ .

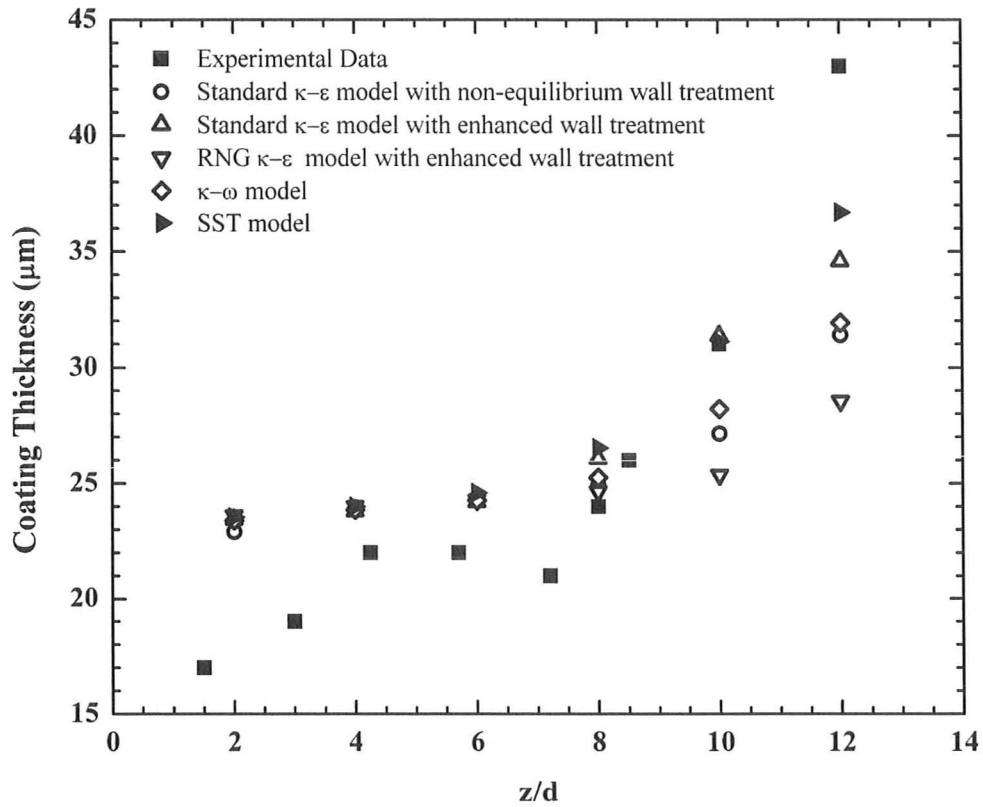


Figure A-1: Comparison of the coating thickness of Lacanette *et al.* [2006] experimental data with different turbulence models numerical data.

All of the turbulence models overestimated the coating thickness with respect to the experimental data for  $z/d \leq 8$ . The range of overestimation for the case of  $z/d = 2$  is 30-34%. For  $z/d = 4$  and 6, the error values change in the range of 8.2-10.8% while for  $z/d = 8$ , the error variations are in the range of 2.6-10.5%. The numerical results underestimated the coating thickness for  $z/d = 10$  and 12 in comparison with the experimental results. For  $z/d = 10$ , the standard  $k - \epsilon$  turbulence model with enhanced wall treatment and *SST* turbulence model have a reasonable correlation with the

experimental data. The numerical error changes between 1.2% and 0.4%, respectively. For  $z/d = 12$ , the *SST* turbulence model has the best agreement with the experimental results with an error of about 15.3%. The *RNG*  $k - \varepsilon$  turbulence model has the highest numerical error for  $z/d = 12$  ( $\sim 34\%$ ). It can be concluded that for  $z/d \leq 8$ , the coating thickness is not quite sensitive to different turbulence models, and for  $z/d \geq 8$  the *SST* turbulence model has the best agreement with the experimental data.

## v. Additional Results

The wall pressure results and wall shear stress distributions for different turbulence models are shown in this section.

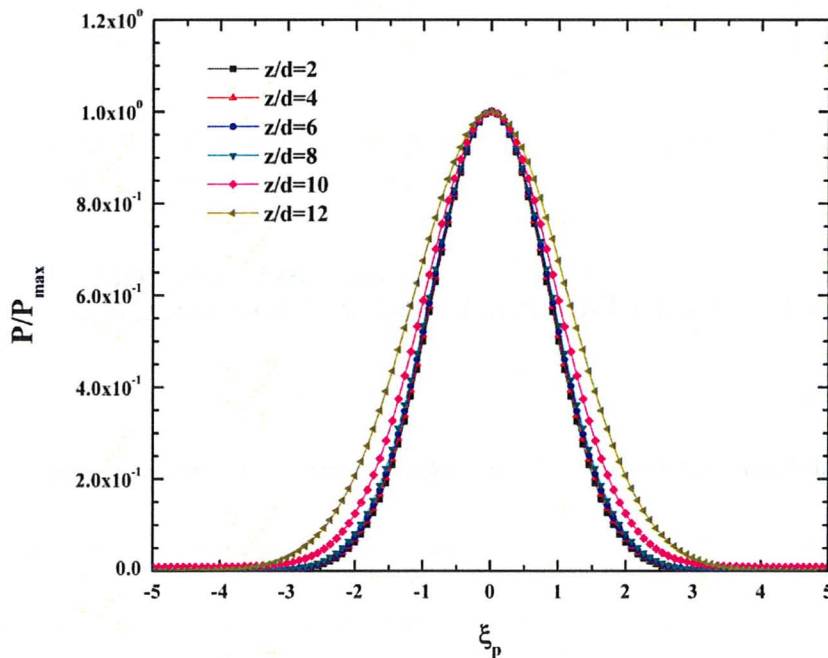


Figure A-2: Non-dimensional wall pressure distributions for different  $z/d$  ratios with  $Re_m = 4500$  for case 1.

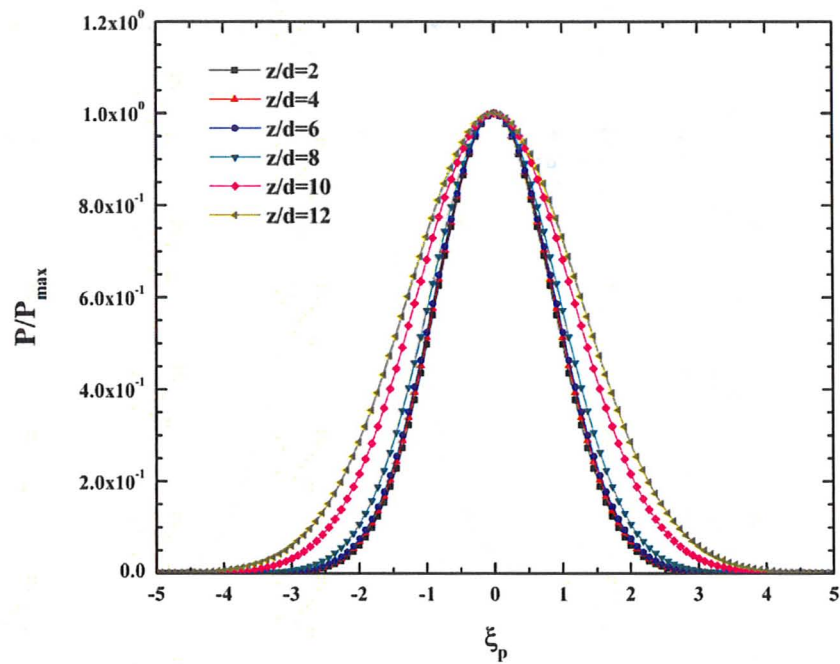


Figure A-3: Non-dimensional wall pressure distributions for different  $z/d$  ratios with  $Re_m = 4500$  for case 2.

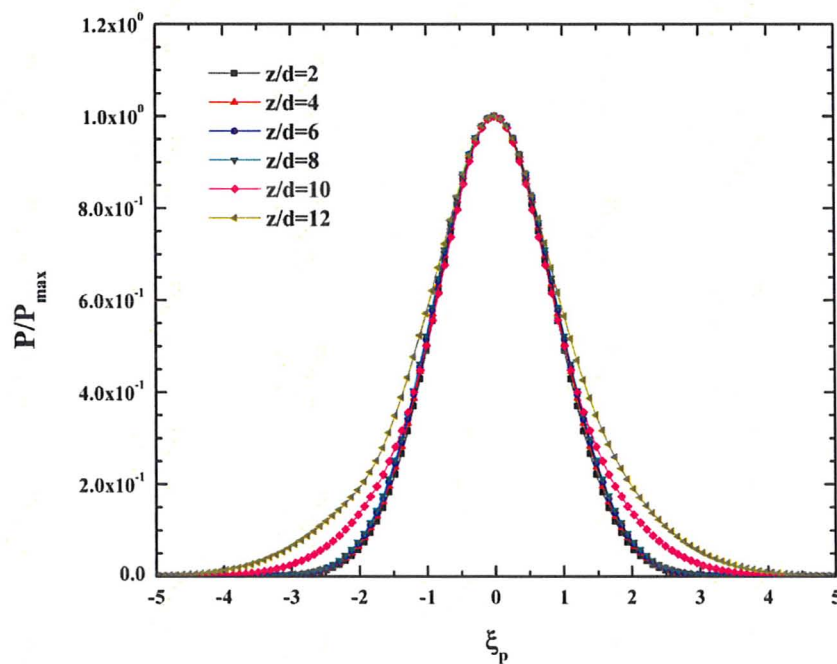


Figure A-4: Non-dimensional wall pressure distributions for different  $z/d$  ratios with  $Re_m = 4500$  for case 3.

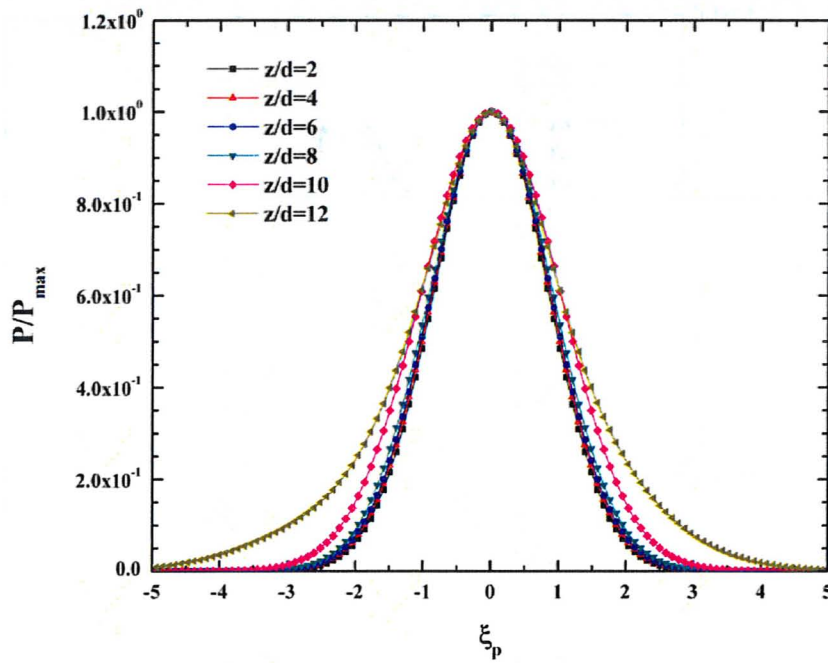


Figure A-5: Non-dimensional wall pressure distributions for different  $z/d$  ratios with  $Re_m = 4500$  for case 4.

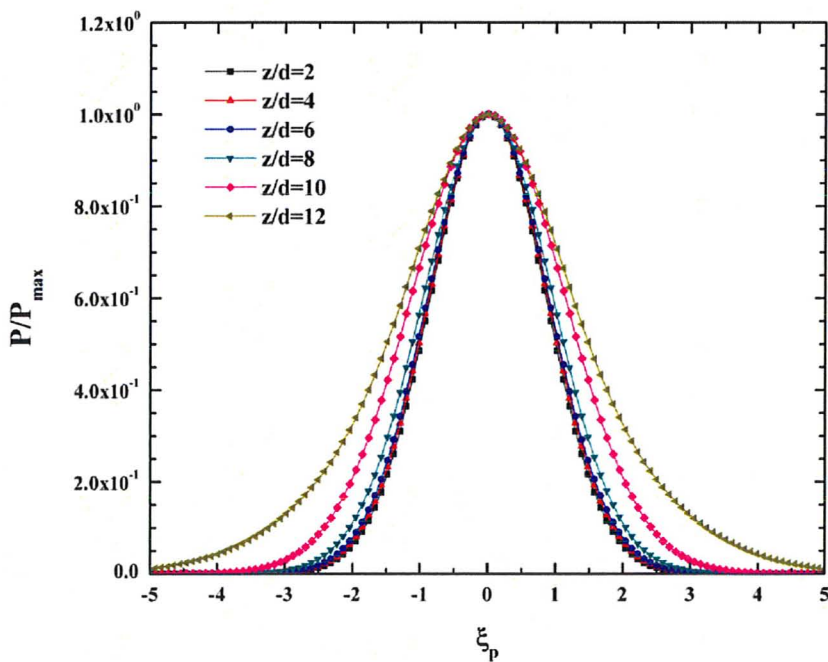


Figure A-6: Non-dimensional wall pressure distributions for different  $z/d$  ratios with  $Re_m = 4500$  for case 5.

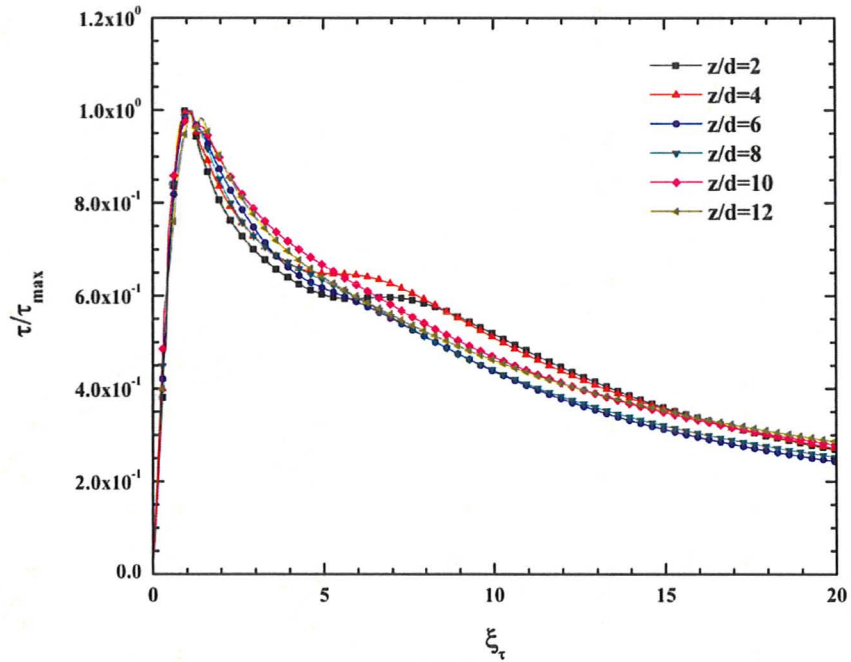


Figure A-7: Non-dimensional wall shear stress distributions for different  $z/d$  ratios with  $Re_m = 4500$  for case 1.

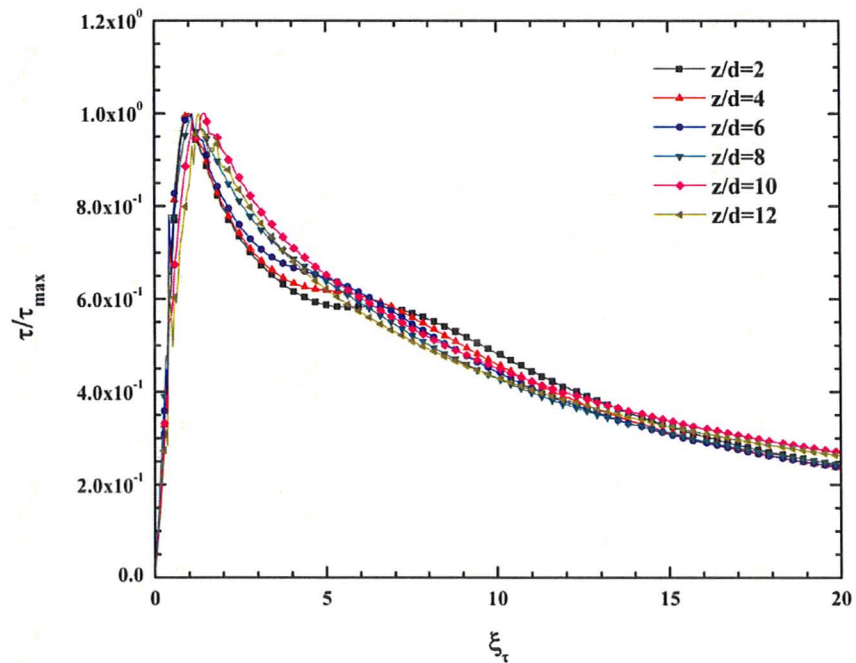


Figure A-8: Non-dimensional wall shear stress distributions for different  $z/d$  ratios with  $Re_m = 4500$  for case 2.

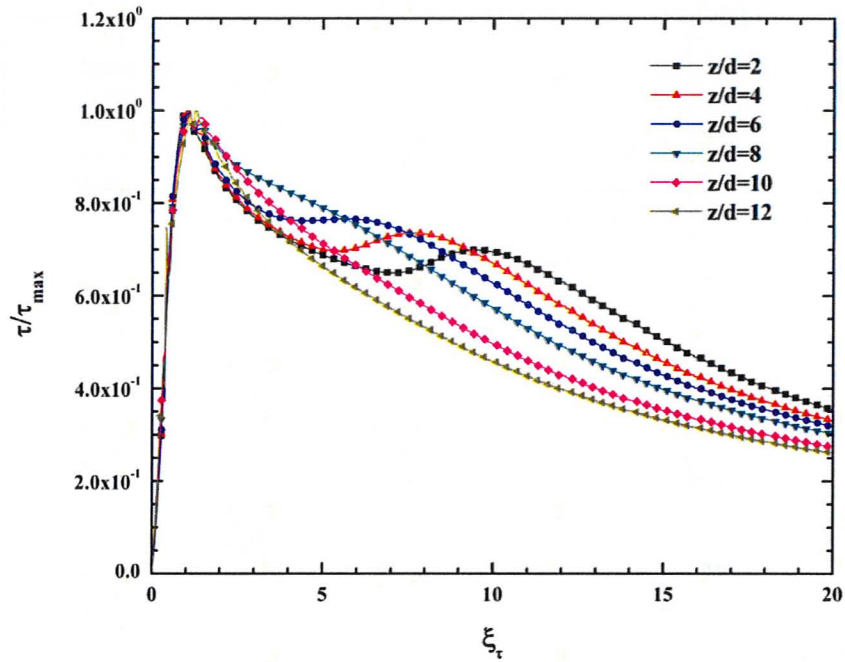


Figure A-9: Non-dimensional wall shear stress distributions for different  $z/d$  ratios with  $Re_m = 4500$  for case 3.

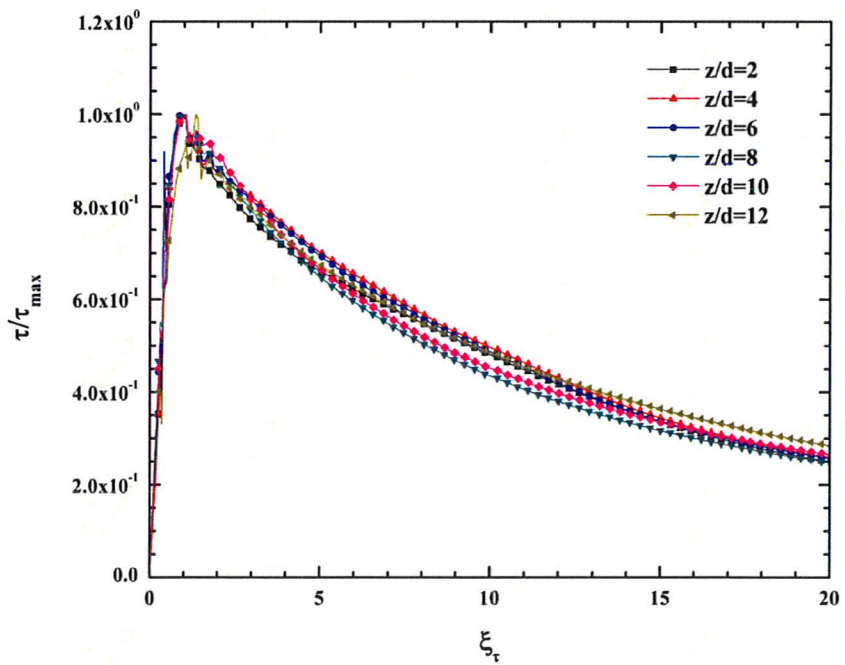


Figure A-10: Non-dimensional wall shear stress distributions for different  $z/d$  ratios with  $Re_m = 4500$  for case 4.

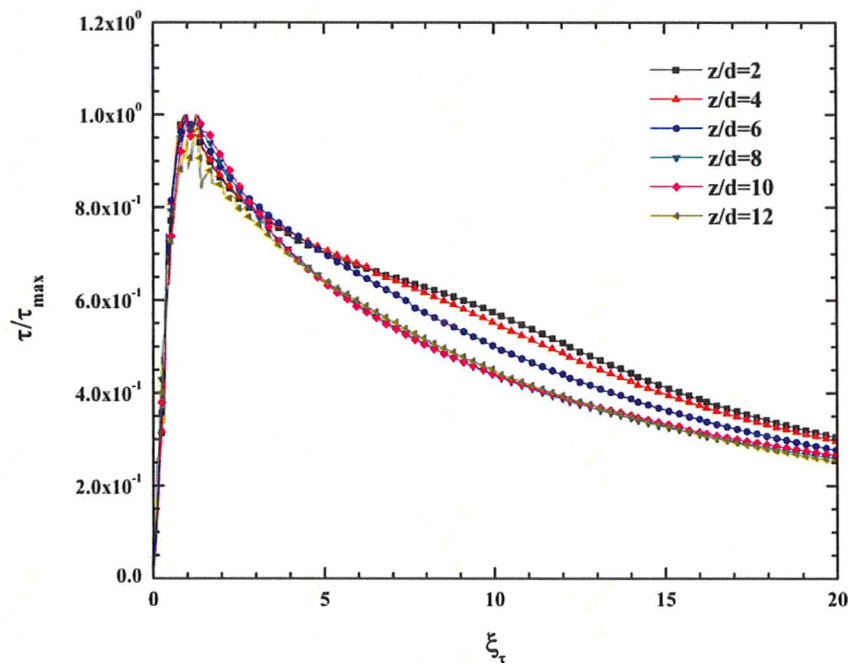


Figure A-11: Non-dimensional wall shear stress distributions for different  $z/d$  ratios with  $Re_m = 4500$  for case 5.